

MICROSCOPIC STUDIES ON TWO-PHONON GIANT RESONANCES

C.A. BERTULANI^a, V.Yu. PONOMAREV^b

^a*Instituto de Física, Universidade Federal do Rio de Janeiro, 21945-970 Rio de Janeiro,
RJ, Brazil*

^b*Bogoliubov Laboratory of Theoretical Physics, Joint Institute for Nuclear Research,
141980, Dubna, Russia*



ELSEVIER

AMSTERDAM – LAUSANNE – NEW YORK – OXFORD – SHANNON – TOKYO



Microscopic studies on two-phonon giant resonances

C.A. Bertulani^{a,*}, V.Yu. Ponomarev^b

^a*Instituto de Física, Universidade Federal do Rio de Janeiro, 21945-970 Rio de Janeiro, RJ, Brazil*

^b*Bogoliubov Laboratory of Theoretical Physics, Joint Institute for Nuclear Research, 141980, Dubna, Russia*

Received April 1999; editor: G.E. Brown

Contents

| | | | |
|---|-----|---|-----|
| 1. Introduction | 142 | 3.4. Coupled-channel calculations with inclusion of the GR widths | 196 |
| 2. Heavy ion excitation of giant resonances | 143 | 4. Description of one- and multi-phonon excited states within the quasiparticle-phonon model | 204 |
| 2.1. Coulomb excitation at relativistic energies | 143 | 4.1. The model Hamiltonian and phonons | 204 |
| 2.2. Coulomb excitation at intermediate energies | 150 | 4.2. Mixing between simple and complex configurations in wave functions of excited states | 209 |
| 2.3. Comparison of Coulomb excitation of GRs at low energies and at relativistic energies | 157 | 4.3. Comparison with other approaches | 217 |
| 2.4. Quantum description of Coulomb excitation at high energies | 161 | 5. Physical properties of the double-giant resonances | 217 |
| 2.5. Singles spectra in Coulomb excitation of GDR | 167 | 5.1. One-step excitation of two-phonon states in the energy region of giant resonances | 218 |
| 2.6. Excitation and photon decay of the GDR | 170 | 5.2. 1^+ component of the DGDR | 224 |
| 2.7. Nuclear excitation and strong absorption | 172 | 5.3. Position, width and cross section of excitation in RHIC of the DGDR in ^{136}Xe and ^{208}Pb | 228 |
| 2.8. Nucleon removal in peripheral relativistic heavy ion collisions | 174 | 5.4. The role of transitions between complex configurations of the GDR and the DGDR | 238 |
| 2.9. Excitation by a deformed nucleus | 177 | 5.5. The DGDR in deformed nuclei | 243 |
| 3. Heavy ion excitation of multiphonon resonances | 182 | Acknowledgements | 248 |
| 3.1. Introduction | 182 | References | 248 |
| 3.2. Perturbation theory and harmonic models | 184 | | |
| 3.3. General arguments on the width of the double-phonon state | 192 | | |

Abstract

A new class of giant resonances in nuclei, namely double-giant resonances, is discussed. They are giant resonances built on top of other giant resonances. Investigation on their properties, together with similar

* Corresponding author.

E-mail addresses: bertu@if.ufrj.br (C.A. Bertulani), vlad@thsun1.jinr.ru (V.Yu. Ponomarev)

studies on low-lying two-phonon states, should give an answer on how far the harmonic picture of boson-type excitations holds in the finite fermion systems like atomic nuclei. The main attention in this review is paid to double-giant dipole resonances (DGDR) which are observed in relativistic heavy ion collisions with very large cross sections. A great experimental and theoretical effort is underway to understand the reaction mechanism which leads to the excitation of these states in nuclei, as well as the better microscopic understanding of their properties. The Coulomb mechanism of the excitation of single- and double-giant resonances in heavy ion collision at different projectile energies is discussed in detail. A contribution of the nuclear excitation to the total cross section of the reaction is also considered. The Coulomb excitation of double resonances is described within both, the second-order perturbation theory approach and in coupled-channels calculation. The properties of single and double resonances are considered within the phenomenologic harmonic vibrator model and microscopic quasiparticle-RPA approach. For the last we use the quasiparticle-phonon model (QPM) the basic ideas and formalism of which are presented. The QPM predictions of the DGDR properties (energy centroids, widths, strength distributions, anharmonicities and excitation cross sections) are compared to predictions of harmonic vibrator model, results of other microscopic calculations and experimental data available. © 1999 Elsevier Science B.V. All rights reserved.

PACS: 24.30.Cz; 25.70.De; 21.60. — n

Keywords: Multi-phonon resonances; Coulomb excitation

1. Introduction

The phenomenon of a Giant Resonance (GR) in a nucleus is now known for more than 60 years. The first article on this subject was published in 1937 by Bothe and Gentner [1] who observed an unexpectedly large absorption of 17.6 MeV photons (from the ${}^7\text{Li}(p, \gamma)$ reaction) in some targets. They noticed that the cross section for ${}^{63}\text{Cu}$ was surprisingly high and they suggested that this might be due to a resonance phenomenon. These observations were later confirmed by Baldwin and Klaiber (1947) with photons from a betatron. In 1948 Goldhaber and Teller [2] interpreted these resonances (named by isovector giant dipole resonances) with a hydrodynamical model in which rigid proton and neutron fluids vibrate against each other, the restoring force resulting from the surface energy. Steinwendel and Jensen [3] later developed the model, considering compressible neutron and proton fluids vibrating in opposite phase in a common fixed sphere, the restoring force resulting from the volume symmetry energy. The standard microscopic basis for the description of giant resonances is the random phase approximation (RPA) in which giant resonances appear as coherent superpositions of one-particle one-hole ($1p1h$) excitations in closed shell nuclei or two quasi-particle excitations in open shell nuclei (for a review of these techniques, see, e.g., Ref. [4]).

The isoscalar quadrupole resonances were discovered in inelastic electron scattering by Pitthan and Walcher (1971) and in proton scattering by Lewis and Bertrand [5]. Giant monopole resonances were found later and their properties are closely related to the compression modulus of nuclear matter. Following these, other resonances of higher multiplicities and giant magnetic resonances were investigated. Typical probes for giant resonance studies are (a) γ 's and electrons for the excitation of GDR (isovector giant dipole resonance), (b) α -particles and electrons for the excitation of isoscalar GMR (giant monopole resonance) and GQR (giant quadrupole resonance), and (c) (p, n), or (${}^3\text{He}, t$), for Gamow–Teller resonances, respectively.

Relativistic coulomb excitation (RCE) is a well-established tool to unravel interesting aspects of nuclear structure [6]. Examples are the studies of multiphonon resonances in the SIS accelerator at the GSI facility, in Darmstadt, Germany [7–9]. Important properties of nuclei far from stability [10,11] have also been studied with this method.

Inelastic scattering studies with heavy ion beams have opened new possibilities in the field (for a review the experimental developments, see Refs. [7,9]). A striking feature was observed when either the beam energy was increased, or heavier projectiles were used, or both [12]. This is displayed in Fig. 1, where the excitation of the GDR in ${}^{208}\text{Pb}$ was observed in the inelastic scattering of ${}^{17}\text{O}$ at 22A and 84A MeV, respectively, and ${}^{36}\text{Ar}$ at 95A MeV [13,14]. What one clearly sees is that the “bump” corresponding to the GDR at 13.5 MeV is appreciably enhanced. This feature is solely due to one agent: the electromagnetic interaction between the nuclei. This interaction is more effective at higher energies, and for increasing charge of the projectile.

Baur and Bertulani showed in Ref. [15] that the excitation probabilities of the GDR in heavy ion collisions approach unity at grazing impact parameters. They also showed that, if double GDR resonance (i.e. a GDR excited on a GDR state) exists then the cross sections for their excitation in heavy ion collisions at relativistic energies are of order of a few hundred of milibarns. These calculations motivated experimentalists at the GSI [7,9] and elsewhere [13,14] to look for the signatures of the DGDR in the laboratory. This has by now become a very active field in nuclear physics with a great theoretical and experimental interest [7–9].

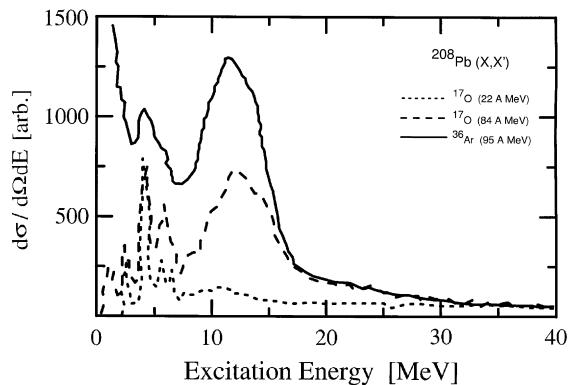


Fig. 1. Experimental cross sections in arbitrary units for the excitation of ^{208}Pb targets by ^{17}O (22A and 84A MeV) and by ^{36}Ar (95A MeV), as a function of the excitation energy.

In the first part of this review, we study the reaction mechanism in RCE of giant resonances in several collisions between heavy ions. In Section 2 we start with the description of the semiclassical theory for relativistic Coulomb excitation, then we consider the effects of recoil and later we describe the fully quantum mechanical approach. The role of nuclear excitation in relativistic heavy ion collisions is also discussed here. We demonstrate that the experimental data on the excitation and decay of single-giant resonances are well described by these formalisms. In Section 3 the process of the excitation of multi-phonon resonances in relativistic heavy ion collisions is considered within the second-order perturbation theory and in coupled-channels calculations. Giant resonances are treated in this section within the phenomenologic harmonic vibrator model. Some general arguments for the width of multi-phonon resonances are discussed here as well as an influence of giant resonances width on the total cross section of their excitation. A good part of this report (Sections 4 and 5) is dedicated to a review of the microscopic properties on the giant resonances in the quasiparticle-phonon model. In Section 4 we present the main ideas and formalism of this model. The particle-hole modes of nuclear excitation are projected into the space of quasi-bosons, phonons, and matrix elements of interaction between one- and multi-phonon configurations are calculated on microscopic footing within this approach. In Section 5, we use this model as a basis for a detailed investigation of the interplay between excitation mechanisms and the nuclear structure in the excitation of the DGDR. Different aspects related to the physical properties of the DGDR in heavy nuclei (energy centroids, widths, strength distributions, anharmonicities and excitation cross sections) as predicted by microscopic studies are discussed in this section and compared to experimental data.

2. Heavy ion excitation of giant resonances

2.1. Coulomb excitation at relativistic energies

In relativistic heavy ion collisions, the wavelength associated to the projectile-target separation is much smaller than the characteristic lengths of system. It is, therefore, a reasonable approximation

to treat \mathbf{r} as a classical variable $\mathbf{r}(t)$, given at each instant by the trajectory followed by the relative motion. At high energies, is also a good approximation to replace this trajectory by a straight line. The intrinsic dynamics can then be handled as a quantum mechanics problem with a time-dependent Hamiltonian. This treatment is discussed in full details by Alder and Winther in Refs. [16–18]. We will describe next the formalism developed by Bertulani et al. [19], which explicitly gives the time dependence of the multipole fields, useful for a coupled-channels calculation.

The intrinsic state $|\psi(t)\rangle$ satisfies the Schrödinger equation

$$[h + V(\mathbf{r}(t))]|\psi(t)\rangle = i\hbar \partial|\psi(t)\rangle/\partial t . \quad (1)$$

where h is the intrinsic Hamiltonian and V is the channel-coupling interaction.

Expanding the wave function in the set $\{|m\rangle; m = 0, N\}$ of eigenstates of h , where N is the number of excited states included in the coupled-channels problem, we obtain

$$|\psi(t)\rangle = \sum_{m=0}^N a_m(t)|m\rangle \exp(-iE_m t/\hbar) , \quad (2)$$

where E_m is the energy of the state $|m\rangle$. Taking scalar product with each of the states $\langle n|$, we get the set of coupled equations

$$i\hbar \dot{a}_n(t) = \sum_{m=0}^N \langle n|V|m\rangle e^{i(E_n - E_m)t/\hbar} a_m(t), \quad n = 0-N . \quad (3)$$

It should be remarked that the amplitudes depend also on the impact parameter b specifying the classical trajectory followed by the system. For the sake of keeping the notation simple, we do not indicate this dependence explicitly. We write, therefore, $a_n(t)$ instead of $a_n(b, t)$. Since the interaction V vanishes as $t \rightarrow \pm \infty$, the amplitudes have as initial condition $a_n(t \rightarrow -\infty) = \delta(n, 0)$ and they tend to constant values as $t \rightarrow \infty$. Therefore, the excitation probability of an intrinsic state $|n\rangle$ in a collision with impact parameter b is given as

$$P_n(b) = |a_n(\infty)|^2 . \quad (4)$$

The total cross section for excitation of the state $|n\rangle$ can be approximated by the classical expression

$$\sigma_n = 2\pi \int P_n(b) b db . \quad (5)$$

Since we are interested in the excitation of specific nuclear states, with good angular momentum and parity quantum numbers, it is appropriate to develop the time-dependent coupling interaction $V(t)$ into multipoles. In Ref. [18], a multipole expansion of the electromagnetic excitation amplitudes in relativistic heavy ion collisions was carried out. This work used first-order perturbation theory and the semiclassical approximation. The time dependence of the multipole interactions was not explicitly given. This was accomplished in Ref. [19], which we describe next.

We consider a nucleus 2 which is at rest and a relativistic nucleus 1 which moves along the z -axis and is excited from the initial state $|I_i M_i\rangle$ to the state $|I_f M_f\rangle$ by the electromagnetic field of nucleus 1. The nuclear states are specified by the spin quantum numbers I_i, I_f and by the corresponding magnetic quantum numbers M_i, M_f , respectively. We assume that the relativistic nucleus 1

moves along a straight-line trajectory with impact parameter b , which is therefore also the distance of the closest approach between the center of mass of the two nuclei at the time $t = 0$. We shall consider the situation where b is larger than the sum of the two nuclear radii, such that the charge distributions of the two nuclei do not strongly overlap at any time. The electromagnetic field of the nucleus 1 in the reference frame of nucleus 2 is given by the usual Lorentz transformation [20] of the scalar potential $\phi(\mathbf{r}) = Z_1 e/|\mathbf{r}|$, i.e.,

$$\phi(\mathbf{r}', t) = \gamma\phi[\mathbf{b}' - \mathbf{b}, \gamma(z' - vt)] , \quad \mathbf{A}(\mathbf{r}', t) = (\mathbf{v}/c)\gamma\phi[\mathbf{b}' - \mathbf{b}, \gamma(z' - vt)] . \quad (6)$$

Here \mathbf{b} (impact parameter) and \mathbf{b}' are the components of the radius-vectors \mathbf{r} and \mathbf{r}' transverse to \mathbf{v} .

The time-dependent matrix element for electromagnetic excitation is of the form

$$V_{fi}(t) = \langle I_f M_f | [\rho(\mathbf{r}') - (\mathbf{v}/c^2) \cdot \mathbf{J}(\mathbf{r}')] \phi(\mathbf{r}', t) | I_i M_i \rangle , \quad (7)$$

where ρ (\mathbf{J}) is the nuclear transition density (current).

A Taylor-series expansion of the Liénard–Wiechert potential around $\mathbf{r}' = 0$ yields

$$\phi(\mathbf{r}', t) = \gamma\phi[\mathbf{r}(t)] + \gamma\nabla\phi[\mathbf{r}(t)] \cdot \mathbf{r}' + \dots , \quad (8)$$

where $\mathbf{r} = (\mathbf{b}, \gamma vt)$, and the following simplifying notation is used:

$$\nabla\phi[\mathbf{r}] \equiv \nabla' \phi(\mathbf{r}', t)|_{\mathbf{r}'=0} = -\nabla_b \phi(\mathbf{r}) - (\partial/\partial vt)\phi(\mathbf{r})\hat{\mathbf{z}} = -\nabla_b \phi(\mathbf{r}) - (\mathbf{v}/v^2)(\partial/\partial t)\phi(\mathbf{r}) . \quad (9)$$

Thus,

$$V_{fi}(t) = \langle I_f M_f | [\rho(\mathbf{r}') - (\mathbf{v}/c^2) \cdot \mathbf{J}(\mathbf{r}')] [\gamma\phi(\mathbf{r}) + \gamma\mathbf{r}' \cdot \nabla\phi(\mathbf{r})] | I_i M_i \rangle . \quad (10)$$

Using the continuity equation

$$\nabla \cdot \mathbf{J} = -i\omega\rho , \quad (11)$$

where $\omega = (E_f - E_i)/\hbar$, and integrating by parts,

$$V_{fi}(t) = \left\langle I_f M_f \left| \mathbf{J}(\mathbf{r}) \cdot \left[\frac{\nabla'}{i\omega} - \frac{\mathbf{v}}{c^2} \right] [\gamma\phi(\mathbf{r}) + \gamma\mathbf{r}' \cdot \nabla\phi(\mathbf{r})] \right| I_i M_i \right\rangle . \quad (12)$$

In spherical coordinates

$$\mathbf{r}' \cdot \nabla\phi = \frac{\sqrt{4\pi}}{3} \sum_{\mu=-1}^1 \alpha_\mu \mathbf{r}' \cdot \mathbf{Y}_{1\mu}^* , \quad (13)$$

where

$$\alpha_\mu = \hat{\mathbf{e}}_\mu \cdot \nabla\phi , \quad (14)$$

and $\hat{\mathbf{e}}_\mu$ are the spherical unit vectors

$$\hat{\mathbf{e}}_\pm = \mp (1/\sqrt{2})(\hat{\mathbf{e}}_x \pm \hat{\mathbf{e}}_y), \quad \hat{\mathbf{e}}_0 = \hat{\mathbf{e}}_z .$$

We will use the relations

$$\mathbf{v}/c^2 = (v/c^2)\hat{\mathbf{e}}_0 = (v/c^2)\sqrt{(4\pi/3)}\nabla(rY_{10}^*) \quad (15)$$

and

$$\nabla \times \mathbf{L}(r^k Y_{lm}) = i(k+1)\nabla(r^k Y_{lm}) \quad (16)$$

where $\mathbf{L} = -i\mathbf{r} \times \nabla$.

Then, one can write

$$\begin{aligned} & \mathbf{J} \cdot \left(\frac{\nabla}{i\omega} - \frac{\mathbf{v}}{c^2} \right) [\gamma\phi + \gamma\mathbf{r}' \cdot \nabla\phi] \\ &= -\gamma\mathbf{J} \cdot \left[\frac{\mathbf{v}}{c^2} (\nabla\phi \cdot \mathbf{r}') - \sqrt{\frac{4\pi}{3}} \left\{ \sum_{\mu=-1}^1 \frac{\alpha_\mu}{i\omega} \nabla'(r' Y_{1\mu}) - \frac{v}{c^2} \phi \nabla'(r' Y_{10}^*) \right\} \right]. \end{aligned} \quad (17)$$

The first term in the above equation can be rewritten as

$$\left(\mathbf{J} \cdot \frac{\mathbf{v}}{c^2} \right) (\mathbf{r}' \cdot \nabla\phi) = \frac{v}{2c^2} \mathbf{J} \cdot [\hat{\mathbf{e}}_0(\mathbf{r}' \cdot \nabla\phi) + (\mathbf{r}' \cdot \hat{\mathbf{e}}_0)\nabla\phi] + (v/2c^2)\mathbf{J} \cdot [\hat{\mathbf{e}}_0(\mathbf{r}' \cdot \nabla\phi) - (\mathbf{r}' \cdot \hat{\mathbf{e}}_0)\nabla\phi]. \quad (18)$$

The first term in this equation is symmetric under parity inversion, and contributes to the electric quadrupole ($E2$) excitation amplitudes, since

$$(v/2c^2)\mathbf{J} \cdot [\hat{\mathbf{e}}_0(\mathbf{r}' \cdot \nabla\phi) + (\mathbf{r}' \cdot \hat{\mathbf{e}}_0)\nabla\phi] = (v/2c^2)\mathbf{J} \cdot \nabla' [z'(\mathbf{r}' \cdot \nabla\phi)]. \quad (19)$$

The second term in Eq. (18) is antisymmetric in \mathbf{J} and \mathbf{r}' , and leads to magnetic dipole ($M1$) excitations. Indeed, using Eqs. (13)–(16), one finds

$$\frac{v}{2c^2} \mathbf{J} \cdot [\hat{\mathbf{e}}_0(\mathbf{r}' \cdot \nabla\phi) - (\mathbf{r}' \cdot \hat{\mathbf{e}}_0)\nabla\phi] = \frac{v}{2c^2} \mathbf{J} \cdot \left[\sqrt{\frac{4\pi}{3}} \sum_{\mu=-1}^1 \alpha_\mu (-1)^\mu \mathbf{L}(r Y_{1,-\mu}) \right]. \quad (20)$$

Thus, only the last two terms on the right-hand side of Eq. (17) contribute to the electric dipole ($E1$) excitations. Inserting them into Eq. (12), we get

$$V_{fi}^{(E1)}(t) = \gamma \sqrt{\frac{4\pi}{3}} \sum_{\mu=-1}^1 (-1)^\mu \beta_\mu \langle I_f M_f | \mathcal{M}(E1, -\mu) | I_i M_i \rangle, \quad (21)$$

where

$$\mathcal{M}(E1, -\mu) = \frac{i}{\omega} \int d^3r \mathbf{J}(\mathbf{r}) \cdot \nabla(r Y_{1\mu}) = \int d^3r r \rho(\mathbf{r}) r Y_{1\mu}(\mathbf{r}) \quad (22)$$

and

$$\begin{aligned} \beta_\pm &= -\alpha_\mu = -(\nabla\phi \cdot \hat{\mathbf{e}}_\mu) = \hat{\mathbf{e}}_\mu \cdot \partial\phi/\partial\mathbf{b}, \\ \beta_0 &= -\alpha_0 - i(\omega v/c^2)\phi. \end{aligned} \quad (23)$$

The derivatives of the potential ϕ are explicitly given by

$$\begin{aligned} \frac{\partial\phi}{\partial\mathbf{b}_x} &\equiv \nabla_{\mathbf{b}_x}\phi|_{r'=0} = -\hat{\mathbf{x}} b_x \frac{Z_1 e}{[b^2 + \gamma^2 v^2 t^2]^{3/2}}, \\ \nabla_z\phi|_{r'=0} &= -\hat{\mathbf{z}} \gamma^2 v t \frac{Z_1 e}{[b^2 + \gamma^2 v^2 t^2]^{3/2}}. \end{aligned} \quad (24)$$

Using the results above, we get for the electric dipole potential

$$V_{fi}^{(E1)}(t) = \sqrt{\frac{2\pi}{3}} \gamma \left\{ \mathcal{E}_1(\tau) [\mathcal{M}_{fi}(E1, -1) - \mathcal{M}_{fi}(E1, 1)] + \sqrt{2} \gamma \left[\tau \mathcal{E}_1(\tau) - i \frac{\omega v}{\gamma c^2} \mathcal{E}_2(\tau) \right] \mathcal{M}_{fi}(E1, 0) \right\}, \quad (25)$$

where $\tau = \gamma v/b$, and

$$\mathcal{E}_1(\tau) = Z_1 e/b^2 [1 + \tau^2]^{3/2} \quad \text{and} \quad \mathcal{E}_2(\tau) = Z_1 e/b [1 + \tau^2]^{1/2} \quad (26)$$

are proportional to the transverse and longitudinal electric fields generated by the relativistic nucleus with charge $Z_1 e$, respectively. From the definition

$$\mathcal{M}_{fi}(M1, \mu) = -\frac{i}{2c} \int d^3r \mathbf{J}(\mathbf{r}) \cdot \mathbf{L}(r Y_{1\mu}), \quad (27)$$

and Eq. (19), we find

$$V_{fi}^{(M1)}(t) = i \sqrt{\frac{2\pi}{3}} \frac{v}{c} \gamma \mathcal{E}_1(\tau) [\mathcal{M}_{fi}(M1, 1) + \mathcal{M}_{fi}(M1, -1)]. \quad (28)$$

The current \mathbf{J} in Eq. (27) is made up of the usual convective part and a magnetization part, proportional to the intrinsic (Dirac and anomalous) magnetic moment of the nucleons. To obtain the electric quadrupole ($E2$) potential we use the third term in the Taylor expansion of Eq. (8). Using the continuity equation, a part of this term will contribute to $E3$ and $M2$ excitations, which we neglect. We then find that

$$\begin{aligned} V_{fi}^{(E2)}(\tau) = & -\sqrt{\frac{\pi}{30}} \gamma \left\{ 3\mathcal{E}_3(\tau) [\mathcal{M}_{fi}(E2, 2) + \mathcal{M}_{fi}(E2, -2)] \right. \\ & + \gamma \left[6\tau \mathcal{E}_3(\tau) - i \frac{\omega v}{\gamma c^2} \mathcal{E}_1(\tau) \right] [\mathcal{M}_{fi}(E2, -1) + \mathcal{M}_{fi}(E2, 1)] \\ & \left. + \sqrt{6} \gamma^2 \left[(2\tau^2 - 1) \mathcal{E}_3(\tau) - i \frac{\omega v}{\gamma c^2} \tau \mathcal{E}_1(\tau) \right] \mathcal{M}_{fi}(E2, 0) \right\}, \quad (29) \end{aligned}$$

where $\mathcal{E}_3(\tau)$ is the quadrupole electric field of nucleus 1, given by

$$\mathcal{E}_3(\tau) = Z_1 e/b^3 [1 + \tau^2]^{5/2}. \quad (30)$$

The fields $\mathcal{E}_i(\tau)$ peak around $\tau = 0$, and decrease fastly within an interval $\Delta\tau \simeq 1$. This corresponds to a collisional time $\Delta t \simeq b/\gamma v$. This means that, numerically one needs to integrate the coupled-channels equations (Eq. (3)) only in a time interval within a range $n \times \Delta\tau$ around $\tau = 0$, with n equal to a small integer number. A computer code for coupled channels calculations of relativistic Coulomb excitation using the formalism presented in this section is available in the literature [121].

2.1.1. First-order perturbation theory

In most cases, the first-order perturbation theory is a good approximation to calculate the amplitudes for relativistic Coulomb excitation. It amounts to using $a_k = \delta_{k0}$ on the right-hand side

of Eq. (3). The time integrals can be evaluated analytically for the $V_{Ei}(t)$ perturbations, given by Eqs. (25), (28), and (29). The result is

$$a_{1st}^{(E1)} = -i \sqrt{\frac{8\pi}{3}} \frac{Z_1 e}{\hbar v b} \xi \left\{ K_1(\xi) [\mathcal{M}_{fi}(E1, -1) - \mathcal{M}_{fi}(E1, 1)] + i \frac{\sqrt{2}}{\gamma} K_0(\xi) \mathcal{M}_{fi}(E1, 0) \right\}, \quad (31)$$

where K_1 (K_2) is the modified Bessel function of first (second) degree, and $\xi = \omega b / \gamma v$. For the $E2$ and $M1$ multipoles, we obtain respectively,

$$\begin{aligned} a_{1st}^{(E2)} = & 2i \sqrt{\frac{\pi}{30}} \frac{Z_1 e}{\gamma \hbar v b^2} \xi^2 \{ K_2(\xi) [\mathcal{M}_{fi}(E2, 2) + \mathcal{M}_{fi}(E2, -2)] \\ & + i\gamma \left(2 - \frac{v^2}{c^2} \right) K_1(\xi) [\mathcal{M}_{fi}(E2, -1) + \mathcal{M}_{fi}(E2, 1)] \\ & - \sqrt{6} K_0(\xi) \mathcal{M}_{fi}(E2, 0) \} \end{aligned} \quad (32)$$

and

$$a_{1st}^{(M1)} = \sqrt{\frac{8\pi}{3}} \frac{Z_1 e}{\hbar c b} \xi K_1(\xi) [\mathcal{M}_{fi}(M1, 1) - \mathcal{M}_{fi}(M1, -1)]. \quad (33)$$

These expressions are the same as those obtained from the formulae deduced in Ref. [18]. We note that the multipole decomposition developed by those authors is accomplished by a different approach, i.e., using recurrence relations for the Gegenbauer polynomials, after the integral on time is performed. Therefore, the above results present a good check for the time dependence of the multipole fields deduced here.

The formulas above have been derived under the assumption of the long-wavelength approximation. When this approximation is not valid the matrix elements given by Eqs. (22) and (27) are to be replaced by the non-approximated matrix elements for electromagnetic excitations [16], i.e.,

$$\mathcal{M}(E\lambda, \mu) = \frac{(2\lambda + 1)!!}{\kappa^{\lambda+1} c (\lambda + 1)} \int \mathbf{J}(\mathbf{r}) \cdot \nabla \times \mathbf{L} [j_\lambda(\kappa r) Y_{\lambda\mu}(\hat{\mathbf{r}})] d^3r, \quad (34)$$

$$\mathcal{M}(M\lambda, \mu) = -i \frac{(2\lambda + 1)!!}{\kappa^\lambda c (\lambda + 1)} \int \mathbf{J}(\mathbf{r}) \cdot \mathbf{L} [j_\lambda(\kappa r) Y_{\lambda\mu}(\hat{\mathbf{r}})] d^3r \quad (35)$$

for electric and magnetic excitations ($\kappa = \omega/c$), respectively. However, the other factors do not change (see, e.g., [18]).

2.1.2. Excitation probabilities and virtual photon numbers

The square modulus of Eqs. (31)–(33) gives the probability of exciting the target nucleus from the initial state $|I_i M_i\rangle$ to the final state $|I_f M_f\rangle$ in a collision with impact parameter b . If the orientation of the initial state is not specified, the probability for exciting the nuclear state of energy E_f and spin I_f is

$$P_{i \rightarrow f} = \frac{1}{2I_i + 1} \sum_{M_i, M_f} |a_{fi}|^2. \quad (36)$$

Integration of (36) over all energy transfers $\varepsilon = \hbar\omega$, and summation over all possible final states of the projectile nucleus (making use of the Wigner–Eckart theorem and the orthogonality of the properties of the Clebsch–Gordan coefficients) leads to the Coulomb excitation probability in a collision with impact parameter b :

$$P_C = \sum_f \int P_{i \rightarrow f}(b) \rho_f(\varepsilon) d\varepsilon \quad (37)$$

where $\rho_f(\varepsilon)$ is the density of final states of the target with energy $E_f = E_i + \varepsilon$.

Inserting (31)–(33) into (37) one finds

$$P_C(b, \varepsilon) = \sum_{\pi\lambda} P_{\pi\lambda}(b, \varepsilon) = \sum_{\pi\lambda} \int \frac{d\varepsilon}{\varepsilon} n_{\pi\lambda}(b, \varepsilon) \sigma_{\gamma}^{\pi\lambda}(\varepsilon), \quad (38)$$

where

$$\sigma_{\gamma}^{\pi\lambda}(\varepsilon) = \frac{(2\pi)^3(\lambda + 1)}{\lambda[(2\lambda + 1)!!]^2} \sum_f \rho_f(\varepsilon) \kappa^{2\lambda-1} B(\pi\lambda, I_i \rightarrow I_f) \quad (39)$$

are the photonuclear absorption cross sections for a given multipolarity $\pi\lambda$. The total photonuclear cross section is a sum of all these multiplicities,

$$\sigma_{\gamma} = \sum_{\pi\lambda} \sigma_{\gamma}^{\pi\lambda}(\varepsilon). \quad (40)$$

The functions $n_{\pi\lambda}(\varepsilon)$ are called the *virtual photon numbers*, and are given by

$$n_{E1}(b, \varepsilon) = \frac{Z_1^2 \alpha}{\pi^2} \frac{\xi^2}{b^2} \left(\frac{c}{v}\right)^2 \left\{ K_1^2 + \frac{1}{\gamma^2} K_0^2 \right\}, \quad (41)$$

$$n_{E2}(b, \varepsilon) = \frac{Z_1^2 \alpha}{\pi^2 b^2} \left(\frac{c}{v}\right)^4 \left\{ \frac{4}{\gamma^2} [K_1^2 + \xi K_0 K_1 + \xi^2 K_0^2] + \xi^2 (2 - v^2/c^2)^2 K_1^2 \right\} \quad (42)$$

and

$$n_{M1}(b, \varepsilon) = \frac{Z_1^2 \alpha}{\pi^2} \frac{\xi^2}{b^2} K_1^2, \quad (43)$$

where all modified Bessel functions K_{μ} are functions of $\xi(b) = \omega b / \gamma v$.

Since all nuclear excitation dynamics is contained in the photoabsorption cross section, the virtual photon numbers (41)–(43) do not depend on the nuclear structure. They are kinematical factors, depending on the orbital motion. They may be interpreted as the number of equivalent (virtual) photons that hit the target per unit area. These expressions show that Coulomb excitation probabilities are exactly directly proportional to the photonuclear cross sections, although the exchanged photons are off-shell. This arises from the condition that the reaction is peripheral and the nuclear charge distributions of each nuclei do not overlap during the collision. This result can be proved from first principles, and has been shown in some textbooks (see, e.g., [21]).

The usefulness of Coulomb excitation, even in first-order processes, is displayed in Eq. (38). The field of a real photon contains all multiplicities with the same weight and the photonuclear cross

section (40) is a mixture of the contributions from all multiplicities, although only a few contribute in most processes. In the case of Coulomb excitation the total cross section is weighted by kinematical factors which are different for each projectile or bombarding energy. This allows one to disentangle the multiplicities when several ones are involved in the excitation process, except for the very high bombarding energies $\gamma \gg 1$ for which all virtual photon numbers can be shown to be the same [22].

2.1.3. Cross sections and total virtual photon numbers

The cross section is obtained by the impact parameter integral of the excitation probabilities. Eq. (38) shows that we only need to integrate the number of virtual photons over impact parameter. One has to introduce a minimum impact parameter b_0 in the integration. Impact parameters smaller than b_0 are dominated by nuclear fragmentation processes. One finds

$$d\sigma_C = \sum_{\pi\lambda} \sigma_{\pi\lambda} = \sum_{\pi\lambda} \int \frac{d\varepsilon}{\varepsilon} N_{\pi\lambda}(\varepsilon) \sigma_{\gamma}^{\pi\lambda}(\varepsilon), \quad (44)$$

where the *total virtual photon numbers* $N_{\pi\lambda}(\varepsilon) = 2\pi \int db n_{\pi\lambda}(b, \varepsilon)$ are given analytically by

$$N_{E1}(\varepsilon) = \frac{2Z_1^2\alpha}{\pi} \left(\frac{c}{v}\right)^2 \left[\xi K_0 K_1 - \frac{v^2 \xi^2}{2c^2} (K_1^2 - K_0^2) \right], \quad (45)$$

$$N_{E2}(\varepsilon) = \frac{2Z_1^2\alpha}{\pi} \left(\frac{c}{v}\right)^4 \left[2 \left(1 - \frac{v^2}{c^2}\right) K_1^2 + \xi \left(1 - \frac{v^2}{c^2}\right)^2 K_0 K_1 + \frac{\xi^2 v^4}{2c^4} (K_1^2 - K_0^2) + \xi^2 (2 - v^2/c^2)^2 K_1^2 \right] \quad (46)$$

and

$$N_{M1}(\varepsilon) = \frac{2Z_1^2\alpha}{\pi} \frac{\xi^2}{b^2} \left[\xi K_0 K_1 - \frac{\xi^2}{2} (K_1^2 - K_0^2) \right], \quad (47)$$

where all K_μ 's are now functions of $\xi(b) = \omega b_0/\gamma v$.

2.2. Coulomb excitation at intermediate energies

2.2.1. Classical trajectory: recoil and retardation corrections

The semiclassical theory of Coulomb excitation in low-energy collisions accounts for the Rutherford bending of the trajectory, but relativistic retardation effects are neglected [17]. On the other hand, in the theory of relativistic Coulomb excitation [18], recoil effects on the trajectory are neglected (one assumes straight-line motion) but retardation is handled correctly. In fact, the onset of retardation brings new important effects such as the steady increase of the excitation cross sections with bombarding energy. In a heavy ion collision around 100A MeV, the Lorentz factor γ is about 1.1. Since this factor enters the excitation cross sections in many ways, like in the adiabaticity parameter

$$\xi(\mathbf{R}) = \omega_{fi} \mathbf{R}/\gamma v, \quad (48)$$

one expects that some sizable modifications in the theory of relativistic Coulomb excitation should occur [23]. Recoil corrections are not negligible either, and the relativistic calculations based on the straight-line parametrization should not be completely appropriate to describe the excitation probabilities and cross sections. The Coulomb recoil in a single collision is of the order of

$$a_0 = Z_1 Z_2 e^2 / m_0 v^2, \quad (49)$$

which is *half-distance of closest approach* in a head-on collision, with m_0 equal to the reduced mass of the colliding nuclei. Although this recoil is small for intermediate energy collisions, the excitation probabilities are quite sensitive to it. This is important for example in the excitation of giant resonances because the adiabaticity parameter is of the order of one (see, Eq. (48)). When $\xi(b) \ll 1$, the excitation probabilities depends on b approximately like $1/b^2$, while when $\xi(b)$ becomes greater than one they decrease approximately as $e^{-2\pi\xi(b)}/b^2$. Therefore, when $\xi \simeq 1$, a slight change of b may vary appreciably the excitation probabilities.

In the semiclassical theory of Coulomb excitation the nuclei are assumed to follow classical trajectories and the excitation probabilities are calculated in time-dependent perturbation theory. At low energies one assumes Rutherford trajectories for the relative motion while at relativistic energies one assumes straight-line motion. In intermediate energy collisions, where one wants to account for recoil and retardation simultaneously, one should solve the general classical problem of the motion of two relativistic charged particles. But, even if radiation is neglected, this problem can only be solved if one particle has infinite mass [24]. This approximation should be sufficient if we take, e.g., the collision $^{16}\text{O} + ^{208}\text{Pb}$ as our system. An improved solution may be obtained by use of the reduced mass, as we show next, in a formalism developed by Aleixo and Bertulani [23].

In the classical one-body problem, one starts with the relativistic Lagrangian

$$\mathcal{L} = -m_0 c^2 \{1 - (1/c^2)(\dot{r}^2 + r^2 \dot{\phi}^2)\}^{1/2} - Z_1 Z_2 e^2 / r, \quad (50)$$

where \dot{r} and $\dot{\phi}$ are the radial and the angular velocity of the particle, respectively (see Fig. 2). Using the Euler–Lagrange equations one finds three kinds of solutions, depending on the sign of the charges and the angular momentum in the collision. In the case of our interest, the appropriate solution relating the collisional angle ϕ and the distance r between the nuclei is [24]

$$1/r = A[\varepsilon \cos(W\phi) - 1] \quad (51)$$

where

$$W = [1 - (Z_1 Z_2 e^2 / c L_0)^2]^{1/2}, \quad (52)$$

$$A = Z_1 Z_2 e^2 E / c^2 L_0^2 W^2, \quad (53)$$

$$\varepsilon = (c L_0 / Z_1 Z_2 e^2 E) [E^2 - m_0^2 c^4 + (m_0 c Z_1 Z_2 e^2 / L_0)^2]^{1/2}. \quad (54)$$

E is the total bombarding energy in MeV, m_0 is the mass of the particle and L_0 its angular momentum. In terms of the Lorentz factor γ and of the impact parameter b , $E = \gamma m_0 c^2$ and $L_0 = \gamma m_0 v b$. The above solution is valid if $L_0 > Z_1 Z_2 e^2 / c$. In heavy ion collisions at intermediate energies one has $L_0 \gg Z_1 Z_2 e^2 / c$ for impact parameters that do not lead to strong interactions. It is

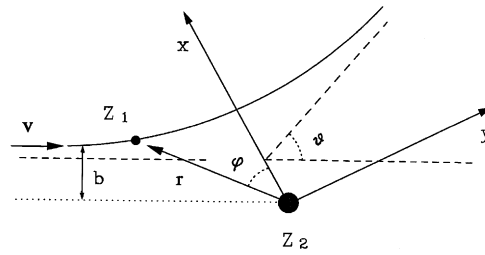


Fig. 2. A nuclear target is Coulomb excited by a fast moving projectile. The coordinates used in text are shown.

also easy to show that, from the magnitudes of the parameters involved in heavy ion collisions at intermediate energies, the trajectory (51) can be very well described by approximating

$$W = 1, \quad A = a_0/\gamma b^2, \quad \varepsilon = \sqrt{(b^2\gamma^2/a_0^2) + 1}, \quad (55)$$

where a_0 is half the distance of closest approach in a head on collision (if the nuclei were pointlike and if non-relativistic kinematics were used), and ε is the eccentricity parameter. In the approximation (55) ε is related to the deflection angle ϑ by $\varepsilon = (a_0/\gamma) \cot \vartheta$.

The time dependence for a particle moving along the trajectory (51) may be directly obtained by solving the equation of angular momentum conservation. Introducing the parametrization

$$r(\chi) = (a_0/\gamma)[\varepsilon \cosh \chi + 1] \quad (56)$$

we find

$$t = (a_0/\gamma v)[\chi + \varepsilon \sinh \chi]. \quad (57)$$

Using the scattering plane perpendicular to the Z -axis, one finds that the corresponding components of \mathbf{r} may be written as

$$x = a[\cosh \chi + \varepsilon], \quad (58)$$

$$y = a\sqrt{\varepsilon^2 - 1} \sinh \chi, \quad (59)$$

$$z = 0, \quad (60)$$

where $a = a_0/\gamma$. This parametrization is of the same form as commonly used in the non-relativistic case [17], except that a_0 is substituted by $a_0/\gamma \equiv a$.

In the limit of straight-line motion $\varepsilon \simeq b/a \gg 1$, and the equations above reduce to the simple parametrization

$$y = vt, \quad x = b \quad \text{and} \quad z = 0. \quad (61)$$

As we quoted before, the classical solution for the relative motion of two relativistic charges interacting electromagnetically can only be solved analytically if one of the particles has infinite mass. Non-relativistically the two-body problem is solvable by introduction of center of mass and relative motion coordinates. Then, the result is equivalent to that of a particle with reduced mass $m_0 = m_P m_T / (m_P + m_T)$ under the action of the same potential. The particle with reduced mass m_0 is lighter than those with mass m_P and m_T , and this accounts for the simultaneous recoil of them. An

exact relativistic solution should reproduce this behavior as the relative motion energy is lowered. We shall use the reduced mass definition of m_0 as usual in the parametrization of the classical trajectory of Coulomb excitation in intermediate energy collisions, as outlined above. In a $^{16}\text{O} + ^{208}\text{Pb}$ collision this is not a too serious approximation. For heavier systems like $\text{U} + \text{U}$ it would be the simplest way to overcome this difficulty. But, as energy increases, this approximation is again unimportant since the trajectories will be straight lines parametrized by an impact parameter b . A more exact result can be obtained numerically using the Darwin Lagrangian to determine the classical trajectory in collisions at intermediate energies [25]. But, the parametrization of the classical trajectory as given by Eqs. (58)–(60) with a reduced mass particle, besides reproducing both the non-relativistic and the relativistic energies, gives a reasonable solution to the kind of collisions we want to study.

2.2.2. Excitation amplitudes

Including retardation, the amplitude for Coulomb excitation of a target from the initial state $|i\rangle$ to the final state $|f\rangle$ is given in first-order time-dependent perturbation theory by

$$a_{fi} = \frac{1}{i\hbar} \int \left\{ \rho_{fi}(\mathbf{r}) \phi(\omega, \mathbf{r}) + \frac{1}{c} \mathbf{J}_{fi}(\mathbf{r}) \cdot \mathbf{A}(\omega, \mathbf{r}) \right\} d^3r \quad (62)$$

where ρ_{fi} (\mathbf{J}_{fi}) is the nuclear transition density (current) and

$$\phi(\omega, \mathbf{r}) = Z_1 e \int_{-\infty}^{\infty} e^{i\omega t} \frac{e^{i\kappa|\mathbf{r}-\mathbf{r}'(t)|}}{|\mathbf{r}-\mathbf{r}'(t)|} dt, \quad (63)$$

$$\mathbf{A}(\omega, \mathbf{r}) = \frac{Z_1 e}{c} \int_{-\infty}^{\infty} \mathbf{v}'(t) e^{i\omega t} \frac{e^{i\kappa|\mathbf{r}-\mathbf{r}'(t)|}}{|\mathbf{r}-\mathbf{r}'(t)|} dt \quad (64)$$

are the retarded potentials generated by a projectile with charge Z_2 following a Coulomb trajectory, and $\kappa = \omega/c$. When the magnitude of the amplitudes (62) is small compared to unity, the use of first-order perturbation theory is justified.

We now use the expansion

$$\frac{e^{i\kappa|\mathbf{r}-\mathbf{r}'|}}{|\mathbf{r}-\mathbf{r}'|} = 4\pi i \kappa \sum_{\lambda\mu} j_{\lambda}(\kappa r_{<}) Y_{\lambda\mu}^*(\hat{\mathbf{r}}_{<}) h_{\lambda}(\kappa r_{>}) Y_{\lambda\mu}(\hat{\mathbf{r}}_{>}), \quad (65)$$

where j_{λ} (h_{λ}) denotes the spherical Bessel (Hankel) functions (of first kind), $\mathbf{r}_{>}$ ($\mathbf{r}_{<}$) refers to whichever of \mathbf{r} and \mathbf{r}' has the larger (smaller) magnitude. Assuming that the projectile does not penetrate the target, we use $\mathbf{r}_{>}$ ($\mathbf{r}_{<}$) for the projectile (target) coordinates. At collision energies above the Coulomb barrier this assumption only applies for impact parameters larger than a certain minimum, below which the nuclei penetrate each other. Using the continuity equation (11) for the nuclear transition current (we changed the notation: $\rho \equiv \rho_{fi}$, $\mathbf{J} \equiv \mathbf{j}_{fi}$), we can show that the expansion (65) can be expressed in terms of spherical tensors (see, e.g., Ref. [21, Vol. II]) and Eq. (62) becomes

$$a_{fi} = \frac{Z_1 e}{i\hbar} \sum_{\lambda\mu} \frac{4\pi}{2\lambda+1} (-1)^{\mu} \{ S(E\lambda, \mu) \mathcal{M}_{fi}(E\lambda, -\mu) + S(M\lambda, \mu) \mathcal{M}_{fi}(M\lambda, -\mu) \}, \quad (66)$$

where $\mathcal{M}(\pi\lambda, \mu)$ are the matrix elements for electromagnetic transitions, as defined in (34) and (35).

The orbital integrals $S(\pi\lambda, \mu)$ are given by

$$S(E\lambda, \mu) = -\frac{i\kappa^{\lambda+1}}{\lambda(2\lambda-1)!!} \int_{-\infty}^{\infty} \frac{\partial}{\partial r'} \{r'(t) h_\lambda[\kappa r'(t)]\} Y_{\lambda\mu}[\theta'(t), \phi'(t)] e^{i\omega t} dt \\ - \frac{\kappa^{\lambda+2}}{c\lambda(2\lambda-1)!!} \int_{-\infty}^{\infty} \mathbf{v}'(t) \cdot \mathbf{r}'(t) h_\lambda[\kappa r'(t)] Y_{\lambda\mu}[\theta'(t), \phi'(t)] e^{i\omega t} dt \quad (67)$$

and

$$S(M\lambda, \mu) = -\frac{i}{\gamma m_0 c} \frac{\kappa^{\lambda+1}}{\lambda(2\lambda-1)!!} \mathbf{L}_0 \cdot \int_{-\infty}^{\infty} \nabla' \{h_\lambda[\kappa r'(t)] Y_{\lambda\mu}[\theta'(t), \phi'(t)]\} e^{i\omega t} dt, \quad (68)$$

where \mathbf{L}_0 is the angular momentum of relative motion, which is constant:

$$L_0 = \gamma a m_0 v \cot \vartheta/2 \quad (69)$$

with ϑ equal to the (center-of-mass) scattering angle.

In non-relativistic collisions

$$\kappa r' = \omega r'/c = (v/c)(\omega r'/v) < (v/c) \ll 1 \quad (70)$$

because when the relative distance r' obeys the relations $\omega r'/v \geq 1$ the interaction becomes adiabatic. Then one uses the limiting form of h_λ for small values of its argument [26] to show that

$$S^{\text{NR}}(E\lambda, \mu) \simeq \int_{-\infty}^{\infty} r'^{-\lambda-1}(t) Y_{\lambda\mu}[\theta'(t), \phi'(t)] e^{i\omega t} dt \quad (71)$$

and

$$S^{\text{NR}}(M\lambda, \mu) \simeq -\frac{1}{\lambda m_0 c} \mathbf{L}_0 \cdot \int_{-\infty}^{\infty} \nabla' \{r'^{-\lambda-1}(t) Y_{\lambda\mu}[\theta'(t), \phi'(t)]\} e^{i\omega t} dt \quad (72)$$

which are the usual orbital integrals in the non-relativistic Coulomb excitation theory with hyperbolic trajectories (see Ref. [17, Eqs. (II.A.43)]).

In the intermediate energy case the relation (69) is partially relaxed (of course, for relativistic energies, $v \sim c$, it is not valid) and one has to keep the more complex forms (67), (68) for the orbital integrals.

Using the Z -axis perpendicular to the trajectory plane, the recursion relations for the spherical Hankel functions and the identity

$$\mathbf{v} \cdot \mathbf{r} = d\chi/dt \otimes d\mathbf{r}/d\chi \cdot \mathbf{r} = a\epsilon v \sinh \chi, \quad (73)$$

we can rewrite the orbital integrals, in terms of the parametrization (58)–(60), as

$$S(E\lambda, \mu) = -\frac{i\kappa^\lambda \eta}{c\lambda(2\lambda-1)!!} \mathcal{C}_{\lambda\mu} \int_{-\infty}^{\infty} d\chi e^{i\eta(\epsilon \sinh \chi + \chi)} \frac{(\epsilon + \cosh \chi + i\sqrt{\epsilon^2 - 1} \sinh \chi)^\mu}{(\epsilon \cosh \chi + 1)^\mu} \\ \times \left[(\lambda + 1) h_\lambda - \frac{v\eta}{c} (\epsilon \cosh \chi + 1) h_{\lambda+1} + i \left(\frac{v}{c}\right)^2 \eta \epsilon \sinh \chi \cdot h_\lambda \right], \quad (74)$$

where

$$\mathcal{C}_{\lambda\mu} = \begin{cases} \sqrt{\frac{2\lambda+1}{4\pi}} \frac{\sqrt{(\lambda-\mu)!(\lambda+\mu)!}}{(\lambda-\mu)!(\lambda+\mu)!} (-1)^{(\lambda+\mu)/2} & \text{for } \lambda + \mu = \text{even} , \\ 0 & \text{for } \lambda + \mu = \text{odd} \end{cases} \quad (75)$$

and

$$\eta = \omega a/v = \omega a_0/\gamma v , \quad (76)$$

and with all h_λ 's as functions of $(v/c)\eta(\varepsilon \cosh \chi + 1)$.

For convenience, we define

$$I(E\lambda, \mu) = (va^\lambda/\mathcal{C}_{\lambda\mu})S(E\lambda, \mu) \quad (77)$$

and we translate the path of integration by an amount $i\pi/2$ to avoid strong oscillations of the integral. We find,

$$I(E\lambda, \mu) = -i \left(\frac{v\eta}{c}\right)^{\lambda+1} \frac{1}{\lambda(2\lambda-1)!!} e^{-\pi\eta/2} \int_0^\infty d\chi e^{-\eta\varepsilon \cosh \chi} e^{i\eta\chi} \\ \times \frac{(\varepsilon + i \sinh \chi - \sqrt{\varepsilon^2 - 1} \cosh \chi)^\mu}{(i\varepsilon \sinh \chi + 1)^{\mu-1}} \left[(\lambda+1)h_\lambda - zh_{\lambda+1} - \left(\frac{v}{c}\right)^2 \varepsilon\eta \cosh \chi \cdot h_\lambda \right], \quad (78)$$

where all h_λ 's are now functions of

$$z = (v/c)\eta(i\varepsilon \sinh \chi + 1) . \quad (79)$$

In the case of magnetic excitations, one may explore the fact that L_0 is perpendicular to the scattering plane to show that

$$\frac{1}{m_0} L_0 \cdot \nabla \left\{ h_\lambda(\kappa r) Y_{\lambda\mu} \left(\frac{\pi}{2}, \phi \right) \right\} = \gamma \frac{av}{r} \cot \frac{\vartheta}{2} \sqrt{\frac{2\lambda+1}{2\lambda+3}} \sqrt{(\lambda+1)^2 - \mu^2} \mathcal{C}_{\lambda+1, \mu} e^{i\mu\phi} h_\lambda(\kappa r) . \quad (80)$$

The magnetic orbital integrals become

$$S(M\lambda, \mu) = -ia \frac{v}{c} \frac{\kappa^{\lambda+1}}{\lambda(2\lambda-1)!!} \sqrt{\frac{2\lambda+1}{2\lambda+3}} \sqrt{(\lambda+1)^2 - \mu^2} \\ \times \mathcal{C}_{\lambda+1, \mu} \cot \frac{\vartheta}{2} \int_{-\infty}^\infty h_\lambda[\kappa r'(t)] \frac{1}{r'(t)} e^{i\mu\phi'(t)} e^{i\omega t} dt . \quad (81)$$

Defining

$$I(M\lambda, \mu) = -\frac{\lambda ca^\lambda S(M\lambda, \mu)}{\mathcal{C}_{\lambda+1, \mu} \cot \vartheta/2} \{ [(2\lambda+1)/(2\lambda+3)][(\lambda+1)^2 - \mu^2] \}^{-1/2} \quad (82)$$

we obtain, using the parametrization (58)–(60), and translating the integral path by $i\pi/2$,

$$I(M\lambda, \mu) = \frac{i(v\eta/c)^{\lambda+1}}{(2\lambda-1)!!} e^{-\pi\eta/2} \int_{-\infty}^\infty d\chi h_\lambda(z) e^{-\eta\varepsilon \cosh \chi} e^{i\eta\chi} \frac{(\varepsilon + i \sinh \chi - \sqrt{\varepsilon^2 - 1} \cosh \chi)^\mu}{(i\varepsilon \sinh \chi + 1)^\mu} . \quad (83)$$

Generally, the most important magnetic excitation has $M1$ multipolarity. The orbital integrals (78), (83) can only be solved numerically.

2.2.3. Cross sections and equivalent photon numbers

In the high-energy limit the classical trajectory reduces to a straight line. One can show that using the approximation $\varepsilon = b/a \gg 1$, the orbital integrals (78) and (83) can be expressed in terms of simple analytical functions. However, it is instructive and useful to deduce the excitation amplitudes from the first principles again.

The square modulus of Eq. (66) gives the probability of exciting the target nucleus from the initial state $|I_i M_i\rangle$ to the final state $|I_f M_f\rangle$ in a collision with c.m. scattering angle ϑ . If the orientation of the initial state is not specified, the cross section for exciting the nuclear state of spin I_f is

$$d\sigma_{i \rightarrow f} = \frac{a^2 \varepsilon^4}{4} \frac{1}{2I_i + 1} \sum_{M_i, M_f} |a_{fi}|^2 d\Omega, \quad (84)$$

where $a^2 \varepsilon^4 d\Omega/4$ is the elastic (Rutherford) cross section. Using the Wigner–Eckart theorem and the orthogonality properties of the Clebsch–Gordan coefficients, one can show that

$$\frac{d\sigma_{i \rightarrow f}}{d\Omega} = \frac{4\pi^2 Z_1^2 e^2}{\hbar^2} a^2 \varepsilon^4 \sum_{\lambda\mu} \frac{B(\pi\lambda, I_i \rightarrow I_f)}{(2\lambda + 1)^3} |S(\pi\lambda, \mu)|^2, \quad (85)$$

where $\pi = E$ or M stands for the electric or magnetic multipolarity, and the reduced transition probability is given by

$$\begin{aligned} B(\pi\lambda; I_i \rightarrow I_f) &= \frac{1}{2I_i + 1} \sum_{M_i, M_f} |\langle I_i M_i | \mathcal{M}(\pi\lambda, \mu) | I_f M_f \rangle|^2 \\ &= \frac{1}{2I_i + 1} |\langle I_i || \mathcal{M}(\pi\lambda) || I_f \rangle|^2. \end{aligned} \quad (86)$$

Integration of (85) over all energy transfers $\varepsilon = \hbar\omega$, and summation over all possible final states of the projectile nucleus leads to

$$\frac{d\sigma_C}{d\Omega} = \sum_f \int \frac{d\sigma_{i \rightarrow f}}{d\Omega} \rho_f(\varepsilon) d\varepsilon, \quad (87)$$

where $\rho_f(\varepsilon)$ is the density of final states of the target with energy $E_f = E_i + \varepsilon$. Inserting (85) into (87) one finds

$$\frac{d\sigma_C}{d\Omega} = \sum_{\pi\lambda} \frac{d\sigma_{\pi\lambda}}{d\Omega} = \sum_{\pi\lambda} \int \frac{d\varepsilon}{\varepsilon} \frac{dn_{\pi\lambda}}{d\Omega}(\varepsilon) \sigma_{\gamma}^{\pi\lambda}(\varepsilon), \quad (88)$$

where $\sigma_{\gamma}^{\pi\lambda}$ are the photonuclear absorption cross sections for a given multipolarity $\pi\lambda$. The *virtual photon numbers*, $n_{\pi\lambda}(\varepsilon)$, are given by

$$\frac{dn_{\pi\lambda}}{d\Omega} = \frac{Z_1^2 \alpha}{2\pi} \frac{\lambda [(2\lambda + 1)!!]^2}{(\lambda + 1)(2\lambda + 1)^3} \frac{c^2 a^2 \varepsilon^4}{\kappa^{2(\lambda-1)}} \sum_{\mu} |S(\pi\lambda, \mu)|^2. \quad (89)$$

In terms of the orbital integrals $I(E\lambda, \mu)$, given by (79), and using Eq. (89), we find for the electric multipoles

$$\frac{dn_{E\lambda}}{d\Omega} = \frac{Z_1^2 \alpha \left(\frac{c}{v}\right)^{2\lambda}}{8\pi^2} \frac{\lambda[(2\lambda + 1)!!]^2}{(\lambda + 1)(2\lambda + 1)^2} \varepsilon^4 \eta^{-2\lambda+2} \sum_{\substack{\mu \\ \lambda + \mu = \text{even}}} \frac{(\lambda - \mu)!(\lambda + \mu)!}{[(\lambda - \mu)!(\lambda + \mu)!!]^2} |I(E\lambda, \mu)|^2. \quad (90)$$

In the case of magnetic excitations we find

$$\begin{aligned} \frac{dn_{M\lambda}}{d\Omega} &= \frac{Z_1^2 \alpha \left(\frac{c}{v}\right)^{2(\lambda-1)}}{8\pi^2} \frac{[(2\lambda + 1)!!]^2}{\lambda(\lambda + 1)(2\lambda + 1)^2} \eta^{-2\lambda+2} \varepsilon^4 (\varepsilon^2 - 1) \\ &\times \sum_{\substack{\mu \\ \lambda + \mu = \text{odd}}} \frac{[(\lambda + 1)^2 - \mu^2](\lambda + 1 - \mu)!(\lambda + 1 + \mu)!}{[(\lambda + 1 - \mu)!(\lambda + 1 + \mu)!!]^2} |I(M\lambda, \mu)|^2. \end{aligned} \quad (91)$$

Only for the $E1$ multipolarity the integrals can be performed analytically and we get the closed expression

$$\frac{dn_{E1}}{d\Omega} = \frac{Z_1^2 \alpha \left(\frac{c}{v}\right)^2}{4\pi^2} \varepsilon^4 \zeta^2 e^{-\pi\zeta} \left\{ \frac{1}{\gamma^2} \frac{\varepsilon^2 - 1}{\varepsilon^2} [K_{i\zeta}(\varepsilon\zeta)]^2 + [K'_{i\zeta}(\varepsilon\zeta)]^2 \right\}, \quad (92)$$

where $\varepsilon = 1/\sin(\theta/2)$, $\alpha = 1/137$, $\zeta = \omega a_0/\gamma v$, $a_0 = Z_1 Z_2 e^2/2E_{\text{Lab}}$, $K_{i\zeta}$ is the modified Bessel function with imaginary index, $K'_{i\zeta}$ is the derivative with respect to its argument. Since the impact parameter is related to the scattering angle by $b = a \cot \vartheta/2$, we can also write

$$n_{\pi\lambda}(\varepsilon, b) \equiv \frac{dn_{\pi\lambda}}{2\pi b db} = \frac{4}{a^2 \varepsilon^4} \frac{dn_{\pi\lambda}}{d\Omega} \quad (93)$$

which are interpreted as the number of equivalent photons of energy $\varepsilon = \hbar\omega$, incident on the target per unit area, in a collision with impact parameter b , in analogy with the results obtained in Section 2.1.2.

Again we stress the usefulness of the concept of virtual photon numbers, especially in relativistic collisions. In these collisions the momentum and the energy transfer due to the Coulomb interaction are related by $\Delta p = \Delta E/v \simeq \Delta E/c$. This means that the virtual photons are almost real. One usually explores this fact to extract information about real photon processes from the reactions induced by relativistic charges, and vice versa. This is the basis of the Weizsäcker–Williams method, commonly used to calculate cross sections for Coulomb excitation, particle production, Bremsstrahlung, etc. (see, e.g., Ref. [6]). In the case of Coulomb excitation, even at low energies, although the equivalent photon numbers should not be interpreted as (almost) real ones, the cross sections can still be written as a product of them and the cross sections induced by real photons, as we have shown above.

2.3. Comparison of Coulomb excitation of GRs at low energies and at relativistic energies

Inserting the non-relativistic orbital integrals into Eq. (89), we get the following relation for the non-relativistic equivalent photon numbers (NR):

$$\frac{dn_{\pi\lambda}^{\text{(NR)}}}{d\Omega} = Z_1^2 \alpha \frac{\lambda[(2\lambda + 1)!!]^2}{(2\pi)^3(\lambda + 1)} \zeta^{-2\lambda+2} \left(\frac{c}{v}\right)^{2(\lambda+\delta)} \frac{df_{\pi\lambda}(\vartheta, \zeta)}{d\Omega}, \quad (94)$$

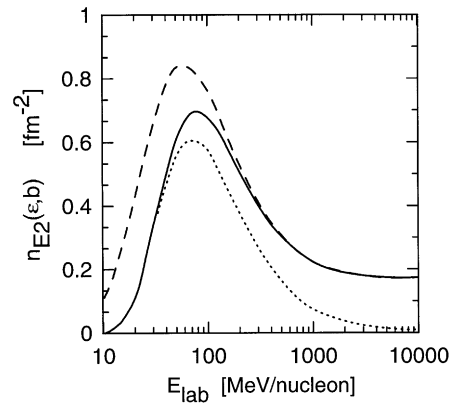
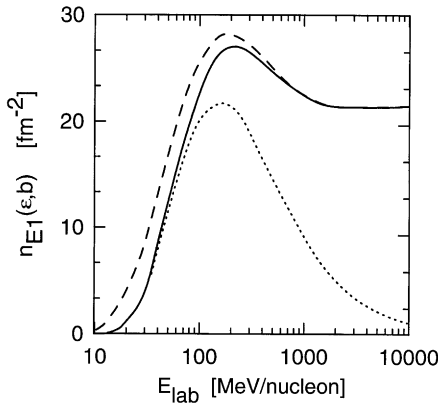


Fig. 3. Electric dipole number of equivalent photons per unit area $d^2b \equiv 2\pi b db$, with energy of 10 MeV, incident on ^{208}Pb in a collision with ^{16}O at impact parameter $b = 15$ fm, and as a function of the bombarding energy in MeV per nucleon. The dotted line and the dashed line correspond to calculations performed with the non-relativistic and with the relativistic approaches, respectively. The solid line represents a more correct calculation, as described in the text.

Fig. 4. Same as Fig. 3, but for the $E2$ multipolarity.

where $\delta = 0$ for electric, and $\delta = -1$ for magnetic multiplicities, and $\zeta = \omega a_0/v$. The non-relativistic Coulomb excitation functions $f_{\pi\lambda}(\vartheta, \zeta)$ are very well known and, e.g., are tabulated in Ref. [17], or maybe calculated numerically.

Using Eqs. (90)–(92), we make an analysis of Coulomb excitation extending from low- to high-energy collisions. As an example, we study the excitations induced by ^{16}O in $^{16}\text{O} + ^{208}\text{Pb}$ collisions. Since expression (89) is quite general, valid for all energies, under the assumption that the nuclei do not overlap, the equivalent photon numbers contain all information about the differences among the low- and the high-energy scattering. In Figs. 3–5 we show $dn_{\pi\lambda,e}$, for the $E1$ (Fig. 3), $E2$ (Fig. 4), and $M1$ (Fig. 5) multiplicities, and for the collision $^{16}\text{O} + ^{208}\text{Pb}$ with an impact parameter $b = 15$ fm. They are the equivalent photon numbers with frequency $\omega = 10$ MeV/ \hbar incident on ^{208}Pb . The dotted lines are obtained by using the non-relativistic equation (94), while the dashed lines correspond to the relativistic expressions (41)–(43). One observes that the relativistic expressions overestimate the equivalent photon numbers at low energies, while the non-relativistic expressions underestimate them at high energies. The most correct values are given by the solid lines, calculated according to Eqs. (90) and (91). They reproduce the low- and the high-energy limits, giving an improved interpolation between these limits at intermediate energies. These discrepancies are more apparent for the $E1$ and the $E2$ multiplicities. In the energy interval around 100 MeV neither the low-energy theory nor the high-energy one can reproduce well the correct values. This energy interval is indeed very sensitive to the effects of retardation and of Coulomb recoil.

At these bombarding energies, the differences between the magnitude of the non-relativistic and the correct relativistic virtual photon numbers are kept at a constant value, of about 20%, for excitation energies $\epsilon = \hbar\omega < 10$ MeV. However, they increase sharply when one reaches the

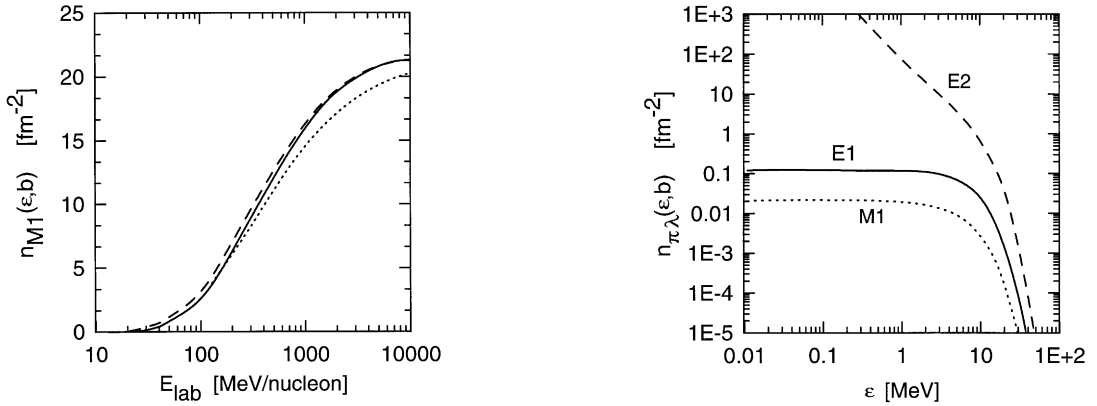


Fig. 5. Same as Fig. 3, but for the $M1$ multiplicity.

Fig. 6. Equivalent photon numbers per unit area incident on ^{208}Pb , in a collision with ^{16}O at 100A MeV and with impact parameter $b = 15$ fm, as a function of the photon energy $\hbar\omega$. The curves for the $E1$, $E2$ and $M1$ multiplicities are shown.

excitation energy of $\varepsilon = \hbar\omega > 10$ MeV. The reason is that, for such excitation energies, the adiabaticity factor becomes greater than unity ($\xi > 1$). This means that excitation energies of order of 10 MeV (like in the case of giant resonance excitation) are in the transition region from a constant behavior of the equivalent photon numbers to that of an exponential ($\sim e^{-\pi\xi}$) decay. This is more transparent in Fig. 6 where we plot the equivalent photon numbers for $E_{\text{lab}} = 100$ A MeV, $b = 15$ fm, and as a function of $\hbar\omega$. One also observes from this figure that the $E2$ multipolarity component of the electromagnetic field dominates at low frequencies. Nonetheless, over the range of $\hbar\omega$ up to some tens of MeV, the $E2$ matrix elements of excitation are much smaller than the $E1$ elements for most nuclei, and the $E2$ effects become unimportant. However, such effects are relevant for the excitation of the isoscalar $E2$ giant resonance (GQR_{is}) which have large matrix elements.

As an application of the semiclassical approach to Coulomb excitation in intermediate energy collisions, we study the excitation of giant isovector dipole resonances ($E1$) and of giant isoscalar quadrupole resonances ($E2$) in ^{208}Pb by means of the Coulomb interaction with a ^{16}O projectile. At 100A MeV the maximum scattering angle which still leads to a pure Coulomb scattering (assuming a sharp cut-off at an impact parameter $b = R_p + R_T$) is 3.9° . The cross sections are calculated by assuming a Lorentzian shape for the photonuclear cross sections:

$$\sigma_\gamma^{\pi\lambda} = \sigma_m \frac{\varepsilon^2 \Gamma^2}{(\varepsilon^2 - E_m^2)^2 + \varepsilon^2 \Gamma^2} \tag{95}$$

with σ_m chosen to reproduce the Thomas–Reiche–Kuhn sum rule for $E1$ excitations,

$$\int \sigma_\gamma^{E1}(\varepsilon) d\varepsilon \simeq 60 \frac{NZ}{A} \text{ MeV mb} \tag{96}$$

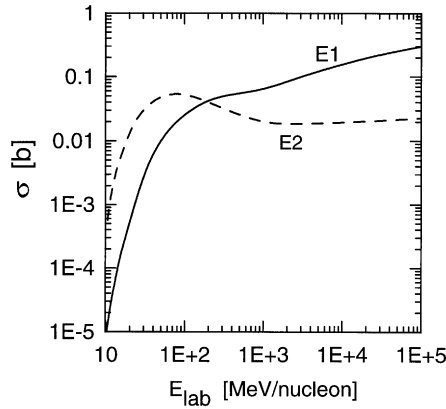


Fig. 7. Total cross sections for the excitation of giant electric dipole ($E1$) and quadrupole ($E2$) resonances in ^{208}Pb by means of the Coulomb interaction with ^{16}O , as a function of the laboratory energy.

and the energy-weighted sum rule for the quadrupole mode,

$$\int \sigma_{\gamma}^{E2}(\varepsilon) \frac{d\varepsilon}{\varepsilon^2} \simeq 0.22ZA^{2/3} \mu\text{b/MeV}. \quad (97)$$

The resonance energies are approximately given by $E_{\text{GDR}} \simeq 77 \cdot A^{-1/3} \text{MeV}$ and $E_{\text{GQR}} \simeq 63 \cdot A^{-1/3} \text{MeV}$. We use the widths $\Gamma_{\text{GDR}} = 4 \text{MeV}$ and $\Gamma_{\text{GQR}} = 2.2 \text{MeV}$ for ^{208}Pb .

We will discuss the differential cross sections as a function of the scattering angle later, when we introduce the effects of strong absorption. To obtain the total cross sections, one has to integrate the equivalent photon numbers in (90) and (91) from 0° to a maximum scattering angle θ_{max} , where the nuclear absorption sets in, or equivalently, one can integrate over the impact parameter, from a minimum value b_{min} up to infinity. Fig. 7 shows the total cross section for the excitation of giant dipole and of giant quadrupole resonances in ^{208}Pb in a collision with ^{16}O as a function of the laboratory energy per nucleon. The same average behavior of the photonuclear cross sections, as assumed in Eqs. (95) and (96), is used.

Only for the $E1$ multipolarity the angular integration can be performed analytically. One obtains¹

$$N_{E1} = \frac{2}{\pi} Z_1^2 \alpha e^{-\pi\zeta(c/v)^2} \left\{ -\zeta K_{i\zeta} K'_{i\zeta} - \frac{1}{2} (c/v)^2 \zeta^2 \right. \\ \left. \times \left(\left(\frac{\zeta}{\xi} \right)^2 K_{i\zeta}^2 + K'_{i\zeta}{}^2 - K_{i\zeta}^2 - \frac{i}{\varepsilon_0} \left(K_{i\zeta} \left(\frac{\partial K'_\mu}{\partial \mu} \right)_{\mu=i\zeta} - K'_{i\zeta} \left(\frac{\partial K_\mu}{\partial \mu} \right)_{\mu=i\zeta} \right) \right) \right\}, \quad (98)$$

¹ We observe that the original formula for the dipole case appearing in [6] has a misprinted sign in one of its terms.

where

$$\varepsilon_0 = \begin{cases} 1 & \text{for } 2a > b_{\min}, \\ R/a - 1 & \text{for } 2a < b_{\min}, \end{cases} \quad (99)$$

and $\zeta = \varepsilon_0 \zeta = \omega b_{\min} / \gamma v$.

It is easy to see that this equation reduces to Eq. (45) in the relativistic limit, when $\zeta \rightarrow 0$, $\varepsilon_0 \rightarrow \infty$.

The cross sections increase very rapidly to large values, which are already attained at intermediate energies. A salient feature is that the cross section for the excitation of giant quadrupole modes is very large at low and intermediate energies, decreasing in importance (about 10% of the $E1$ cross section) as the energy increases above 1A GeV. This occurs because the equivalent photon number for the $E2$ multipolarity is much larger than that for the $E1$ multipolarity at low collision energies. That is, $n_{E2} \gg n_{E1}$, for $v \ll c$. This has a simple explanation. Pictorially, as seen from an observer at rest, when a charged particle moves at low energies the lines of force of its corresponding electric field are isotropic, diverging from its center in all directions. This means that the field carries a large amount of tidal ($E2$) components. On the other hand, when the particle moves very fast its lines of force appear contracted in the direction perpendicular to its motion due to Lorentz contraction. For the observer this field looks like a pulse of plane waves of light. But plane waves contain all multipolarities with the same weight, and the equivalent photon numbers become all approximately equal, i.e., $n_{E1} \simeq n_{E2} \simeq n_{M1}$, and increase logarithmically with the energy for $\gamma \gg 1$. The difference in the cross sections when $\gamma \gg 1$ are then approximately equal to the difference in the relative strength of the two giant resonances $\sigma_\gamma^{E2} / \sigma_\gamma^{E1} < 0.1$. The excitation of giant magnetic monopole resonances is of less importance, since for low energies $n_{M1} \ll n_{E1}$ ($n_{M1} \simeq (v/c)^2 n_{E1}$), whereas for high energies, where $n_{M1} \simeq n_{E1}$, it will be also much smaller than the excitation of electric dipole resonances since their relative strength $\sigma_\gamma^{M1} / \sigma_\gamma^{E1}$ is much smaller than unity.

At very large energies the cross sections for the Coulomb excitation of giant resonances overcome the nuclear geometrical cross sections. Since these resonances decay mostly through particle emission or fission, this indicates that Coulomb excitation of giant resonances is a very important process to be considered in relativistic heavy ion collisions and fragmentation processes, especially in heavy ion colliders. At intermediate energies the cross sections are also large and this offers good possibilities to establish and study the properties of giant resonances.

2.4. Quantum description of Coulomb excitation at high energies

Inelastic scattering of heavy ions at intermediate energy collisions is an important tool to investigate the structure of stable and unstable nuclei. Laboratories like GANIL/France, GSI/Germany, RIKEN/Japan, and MSU/USA, frequently use this technique. The angular distribution of the inelastically scattered fragments are particularly useful to identify unambiguously the multipolarity of the interaction, and consequently the spin and parities of the excited states. In previous sections we have shown that recoil and retardation effects, are important at this energy regime. However, as shown by Bertulani and Nathan [27], in order to describe correctly the angular distribution, absorption and diffraction effects have to be included properly. Next we show how quantum mechanical effects show up in the differential cross sections.

2.4.1. Inelastic amplitudes and virtual photon numbers

Defining \mathbf{r} as the separation between the centers of mass of the two nuclei and \mathbf{r}' to be the intrinsic coordinate of the target nucleus to first-order the inelastic scattering amplitude is given by

$$f(\theta) = \frac{ik}{2\pi\hbar v} \int d^3r d^3r' \langle \Phi_{\mathbf{k}'}^{(-)}(\mathbf{r}) \phi_f(\mathbf{r}') | V_{\text{int}}(\mathbf{r}, \mathbf{r}') | \Phi_{\mathbf{k}}^{(+)}(\mathbf{r}) \phi_i(\mathbf{r}') \rangle, \quad (100)$$

where $\Phi_{\mathbf{k}'}^{(-)}(\mathbf{r})$ and $\Phi_{\mathbf{k}}^{(+)}(\mathbf{r})$ are the incoming and outgoing distorted waves, respectively, for the scattering of the center of mass of the nuclei, and $\phi(\mathbf{r}')$ is the intrinsic nuclear wave function of the target nucleus.

At intermediate energies, $\Delta E/E_{\text{lab}} \ll 1$, and forward angles, $\theta \ll 1$, we can use eikonal wave functions for the distorted waves, i.e.,

$$\Phi_{\mathbf{k}'}^{(-)*}(\mathbf{r}) \Phi_{\mathbf{k}}^{(+)}(\mathbf{r}) = \exp\{-i\mathbf{q} \cdot \mathbf{r} + i\chi(b)\}, \quad (101)$$

where

$$\chi(b) = \frac{i}{\hbar v} \int_{-\infty}^{\infty} U_N^{\text{opt}}(z', b) dz' + i\psi_C(b) \quad (102)$$

is the eikonal phase, $\mathbf{q} = \mathbf{k}' - \mathbf{k}$, U_N^{opt} is the nuclear optical potential, and $\psi_C(b)$ is the Coulomb eikonal phase. We have defined the impact parameter \mathbf{b} by $b = |\mathbf{r} \times \hat{\mathbf{z}}|$.

For light nuclei, one can assume Gaussian nuclear densities, and the Coulomb phase is given by

$$\psi_C(b) = 2 \frac{Z_1 Z_2 e^2}{\hbar v} \left\{ \ln(kb) + \frac{1}{2} E_1 \left(\frac{b^2}{R_G^2} \right) \right\}, \quad (103)$$

with $R_G^{(i)}$ equal to the size parameter of each Gaussian matter density, $R_G^2 = [R_G^{(1)}]^2 + [R_G^{(2)}]^2$, and

$$E_1(x) = \int_x^{\infty} \frac{e^{-t}}{t} dt. \quad (104)$$

The first term in Eq. (103) is the contribution to the Coulomb phase of a point-like charge distribution. It reproduces the elastic Coulomb amplitude when introduced into the eikonal expression for the elastic scattering amplitude. The second term in Eq. (103) is a correction due to the extended Gaussian charge distribution. It eliminates the divergence of the Coulomb phase at $b = 0$, so that

$$\psi_C(0) = 2 \frac{Z_1 Z_2 e^2}{\hbar v} [\ln(kR_G) - C], \quad (105)$$

where $C = 0.577$ is the Euler constant.

For heavy nuclei a “black-sphere” absorption model is more appropriate. Assuming an absorption radius R_0 , the Coulomb phase is given by

$$\begin{aligned} \chi_C(b) = 2(Z_a Z_A e^2 / \hbar v) \{ & \Theta(b - R_0) \ln(kb) + \Theta(R_0 - b) [\ln(kR_0) \\ & + \ln(1 + (1 - b^2/R_0^2)^{1/2}) - (1 - b^2/R_0^2)^{1/2} - \frac{1}{3}(1 - b^2/R_0^2)^{3/2}] \}. \end{aligned} \quad (106)$$

Again, the first term inside the parentheses is the Coulomb eikonal phase for point-like charge distributions. The second term accounts for the finite extension of the charge distributions.

Table 1

Parameters [29] for the nucleon–nucleon amplitude, $f_{NN}(\theta = 0^\circ) = (k_{NN}/4\pi) \sigma_{NN} (i + \alpha_{NN})$

| E (A MeV) | σ_{NN} (fm ²) | α_{NN} |
|-------------|----------------------------------|---------------|
| 85 | 6.1 | 1 |
| 94 | 5.5 | 1.07 |
| 120 | 4.5 | 0.7 |
| 200 | 3.2 | 0.6 |
| 342.5 | 2.84 | 0.26 |
| 425 | 3.2 | 0.36 |
| 550 | 3.62 | 0.04 |
| 650 | 4.0 | – 0.095 |
| 800 | 4.26 | – 0.075 |
| 1000 | 4.32 | – 0.275 |
| 2200 | 4.33 | – 0.33 |

For high-energy collisions, the optical potential $U(r)$ can be constructed by using the t - $\rho\rho$ approximation [28]. One gets

$$U(r) = -\frac{\hbar v}{2} \sigma_{NN} (\alpha_{NN} + i) \int \rho_1(\mathbf{r}') \rho_2(\mathbf{r} - \mathbf{r}') d^3 r', \quad (107)$$

where σ_{NN} is the nucleon–nucleon cross section, and α_{NN} is the real-to-imaginary ratio of the forward ($\theta = 0^\circ$) nucleon–nucleon scattering amplitude. A set of the experimental values of these quantities, useful for our purposes, is given in Table 1.

In Eq. (100) the interaction potential, assumed to be purely Coulomb, is given by

$$V_{\text{int}}(\mathbf{r}, \mathbf{r}') = \frac{v^\mu}{c^2} j_\mu(\mathbf{r}') \frac{e^{i\kappa|\mathbf{r}-\mathbf{r}'|}}{|\mathbf{r}-\mathbf{r}'|}, \quad (108)$$

where $v^\mu = (c, \mathbf{v})$, with \mathbf{v} equal to the projectile velocity, $\kappa = \omega/c$, and $j_\mu(\mathbf{r}')$ is the charge four-current for the intrinsic excitation of nucleus 1 by an energy of $\hbar\omega$. Inserting (101), (102) and (108) in (100) and following the same steps as in Ref. [6], one finds

$$f(\theta) = i \frac{Z_1 e k}{\gamma \hbar v} \sum_{\pi \lambda m} i^m \left(\frac{\omega}{c} \right)^\lambda \sqrt{2\lambda + 1} e^{-im\phi} \Omega_m(q) G_{\pi \lambda m} \left(\frac{c}{v} \right) \langle I_f M_f | \mathcal{M}(\pi \lambda, -m) | I_i M_i \rangle, \quad (109)$$

where $\pi \lambda m$ denotes the multipolarity, $G_{\pi \lambda m}$ are the Winther–Alder relativistic functions [18], and $\langle I_f M_f | \mathcal{M}(\pi \lambda, -m) | I_i M_i \rangle$ is the matrix element for the electromagnetic transition of multipolarity $\pi \lambda m$ from $|I_i M_i\rangle$ to $|I_f M_f\rangle$, with $E_f - E_i = \hbar\omega$. The function $\Omega_m(q)$ is given by

$$\Omega_m(q) = \int_0^\infty db b J_m(qb) K_m \left(\frac{\omega b}{\gamma v} \right) \exp\{i\chi(b)\}, \quad (110)$$

where $q = 2k \sin(\theta/2)$ is the momentum transfer, θ and ϕ are the polar and azimuthal scattering angles, respectively.

For the $E1$, $E2$ and $M1$ multipolarity, the functions $G_{\pi\lambda m}(c/v)$ are given by [18]

$$\begin{aligned} G_{E11}(x) &= -G_{E1-1}(x) = x\sqrt{8\pi}/3, & G_{E10}(x) &= -i4\sqrt{\pi(x^2-1)}/3, \\ G_{M11}(x) &= G_{M1-1}(x) = -i\sqrt{8\pi}/3, & G_{M10}(x) &= 0, \\ G_{E22}(x) &= G_{E2-2}(x) = -2x\sqrt{\pi(x^2-1)}/5, \\ G_{E21}(x) &= -G_{E2-1}(x) = i2\sqrt{\pi/6}(2x^2-1)/5, & G_{E20}(x) &= 2\sqrt{\pi(x^2-1)}/5. \end{aligned} \quad (111)$$

Using the Wigner–Eckart theorem, one can calculate the inelastic differential cross section from (109), using techniques similar to those discussed in previous sections. One obtains

$$\frac{d^2\sigma_C}{d\Omega dE_\gamma}(E_\gamma) = \frac{1}{E_\gamma} \sum_{\pi\lambda} \frac{dn_{\pi\lambda}}{d\Omega} \sigma_\gamma^{\pi\lambda}(E_\gamma) \quad (112)$$

where $\sigma_\gamma^{\pi\lambda}(E_\gamma)$ is the photonuclear cross section for the absorption of a real photon with energy E_γ by nucleus 2, and $dn_{\pi\lambda}/d\Omega$ is the virtual photon number, which is given by [27]

$$\frac{dn_{\pi\lambda}}{d\Omega} = Z_1^2 \alpha \left(\frac{\omega k}{\gamma v} \right)^2 \frac{\lambda[(2\lambda+1)!!]^2}{(2\pi)^3(\lambda+1)} \sum_m |G_{\pi\lambda m}|^2 |\Omega_m(q)|^2, \quad (113)$$

where $\alpha = e^2/\hbar c$.

The total cross section for Coulomb excitation can be obtained from Eqs. (112) and (113), using the approximation $d\Omega \simeq 2\pi q dq/k^2$, valid for small scattering angles and small energy losses. Using the closure relation for the Bessel functions, we obtain

$$\frac{d\sigma_C}{dE_\gamma}(E_\gamma) = \frac{1}{E_\gamma} \sum_{\pi\lambda} n_{\pi\lambda}(E_\gamma) \sigma_\gamma^{\pi\lambda}(E_\gamma), \quad (114)$$

where

$$n_{\pi\lambda}(\omega) = Z_1^2 \alpha \frac{\lambda[(2\lambda+1)!!]^2}{(2\pi)^3(\lambda+1)} \sum_m |G_{\pi\lambda m}|^2 g_m(\omega), \quad (115)$$

and

$$g_m(\omega) = 2\pi \left(\frac{\omega}{\gamma v} \right)^2 \int db b K_m^2 \left(\frac{\omega b}{\gamma v} \right) \exp\{-2\chi_I(b)\}, \quad (116)$$

where $\chi_I(b)$ is the imaginary part of $\chi(b)$, which is obtained from Eq. (102) and the imaginary part of the optical potential.

Before proceeding further, it is worthwhile to mention that the present calculations differ from those of previous sections by the proper inclusion of absorption. To reproduce the angular distributions of the cross sections, it is essential to include the nuclear transparency. In the limit of a black-disk approximation, the above formulas reproduce the results presented in Ref. [6]. One also observes that the Coulomb phase in the distorted waves, which is necessary for the quantitative reproduction of the experimental angular distributions, is not important for the total cross section in high-energy collisions. This fact explains why semiclassical and quantum methods give the same result for the total cross section for Coulomb excitation at relativistic energies [6]. At

intermediate energies, however, it is just this important phase which reproduces the semiclassical limit for the scattering of large- Z ions, as we shall see next. Using the semiclassical terminology, for $E_{\text{lab}} \approx 100 \text{A MeV}$ or less, the recoil in the Coulomb trajectory is relevant. At the distance of closest approach, when the Coulomb field is most effective at inducing the excitation, the ions are displaced farther from each other due to the Coulomb recoil. As we discussed before, this effect can be accounted for approximately by using the effective impact parameter $b_{\text{eff}} = b + \pi Z_1 Z_2 e^2 / 4E_{\text{lab}}$ in the semiclassical calculations. This recoil approximation can also be used in Eq. (116), replacing b by b_{eff} in the Bessel function and the nuclear phase, in order to obtain the total cross section. Since the modified Bessel function is a rapidly decreasing function of its argument, this modification leads to sizable modifications of the total cross section at intermediate energy collisions.

Finally, we point out that for very light heavy ion partners, the distortion of the scattering wavefunctions caused by the nuclear field is not important. This distortion is manifested in the diffraction peaks of the angular distributions, characteristic of strong absorption processes. If $Z_1 Z_2 \alpha \gg 1$, one can neglect the diffraction peaks in the inelastic scattering cross sections and a purely Coulomb excitation process emerges. One can gain insight into the excitation mechanism by looking at how the semiclassical limit of the excitation amplitudes emerges from the general result (113). We do this next.

2.4.2. Semiclassical limit of the excitation amplitudes

If we assume that Coulomb scattering is dominant and neglect the nuclear phase in Eq. (102), we get

$$\Omega_m(q) \simeq \int_0^\infty db b J_m(qb) K_m\left(\frac{\omega b}{\gamma v}\right) \exp\{i\psi_C(b)\} . \quad (117)$$

This integral can be done analytically by rewriting it as

$$\Omega_m(q) = \int_0^\infty db b^{1+i2\eta} J_m(qb) K_m\left(\frac{\omega b}{\gamma v}\right) , \quad (118)$$

where we used the simple form $\psi_C(b) = 2\eta \ln(kb)$, with $\eta = Z_1 Z_2 e^2 / \hbar v$. Using standard techniques found in Ref. [30], we find

$$\Omega_m(q) = 2^{2i\eta} \frac{1}{m!} \Gamma(1 + m + i\eta) \Gamma(1 + i\eta) A^m \left(\frac{\gamma v}{\omega}\right)^{2+2i\eta} F(1 + m + i\eta; 1 + i\eta; 1 + m; -A^2) , \quad (119)$$

where

$$A = q\gamma v / \omega , \quad (120)$$

and F is the hypergeometric function [30].

The connection with the semiclassical results may be obtained by using the low-momentum transfer limit

$$J_m(qb) \simeq \sqrt{\frac{2}{\pi qb}} \cos\left(qb - \frac{\pi m}{2} - \frac{\pi}{4}\right) = \frac{1}{\sqrt{2\pi qb}} \{e^{iqb} e^{-i\pi(m+1/2)/2} + e^{-iqb} e^{i\pi(m+1/2)/2}\} , \quad (121)$$

and using the stationary phase method, i.e.,

$$\int G(x)e^{i\phi(x)} dx \simeq \left(\frac{2\pi i}{\phi''(x_0)} \right)^{1/2} G(x_0)e^{i\phi(x_0)}, \quad (122)$$

where

$$d\phi(x_0)/dx = 0 \quad \text{and} \quad \phi''(x_0) = d^2\phi(x_0)/dx^2. \quad (123)$$

This result is valid for a slowly varying function $G(x)$.

Only the second term in brackets of Eq. (121) will have a positive ($b = b_0 > 0$) stationary point, and

$$\Omega_m(q) \simeq \frac{1}{\sqrt{2\pi q}} \left(\frac{2\pi i}{\phi''(b_0)} \right)^{1/2} \sqrt{b_0} K_m \left(\frac{\omega b_0}{\gamma v} \right) \exp \left\{ i\phi(b_0) + i \frac{\pi(m+1/2)}{2} \right\}, \quad (124)$$

where

$$\phi(b) = -qb + 2\eta \ln(kb). \quad (125)$$

The condition $\phi'(b_0) = 0$ implies

$$b_0 = 2\eta/q = a_0/\sin(\theta/2), \quad (126)$$

where $a_0 = Z_1 Z_2 e^2 / \mu v^2$ is half the distance of closest approach in a classical head-on collision.

We observe that the relation (126) is the same [with $\cot(\theta/2) \sim \sin^{-1}(\theta/2)$] as that between impact parameter and deflection angle of a particle following a classical Rutherford trajectory. Also,

$$\phi''(b_0) = -2\eta/b_0^2 = -q^2/2\eta, \quad (127)$$

which implies that in the semiclassical limit

$$|\Omega_m(q)|_{\text{s.c.}}^2 = \frac{4\eta^2}{q^4} K_m^2 \left(\frac{2\omega\eta}{\gamma v q} \right) = \frac{1}{k^2} \left(\frac{d\sigma}{d\Omega} \right)_{\text{Ruth}} K_m^2 \left(\frac{\omega a_0}{\gamma v \sin(\theta/2)} \right). \quad (128)$$

Using the above results, Eq. (113) becomes

$$\frac{dn_{\pi\lambda}}{d\Omega} = \left(\frac{d\sigma}{d\Omega} \right)_{\text{Ruth}} Z_1^2 \alpha \left(\frac{\omega}{\gamma v} \right)^{2\lambda} \frac{[(2\lambda+1)!!]^2}{(2\pi)^3(\lambda+1)} \sum_m |G_{\pi\lambda m}|^2 K_m^2 \left(\frac{\omega a_0}{\gamma v \sin(\theta/2)} \right). \quad (129)$$

If strong absorption is not relevant, the above formula can be used to calculate the equivalent photon numbers. The stationary value given by Eq. (126) means that the important values of b which contribute to $\Omega_m(q)$ are those close to the classical impact parameter. Dropping the index 0 from Eq. (126), we can also rewrite (129) as

$$\frac{dn_{\pi\lambda}}{2\pi b db} = Z_1^2 \alpha \left(\frac{\omega}{\gamma v} \right)^{2\lambda} \frac{[(2\lambda+1)!!]^2}{(2\pi)^3(\lambda+1)} \sum_m |G_{\pi\lambda m}|^2 K_m^2 \left(\frac{\omega b}{\gamma v} \right), \quad (130)$$

which is equal to the semi-classical expression given in Ref. [23], Eq. (A.2).

For very forward scattering angles, such that $\Lambda \ll 1$, a further approximation can be made by setting the hypergeometric function in Eq. (119) equal to unity [30], and we obtain

$$\Omega_m(q) = 2^{2in}(1/m!) \Gamma(1+m+i\eta) \Gamma(1+i\eta) A^m (\gamma v/\omega)^{2+2in} . \quad (131)$$

The main value of m in this case will be $m = 0$, for which one gets

$$\Omega_0(q) \simeq 2^{2in} \Gamma(1+i\eta) \Gamma(1+i\eta) (\gamma v/\omega)^{2+2in} = -\eta^2 2^{2in} \Gamma(i\eta) \Gamma(i\eta) (\gamma v/\omega)^{2+2in} \quad (132)$$

and

$$|\Omega_0(q)|^2 = \eta^4 (\gamma v/\omega)^4 \pi^2 / \eta^2 \sinh^2(\pi\eta) , \quad (133)$$

which, for $\eta \gg 1$, results in

$$|\Omega_0(q)|^2 = 4\pi^2 \eta^2 (\gamma v/\omega)^4 e^{-2\pi\eta} . \quad (134)$$

This result shows that in the absence of strong absorption and for $\eta \gg 1$, Coulomb excitation is strongly suppressed at $\theta = 0$. This also follows from semiclassical arguments, since $\theta \rightarrow 0$ means large impact parameters, $b \gg 1$, for which the action of the Coulomb field is weak.

2.5. Singles spectra in Coulomb excitation of GDR

In this section, we apply the formalism developed in previous sections in the analysis of the data of Ref. [31], in which a projectile of ^{17}O with an energy of $E_{\text{lab}} = 84\text{A MeV}$ excites the target nucleus ^{208}Pb to the GDR. We first seek parameters of the optical potential which fits the elastic scattering data. We use the eikonal approximation for the elastic amplitude in the form given by

$$f_{\text{el}}(\theta) = ik \int J_0(qb) \{1 - \exp[i\chi(b)]\} b db , \quad (135)$$

where J_0 is the Bessel function of zeroth order and the phase $\chi(b)$ is given by Eq. (102). In Fig. 8 we compare the calculated elastic scattering angular distribution to the data from Ref. [12]. The calculation utilized Eq. (135), with $\chi(b)$ obtained from an optical potential of a standard Woods–Saxon form with parameters

$$V_0 = 50 \text{ MeV}, \quad W_0 = 58 \text{ MeV}, \quad R_V = R_W = 8.5 \text{ fm} \quad \text{and} \quad a_V = a_W = 0.85 \text{ fm} . \quad (136)$$

The data are evidently very well reproduced by the eikonal approximation.

In order to calculate the inelastic cross section for the excitation of the GDR, we use a Lorentzian parameterization for the photoabsorption cross section of ^{208}Pb [32], assumed to be all $E1$, with $E_{\text{GDR}} = 13.5 \text{ MeV}$ and $\Gamma = 4.0 \text{ MeV}$. Inserting this form into Eq. (114) and doing the calculations implicit in Eq. (113) for $dn_{E1}/d\Omega$, we calculate the angular distribution and compare it with the data in Fig. 9. The agreement with the data is excellent, provided we adjust the overall normalization to a value corresponding to 93% of the energy weighted sum rule (EWSR) in the energy interval 7–18.9 MeV. Taking into account the $\pm 10\%$ uncertainty in the absolute cross sections quoted in Ref. [12], this is consistent with photoabsorption cross section in that energy range, for which approximately 110% of the EWSR is exhausted.

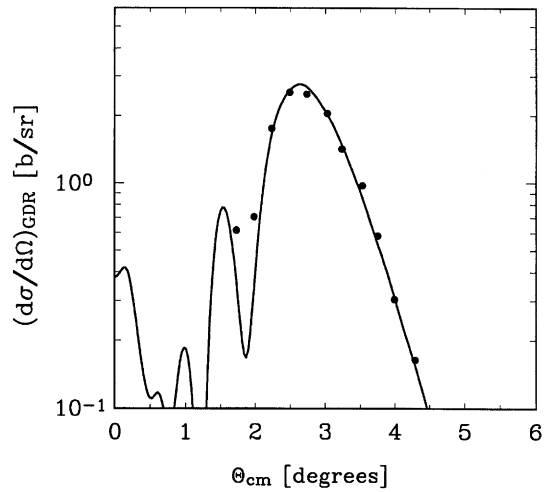
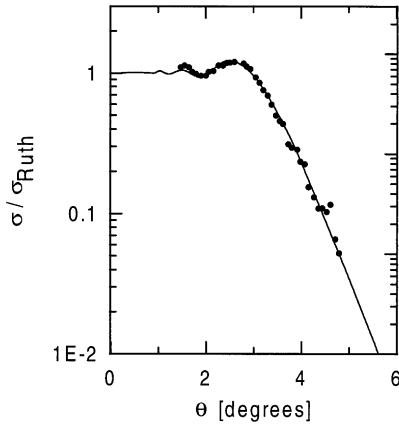


Fig. 8. Ratio to the Rutherford cross section of the elastic cross section for the $^{17}\text{O} + ^{208}\text{Pb}$ reaction at 84A MeV, as a function of the center-of-mass scattering angle. Data are from Ref. [12].

Fig. 9. Differential cross section for the excitation of the isovector giant dipole resonance in ^{208}Pb by means of ^{17}O projectiles at 84A MeV, as a function of the center-of-mass scattering angle. Data are from Ref. [12].

To unravel the effects of relativistic corrections, we repeat the previous calculations unplugging the factor $\gamma = (1 - v^2/c^2)^{-1/2}$ which appears in the expressions (115) and (116) and using the non-relativistic limit of the functions G_{E1m} , as given in Eq. (111). These modifications eliminate the relativistic corrections on the interaction potential. The result of this calculation is shown in Fig. 10 (dotted curve). For comparison, we also show the result of a full calculation, keeping the relativistic corrections (dashed curve). We observe that the two results have approximately the same pattern, except that the non-relativistic result is slightly smaller than the relativistic one. This fact may explain the discrepancy between the fit of Ref. [12] and ours as due to relativistic corrections not properly accounted for in the ECIS code [33]. In fact, if we repeat the calculation for the excitation of GDR_{iv} using the non-relativistic limit of Eqs. (115) and (116), we find that the best fit to the data is obtained by exhausting 113% of the EWSR. This value is very close to the 110% obtained by Barrette et al. [12].

In Fig. 10 we also show the result of a semiclassical calculation (solid curve) for the GDR_{iv} excitation in lead, using Eq. (129) for the virtual photon numbers. One observes that the semiclassical curve is not able to fit the experimental data. This is mainly because diffraction effects and strong absorption are not included. But the semiclassical calculation displays the region of relevance for Coulomb excitation. At small angles the scattering is dominated by large impact parameters, for which the Coulomb field is weak. Therefore, the Coulomb excitation is small and the semiclassical approximation fails. It also fails in describing the large angle data (dark side of the rainbow angle), since absorption is not treated properly. One sees that there is a “window” in the inelastic scattering data near $\theta = 2\text{--}3^\circ$ in which the semiclassical and full calculations give approximately the same cross section.

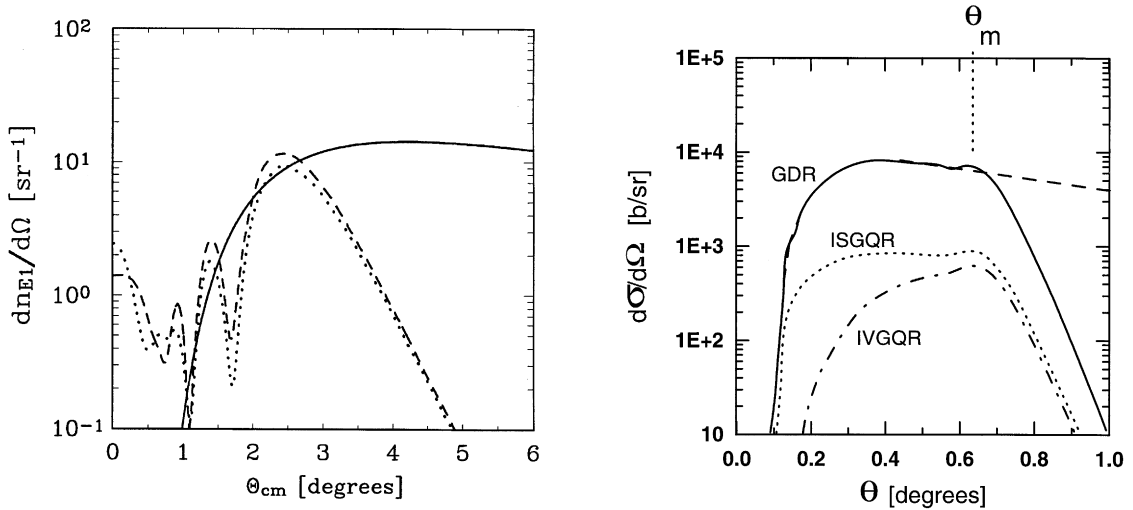


Fig. 10. Virtual photon numbers for the electric dipole multipolarity generated by 84A MeV ^{17}O projectiles incident on ^{208}Pb , as a function of the center-of-mass scattering angle. The solid curve is a semiclassical calculation. The dashed and dotted curves are eikonal calculations with and without relativistic corrections, respectively.

Fig. 11. Differential cross sections for the excitation of the giant dipole resonance (GDR), the isoscalar giant quadrupole resonance (GQR_{is}), and the isovector giant quadrupole resonance (GQR_{iv}), in Pb for the collision $^{208}\text{Pb} + ^{208}\text{Pb}$ at 640A MeV. The solid (dotted) [dashed-dotted] line is the differential cross section for the excitation of the GDR (GQR_{is}) [GQR_{iv}]. The dashed line is the result of a semiclassical calculation.

In Fig. 11 we perform the same calculation, but for the excitation of the GDR, the isoscalar giant quadrupole resonance (GQR_{is}), and the isovector quadrupole resonance (GQR_{iv}), in Pb for the collision $^{208}\text{Pb} + ^{208}\text{Pb}$ at 640A MeV. The solid (dotted) (dashed-dotted) line is the differential cross section for the excitation of the GDR (GQR_{is}) [GQR_{iv}]. The dashed line is the result of a semiclassical calculation. Here we see that a purely semiclassical calculation, using Eq. (92) is able to reproduce the quantum results up to a maximum scattering angle θ_m , at which strong absorption sets in. This justifies the use of semiclassical calculations for heavy systems, even to calculate angular distributions. The cross sections increase rapidly with increasing scattering angle, up to an approximately constant value as the maximum Coulomb scattering angle is neared. This is explained as follows. Very forward angles correspond to large impact parameter collisions in which case $\omega b/\gamma v > 1$ and the excitation of giant resonances in the nuclei is not achieved. As the impact parameter decreases, increasing the scattering angle, this adiabaticity condition is fulfilled and excitation occurs.

As discussed above, the semiclassical result works for large Z nuclei and for relativistic energies where the approximation of Eq. (117) is justified. However, angular distributions are not useful at relativistic energies since the scattering is concentrated at extremely forward angles. The quantity of interest in this case is the total inelastic cross section. If we use a sharp-cutoff model for the strong absorption, so that $\chi_l(b) = \infty$ for $b < b_{\min}$ and 0 otherwise, then Eqs. (115) and (116) yield the same result as an integration of the semiclassical expression, Eq. (130), from b_{\min} to ∞ . In fact, this result has been obtained earlier in Ref. [6].

2.6. Excitation and photon decay of the GDR

We now consider the excitation of the target nucleus to the giant dipole resonance and the subsequent photon decay of that excited nucleus, leaving the target in the ground state. Experimentally, one detects the inelastically scattered projectile in coincidence with the decay photon and demands that the energy lost by the projectile is equal to the energy of the detected photon. To the extent that the excitation mechanism is dominated by Coulomb excitation, with the exchange of a single virtual photon, this reaction is very similar to the photon scattering reaction, except that in the present case the incident photon is virtual rather than real. In this section, we investigate whether the connection between these two reactions can be formalized.

We first review the excitation mechanism. The physical situation is that of a heavy ion of energy E incident on a target. The projectile loses an energy ΔE while scattering through an angle θ . We have shown that, under the conditions $\Delta E/E \ll 1$, the cross section for excitation of the target nucleus partitions into the following expression (we assume that the contribution of the $E1$ -multipolarity is dominant):

$$\frac{d^2\sigma_C}{d\Omega dE_\gamma}(E_\gamma) = \frac{1}{E_\gamma} \frac{dn_\gamma}{d\Omega}(E_\gamma)\sigma_\gamma(E_\gamma), \quad (137)$$

where $\sigma_\gamma(E_\gamma)$ is the photonuclear cross section for the absorption of a real photon with energy $E_\gamma = \Delta E$ by the target nucleus, and the remaining terms on the right-hand side are collectively the number of virtual photons per unit energy with energy E_γ . This latter quantity depends on the kinematics of the scattered heavy ion and on the optical potential but is otherwise independent of the target degrees of freedom. This partitioning allows one to relate the excitation cross section to the photoabsorption cross section.

Now, the usual way to write the cross section $d^2\sigma_{C\gamma}/d\Omega dE_\gamma$ for the excitation of the target followed by photon decay to the ground state is simply to multiply the above expression by a branching ratio R_γ , which represents the probability that the nucleus excited to an energy E_γ will emit a photon leaving it in the ground state [13]:

$$\frac{d^2\sigma_{C\gamma}}{d\Omega dE_\gamma}(E_\gamma) = \frac{1}{E_\gamma} \frac{dn_\gamma}{d\Omega}(E_\gamma)\sigma_\gamma(E_\gamma)R_\gamma(E_\gamma). \quad (138)$$

Instead, we propose the following expression, in complete analogy with Eq. (137):

$$\frac{d^2\sigma_{C\gamma}}{d\Omega dE_\gamma}(E_\gamma) = \frac{1}{E_\gamma} \frac{dn_\gamma}{d\Omega}(E_\gamma)\sigma_{\gamma\gamma}(E_\gamma), \quad (139)$$

where $\sigma_{\gamma\gamma}(E_\gamma)$ is the cross section for the elastic scattering of photons with energy E_γ . Formally, these expressions are equivalent in that they simply define the quantity R_γ . However, if one treats R_γ literally as a branching ratio, then these expressions are equivalent only if it were true that the photon scattering cross section is just product of the photoabsorption cross section and the branching ratio. In fact, it is well-known from the theory of photon scattering that the relationship between the photoabsorption cross section and the photon scattering cross section is more complicated [34]. In particular, it is not correct to think of photon scattering as a two-step process consisting of absorption, in which the target nucleus is excited to an intermediate state of energy E_γ ,

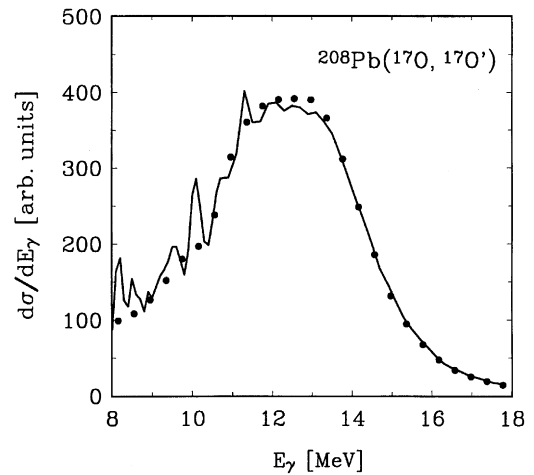
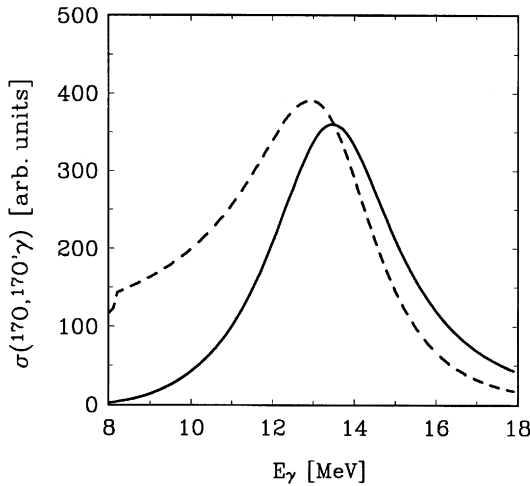


Fig. 12. Calculated cross section for the excitation followed by γ -decay of ^{208}Pb induced by ^{17}O projectiles at 84A MeV. The photoabsorption cross section was parameterized by a simple Lorentzian representing the GDR, and the statistical component of the photon decay was neglected. The solid curve uses the formalism described in the text (Eq. (139)) while the dashed curve uses a constant branching ratio for photon decay (Eq. (138)).

Fig. 13. Cross section for the excitation of the GDR without the detection of the decay photon. Data are from Ref. [13].

followed by emission, in which the emitted photon has the same energy E_γ . Since the intermediate state is not observable, one must sum over all possible intermediate states and not just those allowed by conservation of energy. Now, if the energy E_γ happens to coincide with a narrow level, then that level will completely dominate in the sum over intermediate states. In that case, it is proper to regard the scattering as a two-step process in the manner described above, and the two expressions for the cross section will be equal. However, for E_γ in the nuclear continuum region (e.g., in the region of the GDR), this will not be the case, as demonstrated in the following discussion.

We again consider the inelastic scattering of ^{17}O projectiles of energy $E_{\text{lab}} = 84$ MeV/nucleon from a ^{208}Pb nucleus at an angle of 2.5° . We use Eq. (113) to calculate the $E1$ virtual photon number and we use a Lorentzian parameterization of the GDR of ^{208}Pb . We calculate R_γ and $\sigma_{\gamma\gamma}$ according to the prescriptions of Refs. [13] and [34], respectively; in both cases we neglect the statistical contribution to the photon decay. The results are compared in Fig. 12, where it is very evident that they make very different predictions for the cross section, especially in the wings of the GDR.

We next use our expression to compare directly with the data of Ref. [13]. For this purpose, we again calculate $\sigma_{\gamma\gamma}$ using the formalism of Ref. [34], which relates $\sigma_{\gamma\gamma}$ to the total photoabsorption. For the latter, we use the numerically defined data set of Ref. [32] rather than a Lorentzian parameterization. The effect of the underlying compound nuclear levels (i.e., the statistical contribution to the photon scattering) is also included. The calculation is compared to the data in Figs. 13 and 14. Fig. 13 shows the cross section for the excitation of the GDR without the detection

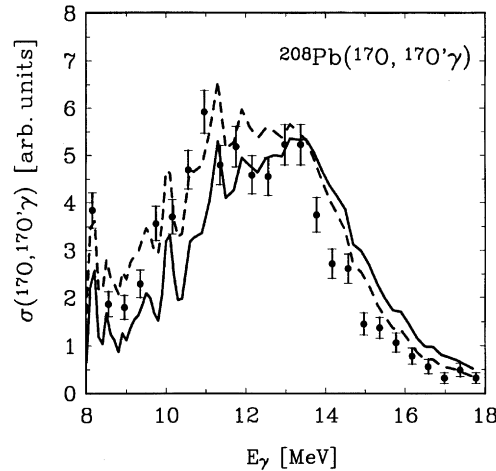


Fig. 14. Cross section for excitation followed by γ -decay of ^{208}Pb by ^{17}O projectiles at 84A MeV. The solid (dashed) line includes (excludes) the Thomson scattering amplitude. Data are from Ref. [13].

of the decay photon. The agreement with the data is excellent, giving us confidence that our calculation of the virtual photon number as a function of E_γ is correct. Fig. 14 shows the cross section for the excitation-decay process as a function of E_γ . Although the qualitative trend of the data are well described, the calculation systematically overpredicts the cross section on the high-energy side of the GDR (solid curve). If the Thompson amplitude is not included in $\sigma_{\gamma\gamma}$, the calculation is in significantly better agreement with the data (dashed curve).

2.7. Nuclear excitation and strong absorption

Up to this point we have only considered the Coulomb excitation of the nuclei, without accounting for nuclear excitation. But, in peripheral collisions, the nuclear interaction between the ions can also induce excitations. This can be easily calculated in a vibrational model. The amplitude for the excitation of a vibrational mode by the nuclear interaction in relativistic heavy ion collisions can be obtained assuming that a residual interaction U between the projectile and the target exists, and that it is weak. According to the Bohr–Mottelson particle–vibrator coupling model, the matrix element for the transition $i \rightarrow f$ is given by

$$V_{fi}^{N(\lambda\mu)}(\mathbf{r}) \equiv \langle I_f M_f | U | I_i M_i \rangle = \delta_\lambda / (\sqrt{2\lambda + 1}) \langle I_f M_f | Y_{\lambda\mu} | I_i M_i \rangle Y_{\lambda\mu}(\hat{\mathbf{r}}) U_\lambda(r), \quad (140)$$

where $\delta_\lambda = \beta_\lambda R$ is the vibrational amplitude, or *deformation length*, R is the nuclear radius, and $U_\lambda(r)$ is the transition potential.

The deformation length δ_λ can be directly related to the reduced matrix elements for electromagnetic transitions. Using well-known sum-rules for these matrix elements one finds a relation between the deformation length and the nuclear masses and sizes. For isoscalar excitations one gets [35]

$$\delta_0^2 = 2\pi \frac{\hbar^2}{m_N \langle r^2 \rangle} \frac{1}{AE_x}, \quad \delta_{\lambda \geq 2}^2 = \frac{2\pi}{3} \frac{\hbar^2}{m_N} \lambda(2\lambda + 1) \frac{1}{AE_x}, \quad (141)$$

where A is the atomic number, $\langle r^2 \rangle$ is the r.m.s. radius of the nucleus, and E_x is the excitation energy.

The transition potentials for nuclear excitations can be related to the optical potential in the elastic channel. The basic idea is that the interaction between the projectile and the target induces surface vibrations in the target. Only the contact region between the nuclei in grazing collisions is of relevance. One thus expects that the interaction potential is proportional to the derivatives of the optical potential in the elastic channel, which peak at the surface. This is discussed in detail in Ref. [35]. The transition potentials for isoscalar excitations are

$$U_0(r) = 3U_{\text{opt}}(r) + r \, dU_{\text{opt}}(r)/dr, \quad (142)$$

for monopole, and

$$U_2(r) = dU_{\text{opt}}(r)/dr, \quad (143)$$

for quadrupole modes.

For dipole isovector excitations

$$\delta_1 = \frac{\pi}{2} \frac{\hbar^2}{m_N} \frac{A}{NZ} \frac{1}{E_x}, \quad (144)$$

where Z (N) is the charge (neutron) number. The transition potential in this case is [35]

$$U_1(r) = \chi \left(\frac{N-Z}{A} \right) \left(\frac{dU_{\text{opt}}}{dr} + \frac{1}{3} R_0 \frac{d^2 U_{\text{opt}}}{dr^2} \right), \quad (145)$$

where the factor χ depends on the difference between the proton and the neutron matter radii as

$$\chi \frac{2(N-Z)}{3A} = \frac{R_n - R_p}{\frac{1}{2}(R_n + R_p)} = \frac{\Delta R_{np}}{R_0}. \quad (146)$$

Thus, the strength of isovector excitations increases with the difference between the neutron and the proton matter radii. This difference is accentuated for neutron-rich nuclei and should be a good test for the quantity ΔR_{np} which enters the above equations.

The time dependence of the matrix elements above can be obtained by making a Lorentz boost. Since the potentials $U_\lambda[r(t)]$ peak strongly at $t = 0$, we can safely approximate $\theta(t) \simeq \theta(t = 0) = \pi/2$ in the spherical harmonic of Eq. (140). One gets

$$V_{fi}^{N(\lambda\mu)}(\mathbf{r}) \equiv \langle I_f M_f | U | I_i M_i \rangle = \gamma \frac{\delta_\lambda}{\sqrt{2\lambda + 1}} \langle I_f M_f | Y_{\lambda\mu} | I_i M_i \rangle Y_{\lambda\mu} \left(\theta = \frac{\pi}{2} \right) U_\lambda[r(t)], \quad (147)$$

where $r(t) = \sqrt{b^2 + \gamma^2 v^2 t^2}$.

Using the Wigner–Eckart theorem, the matrix element of the spherical harmonics becomes

$$\langle I_f M_f | Y_{\lambda\mu} | I_i M_i \rangle = (-1)^{I_f - M_f} \left[\frac{(2I_i + 1)(2\lambda + 1)}{4\pi(2I_f + 1)} \right]^{1/2} \begin{pmatrix} I_f & \lambda & I_i \\ -M_f & \mu & M \end{pmatrix} \begin{pmatrix} I_f & \lambda & I_i \\ 0 & 0 & 0 \end{pmatrix}. \quad (148)$$

For high-energy collisions, the optical potential $U(r)$ can be constructed by using the t - $\rho\rho$ approximation [28], as given by Eq. (107).

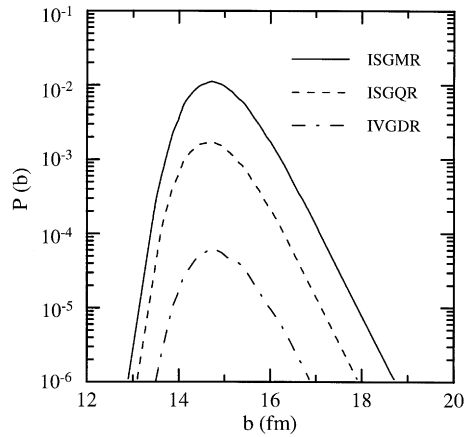
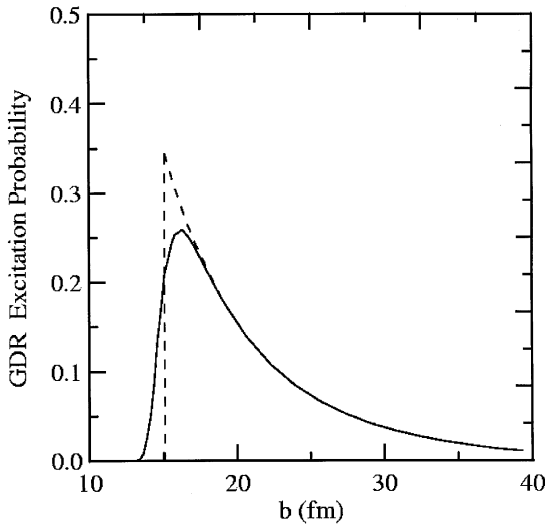


Fig. 15. The GDR Coulomb excitation probabilities as functions of the impact parameter, for sharp and smooth absorptions. The system is ^{208}Pb (640A MeV) + ^{208}Pb .

Fig. 16. Nuclear excitation probabilities, as functions of the impact parameter, of the isoscalar giant monopole resonance (GMR_{is}), the GDR_{iv}, and the GQR_{is}, in ^{208}Pb for the collision ^{208}Pb + ^{208}Pb at 640A MeV.

We are not interested here in diffraction and refraction effects in the scattering, but on the excitation probabilities for a given impact parameter. The strong absorption occurring in collisions with small impact parameters can be included. This can be done by using the eikonal approximation and the optical potential, given by Eq. (107). The practical result is that the excitation probabilities for a given impact parameter b , including the sum of the nuclear and the Coulomb contributions to the excitation, are given by

$$P_{fi}(b) = |a_{fi}^C(b) + a_{fi}^N(b)|^2 \exp \left\{ - \sigma_{NN} \int dz \int d^3r' \rho_1(\mathbf{r}') \rho_2(\mathbf{r} - \mathbf{r}') \right\}, \quad (149)$$

where $r = \sqrt{b^2 + z^2}$. The corresponding excitation cross sections are obtained by an integration of the above equation over impact parameters.

2.8. Nucleon removal in peripheral relativistic heavy ion collisions

In Fig. 15 we plot the GDR excitation probability in Pb as a function of the impact parameter, for the system ^{208}Pb + ^{208}Pb at 640A MeV. We use 100% of the sum rule to calculate the $B(E1)$ -value for the electromagnetic excitation of an isolated GDR state at 13.5 MeV. In the solid line, we consider absorption according to Eq. (149). In the construction of the optical potential we used the g.s. densities calculated from the droplet model of Myers and Swiatecki [36] in accordance with Shen et al. [37]. We will call it by soft-spheres model.

As shown in Ref. [38], this parametrization yields the best agreement between experiment and theory. The dashed line does not include absorption. To simulate strong absorption at low impact parameters, we use $b_{\min} = 15.1$ fm as a lower limit in the impact parameter integration of Eq. (5). This value was chosen such as to lead to the same cross section as that obtained from the solid line. However, a more detailed comparison of the soft-sphere model for strong absorption and a simple semiclassical calculation, based on a single parameter b_{\min} , is described next [38].

In Fig. 16, we plot the nuclear contributions to the excitation probability as a function of the impact parameter. We study the excitation of the isoscalar giant monopole resonance (GMR_{is}), the GDR_{iv}, and the GQR_{is}, in lead for the collision $^{208}\text{Pb} + ^{208}\text{Pb}$ at 640A MeV. The GMR_{is} in ^{208}Pb is located at 13.8 MeV. As discussed previously, isovector excitations are suppressed in nuclear excitation processes, due to the approximate charge independence of the nuclear interaction. We use the formalism of this section, with the deformation parameters such that 100% of the sum rule is exhausted. This corresponds to the monopole amplitude $\delta_0 = 0.054$. The GDR_{iv} and GQR_{is} deformation parameters are $\delta_1 = 0.31$ fm and $\delta_2 = 0.625$ fm, respectively. The GQR_{iv} excitation probability is much smaller than the other excitation probabilities and is, therefore, not shown. The nuclear excitation is peaked at the grazing impact parameter and is only relevant within an impact parameter range of ~ 2 fm. Comparing to Fig. 15, we see that these excitation probabilities are orders of magnitude smaller than those for Coulomb excitation. Consequently, the corresponding cross sections are much smaller. We get 14.8 mb for the isovector GDR, 2.3 mb for the GQR_{is}, and 2.3 mb for the GDR_{iv}. The interference between the nuclear and the Coulomb excitation is also small and can be neglected.

Since they are high lying states above the continuum, giant resonances mostly decay by particle emission (mainly neutron emission in heavy nuclei). Therefore data on neutron removal in relativistic heavy ion collisions is an appropriate comparison between theory and experiment. As we have seen, above, nuclear excitation of GR's contribute very little to the cross section, as compared to Coulomb excitation. However, strong interactions at peripheral collisions also contribute to “direct” knockout (or stripping) of neutrons, and also should be considered. It has been observed [6], however, that neutron removal cross sections induced by strong interactions scale with $A_1^{1/3} + A_2^{1/3}$, while the Coulomb excitation cross sections scale with the projectile's charge as Z_2^2 , approximately. One can thus separate the nuclear contribution for the nucleon removal of a target (or projectile) by measuring the cross sections for different projectiles (or targets).

In the semiclassical approach, the total cross section for relativistic Coulomb excitation is obtained by integrating the excitation probabilities over impact parameter, starting from a minimum value b_{\min} . It is assumed that below this minimum value the interaction is exclusively due to the strong interaction (“sharp-cutoff” approximation). It has been found that with this approximation the Coulomb cross sections are very sensitive to the parameterization of the minimum impact parameter [39–42].

One commonly used parameterization at relativistic energies is that of Benesh et al. [43], fitted to Glauber-type calculations and reading

$$b_{\min}^{\text{BCV}} = 1.35(A_p^{1/3} + A_t^{1/3} - 0.75(A_p^{-1/3} + A_t^{-1/3})) \text{ fm} \quad (150)$$

which we refer to hereafter as “BCV”. In Ref. [43] a detailed study has been made concerning the parametrization procedure of the minimum impact parameter. It was also found that the nuclear

contribution to the neutron removal channels in peripheral collisions has a negligible interference with the Coulomb excitation mechanism. This is a very useful result since the Coulomb and nuclear part of the cross sections may be treated separately.

The other parametrization is that of Kox et al. [44] which reproduced well measured total reaction cross sections of light and medium-mass systems:

$$b_{\min}^{\text{Kox}} = 1.1 \left(A_p^{1/3} + A_t^{1/3} + 1.85 \frac{A_p^{1/3} A_t^{1/3}}{A_p^{1/3} + A_t^{1/3}} - 1.9 \right) \text{fm} . \quad (151)$$

This parametrization has been used previously [41] and a reasonable agreement with the measured data for 1n cross sections was found. It should be noted, however, that the Kox parametrization of total interaction cross sections has been derived mainly from experiments with light projectiles and that its application to heavy systems involves an extrapolation into a region where no data points are available.

To achieve a good a comparison with experimental data on neutron-removal cross sections we will use the experimental photo-neutron emission cross sections from Refs. [32,45]. A Lorentzian fit to the (γ, n) -data is used to parameterize the GDR in gold. The parameters are 13.72 MeV excitation energy, a width of 4.61 MeV, and a strength of 128% of the TRK sum rule. The Lorentz parameters for the isoscalar (isovector) GQR are taken as 10.8 (23.0) MeV for the excitation energy, 2.9 (7.0) MeV for the width, and we assume 95% exhaustion of the respective sum rules [5]. With these parameters we calculate the excitation cross sections $d\sigma(E)/dE$ for dipole and quadrupole excitations. The respective neutron emission cross sections are given by

$$\sigma_n = \int \frac{d\sigma(E)}{dE} f_n(E) dE , \quad (152)$$

where $f_n(E)$ is the probability to evaporate one neutron at excitation energy E . $f_n(E)$ is taken from the experimental (γ, n) -data at low E and from a statistical decay calculation with the code HIVAP [46] for excitation energies above 20 MeV. Since the three-neutron emission threshold in gold is above the energy of the GDR state, this channel is fed mainly by the two-phonon excitation mechanism, while the 1n cross section is dominated by the excitation of the GDR.

We expect that the BCV parametrization of b_{\min} should yield similar results as the soft-spheres calculation since it was derived in fitting the complementary process, the nuclear interaction, calculated also with Glauber theory. Fig. 17 shows that this expectation could be verified: the soft-spheres calculation for 1n-removal from ^{197}Au by ED processes (upper full curve) is almost indistinguishable from a sharp-cutoff calculation using b_{\min}^{BCV} (upper dotted curve). This remarkable agreement tells us that for practical purposes we can avoid the extra numerical complication connected with the use of a soft spheres model and corroborates the use of b_{\min}^{BCV} in sharp-cutoff calculations in earlier works [47,48]. We also think that the soft-spheres calculation (and the sharp-cutoff calculation using b_{\min}^{BCV}) is physically better justified than the Kox parametrization [44] since the former is derived from realistic nuclear density distributions, whereas the latter is an extrapolation of measured total reaction cross sections into a region where no data points are available. We will return later to discuss the other data points of Fig. 17 when we treat the problem of the excitation of multiphonon states. However, it is worthwhile noticing that a point in the above

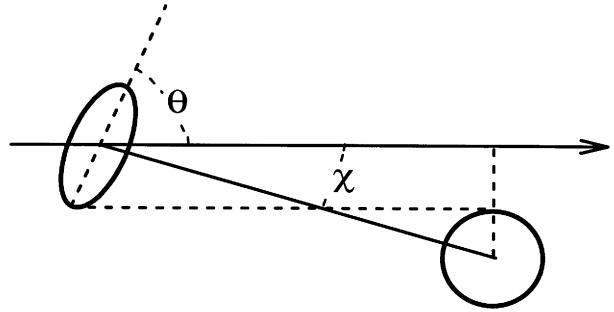
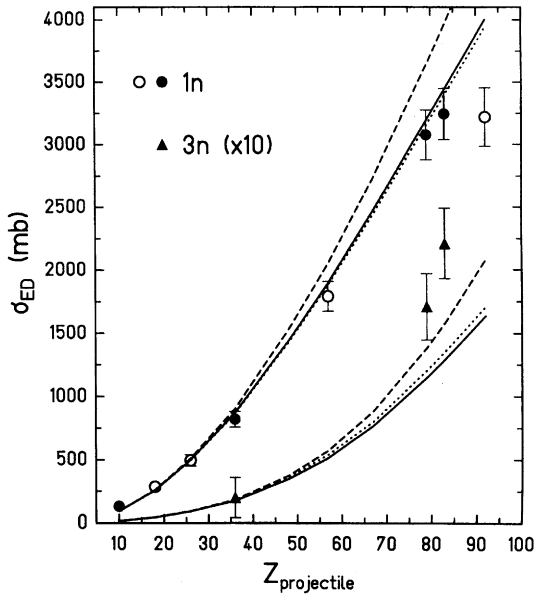


Fig. 17. Experimental 1n- and 3n-removal cross sections for ^{197}Au bombarded with relativistic projectiles (from Ref. [38]) in comparison with theoretical calculations from this work (solid curve: “soft-spheres” model; dotted curve: “sharp-cutoff” model with b_{\min}^{BCV} from Eq. (150)). For completeness, we also show a sharp-cutoff calculation with b_{\min}^{Kox} (Eq. (151)) used in Ref. [41].

Fig. 18. A nuclear target is Coulomb excited by a fast moving deformed projectile. Besides the angle θ , the orientation of the projectile also includes an azimuthal angle ϕ which can rotate its symmetry axis out the scattering plane. For simplicity, this is not shown. χ is the angular position of the c.m. of the projectile with respect to the target.

curve, for uranium targets, is not well reproduced by the theory. In fact, this has been observed in other experiments [49], and deserves a special treatment.

2.9. Excitation by a deformed nucleus

Either by using the soft-sphere model, or by means of a semiclassical calculation, Coulomb excitation by a relativistic projectile, or target, is well described theoretically if the charge distribution of the projectile is spherically symmetric [50].

However, there was found a discrepancy between theory and experiment with data with deformed projectiles, as measured by Justice et al. [49] for uranium projectiles. This problem was studied theoretically by Bertulani in [51], and we will briefly discuss it here. To obtain a qualitative insight of the effects we shall consider a prolate deformed projectile with a variable deformation.

In the frame of reference of the projectile the Coulomb field at a position \mathbf{r} with respect to the center-of-charge of the distribution is given by

$$\phi(\mathbf{r}) = 4\pi \sum_{\lambda,\mu} \frac{1}{2\lambda + 1} \frac{1}{r^{\lambda+1}} Y_{\lambda\mu}^*(\theta, \phi) \mathcal{M}(E\lambda\mu), \tag{153}$$

where

$$\mathcal{M}(E\lambda\mu) = \int \rho(\mathbf{r}') r'^{\lambda} Y_{\lambda\mu}(\hat{\mathbf{r}}') d^3r' , \quad (154)$$

with $\rho(\mathbf{r})$ equal to the ground-state charge distribution of the projectile. For simplicity, we will consider a uniform spheroidal charge distribution with the z -axis along the symmetry axis. The charge distribution drops to zero for distances to the center greater than the angle-dependent radius

$$R(\theta) = R_0(1 + \beta Y_{20}(\theta)) . \quad (155)$$

In lowest order in the multipole expansion, Eq. (153) becomes

$$\phi(\mathbf{r}) = \frac{Z_1 e}{r} + \sqrt{\frac{\pi}{5}} \frac{1}{r^3} Y_{20}(\theta) Q_0^{(c)} , \quad (156)$$

where $Q_0^{(c)}$ is the quadrupole moment of the charge distribution,

$$Q_0^{(c)} = \frac{3}{\sqrt{5\pi}} Z_1 e R_0^2 \beta (1 + 0.16\beta) + \mathcal{O}(\beta^2) . \quad (157)$$

To obtain the (time-dependent) field in the frame of reference of the target we perform a Lorentz transformation of Eq. (156). For a straight-line trajectory one finds

$$\phi(\mathbf{r}', t) = \frac{\gamma Z_1 e}{r'} + \gamma \sqrt{\frac{\pi}{5}} \frac{1}{r'^3} Y_{20}(\theta') Q_0^{(c)} \quad (158)$$

where $r' = \sqrt{b^2 + \gamma^2 v^2 t^2}$, with b equal to the impact parameter, v the projectile velocity, and $\gamma = (1 - v^2/c^2)^{-1/2}$.

The first term in the above equation is the well-known Liénard–Wiechert potential of a relativistic charge. It gives rise to monopole–multipole excitations of the target, which we have discussed so far. The second term accounts for quadrupole–multipole excitations of the target and is a correction due to the deformation of the projectile. This field will depend on the orientation of the projectile with respect to its trajectory (see Fig. 18). We can separate the orientation angles from the angular position of the projectile (along its trajectory) with respect to the target by using the identity

$$Y_{20}(\theta') = \sqrt{\frac{4\pi}{5}} \sum_m Y_{2m}(\theta, \phi) Y_{2m}(\chi', 0) , \quad (159)$$

where (θ, ϕ) denotes the orientation of the projectile symmetry axis with respect to the bombarding axis and $\chi' = \cos^{-1} [\gamma vt/r'(t)]$.

The dipole excitation of the target is the most relevant and we shall restrict ourselves to this case only [6]. At a point $\mathbf{r} \equiv (x, y, z)$ from the center of mass of the target the field is obtained by replacing $\mathbf{r}' = (b, 0, \gamma vt)$ by $[b - x, y, \gamma(vt - z)]$ in Eq. (158). The excitation amplitude to first order is given by Eq. (62). Using the continuity equation and expanding (62) to lowest order in \mathbf{r} we find

$$a_{fi} = a_{fi}^{(1)} + a_{fi}^{(2)} \quad (160)$$

where

$$a_{fi}^{(1)} = -i \frac{2Z_1 e}{\hbar v} \frac{\xi}{b} \left\{ K_1(\xi) D_{fi}^{(x)} + i \frac{1}{\gamma} K_0(\xi) D_{fi}^{(z)} \right\} \quad (161)$$

and

$$a_{fi}^{(2)} = -i \frac{4\pi}{5} \frac{Q_0^{(c)}}{\hbar v} \frac{\xi^2}{b^3} \left\{ K_2(\xi) D_{fi}^{(x)} + i \frac{1}{\gamma} K_1(\xi) D_{fi}^{(z)} \right\} \sum_m Y_{2m}(\theta, \phi) Y_{2m}\left(\frac{\pi}{2}, 0\right), \quad (162)$$

where $\xi = \omega b/\gamma v$ and K_i is the modified Bessel function of order i . To simplify the notation, we have used the Cartesian definition of the matrix elements. The dipole matrix elements for the nuclear excitation are given by

$$D_{fi}^{x(z)} = \langle f | x(z) | i \rangle. \quad (163)$$

In terms of the spherical coordinates, $D_{fi}^{(x)} = \sqrt{2\pi/3} [\mathcal{M}_{fi}(E1, -1) - \mathcal{M}_{fi}(E1, 1)]$, and $D_{fi}^{(z)} = \sqrt{4\pi/3} \mathcal{M}_{fi}(E1, 0)$. Thus, Eq. (161) is equal to Eq. (31).

In expression (162) we have used the approximation $Y_{2m}(\chi, 0) \simeq Y_{2m}(\pi/2, 0)$ which is valid for high-energy collisions since the quadrupole field is strongly peaked at $t = 0$, corresponding to the distance of closet approach. Eqs. (161) and (162) allow us to calculate the dipole excitation cross section by integrating their absolute squares over impact parameter, starting from a minimum impact parameter for which the strong interaction sets in. Neglecting the diffuseness of the matter distribution of the nuclei we can write (see Fig. 18)

$$b_{\min}(\theta) \simeq R_1 + R_2 [1 + \beta Y_{20}(\pi/2 + \theta)] \quad (164)$$

with the nuclear radii given by $R_i = 1.2A_i^{1/3}$ fm. The total cross section is

$$\sigma = 2\pi \int_{b_{\min}(\theta)} db b \langle |a_{fi}(b, \Omega)|^2 \rangle \quad (165)$$

where the $\langle \dots \rangle$ sign means that an average over all the possible orientations of the projectile, i.e., over all angles $\Omega = (\theta, \phi)$, is done.

We will apply the above formalism to the Coulomb excitation of ^{208}Pb by ^{238}U projectiles. We will give the ^{238}U an artificial deformation in the range $\beta = 0-1$ to check the dependence of the cross sections with this parameter. The cross section given above contains three terms: $\sigma = \sigma_1 + \sigma_2 + \sigma_{12}$. σ_1 is due to the monopole–dipole excitation amplitude, σ_2 is due to the quadrupole–dipole excitation amplitude, and σ_{12} is the interference between them.

In Fig. 19 we present the results for the numerical calculation of the quantity

$$A = 100 \times (\sigma_1 - \sigma_1^{\beta=0}) / \sigma_1^{\beta=0} \quad (166)$$

which is the percent correction of dipole excitations in ^{208}Pb by a uranium projectile due to the average over the orientation of the projectile. $\sigma_1^{\beta=0}$ is the cross section for $\beta = 0$. We present results for three bombarding energies, 10A GeV, 1A GeV and 100A MeV, and as a function of β . The quantity defined by Eq. (166) is independent of the nature of the state excited, since the dipole matrix elements cancel out. They depend on the energy of the state. In order to see how the effect depends qualitatively on the energy of the state we used three different excitation energies $E_{fi} = 1$,

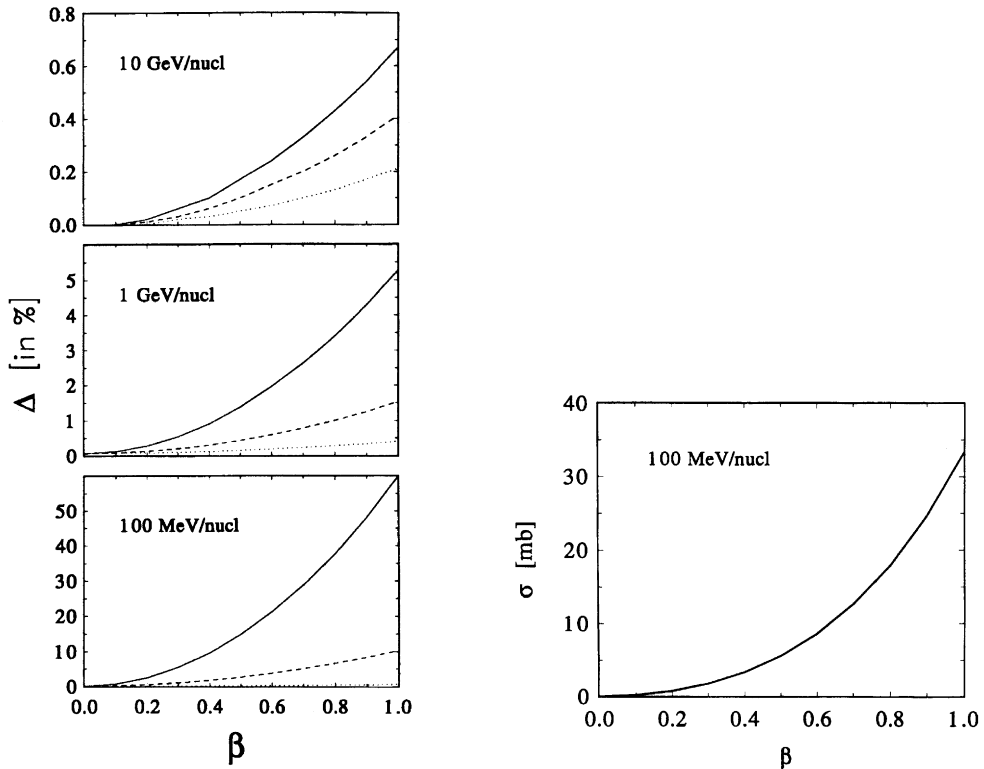


Fig. 19. Percent increase of the Coulomb excitation cross section of dipole states in ^{208}Pb due to the dependence of the minimum impact parameter on the deformation. The effect is shown for ^{238}U projectiles at 100A MeV, 1A GeV and 10A GeV, respectively, and as a function of the deformation parameter β . The solid (dashed) [dotted] line corresponds to an excitation energy of 25 (10) [1] MeV. For the actual deformation of ^{208}U , $\beta \simeq 0.3$, the effect is small.

Fig. 20. Coulomb excitation cross section of a giant dipole resonance in ^{208}Pb due to the quadrupole–dipole interaction with 100A MeV uranium projectiles, as a function of the deformation parameter β . These cross section are averaged over all possible orientations of the projectile.

10 and 25 MeV, respectively. These correspond to the dotted, dashed and solid lines in Fig. 19, respectively.

One observes from Fig. 19 that the deformation effect accounted for by an average of the minimum impact parameter which enters Eq. (165) increases the magnitude of the cross section. Thus the average is equivalent to a smaller “effective” impact parameter, since the cross sections increase with decreasing values of b_{\min} . The effect is larger the greater the excitation energy is. This effect also decreases with the bombarding energy. For very high bombarding energies it is very small even for the largest deformation. These results can be explained as follows. The Coulomb excitation cross section at very high bombarding energies, or very small excitation energies, is proportional to $\ln[\omega b_{\min}(\theta)/\gamma v]$. Averaging over orientation of the projectile means an average of $\ln(b_{\min})$ due to the additivity law of the logarithm. One can easily do this average and the net result is a rescaling of b_{\min} as $f b_{\min}$, with f smaller, but very close to one.

Table 2

Cross sections (in mb) for Coulomb excitation of the giant dipole resonance in ^{208}Pb by ^{238}U projectiles at 100A MeV. In the second (third) column the cross sections are due to the monopole (quadrupole)–dipole interaction. The last column is the total cross section. An average over the orientation of the projectile was done. A realistic value of the deformation of ^{238}U corresponds to $\beta \simeq 0.3$. But, a variation of β is used to obtain an insight of the magnitude of the effect

| β | σ_1 (mb) | σ_2 (mb) | σ (mb) |
|---------|-----------------|-----------------|---------------|
| 0 | 1171 | 0 | 1171 |
| 0.1 | 1173 | 0.179 | 1174 |
| 0.2 | 1179 | 0.748 | 1184 |
| 0.3 | 1189 | 1.773 | 1200 |
| 0.4 | 1202 | 3.34 | 1224 |
| 0.5 | 1220 | 5.57 | 1242 |
| 0.6 | 1241 | 8.61 | 1291 |
| 0.7 | 1265 | 12.6 | 1335 |
| 0.8 | 1294 | 17.9 | 1389 |
| 0.9 | 1326 | 24.7 | 1446 |
| 1 | 1362 | 33.3 | 1522 |

For high excitation energies, or small bombarding energies, the cross section is proportional to $\exp\{-2\omega b_{\min}(\theta)/\gamma v\}$ due to the adiabaticity condition [18]. Thus, in these situations, the cross section is strongly dependent on the average over orientation due to the strong variation of the exponential function with the argument.

Now we consider the effect of the second term of Eq. (158), namely of the quadrupole–dipole excitations. In Fig. 20 we show the excitation of a giant resonance dipole state in lead ($E_{fi} = 13.5$ MeV) due to the second term Eq. (158), as a function the deformation parameter β and for a bombarding energy of 100A MeV. We assume that the giant dipole state exhausts fully the TRK sum rule, Eq. (96), in lead. Now the average over orientation also includes the dependence of the quadrupole–dipole interaction on $\Omega = (\theta, \phi)$. As expected the cross section increases with β . But it is small as compared to the monopole–dipole excitations even for a large deformation. At this beam energy the monopole–dipole excitation is of order of 1 barn.

The total cross section contains an interference between the amplitudes $a_{fi}^{(1)}$ and $a_{fi}^{(2)}$. This is shown in Table 2 for 100A MeV for which the effect is larger. The second column gives the cross sections for monopole–dipole excitations of a giant resonance dipole state in lead. The effect of the orientation average can be seen as an increase of the cross section as compared to the value in the first row (zero deformation). For $\beta = 0.3$ which is approximately the deformation parameter for ^{238}U the correction to the cross section is negligible. In the third column the cross section for quadrupole–dipole excitation are given. They are also much smaller than those for the monopole–dipole excitations. The total cross sections, given in the last column, are also little dependent on the effect of the deformation. For $\beta = 0.3$ it corresponds to an increase of 3% of the value of the original cross section (first row). This effect also decreases with the bombarding energy. For 1A GeV, $\sigma^{\beta=0} = 5922$ mb, while $\sigma = 5932$ mb for $\beta = 0.3$, with all effects included.

In conclusion, the effect of excitation by a deformed projectile, which can be studied by averaging over the projectile orientation, is to increase slightly the cross sections. The inclusion of

the quadrupole–dipole interaction increases the cross section, too. However, these corrections are small for realistic deformations. They cannot be responsible for the large deviations of the experimental values of the Coulomb fragmentation cross sections from the standard theory [6,18], as has been observed [41,49] for deformed projectiles.

3. Heavy ion excitation of multiphonon resonances

3.1. Introduction

Much of the interest on multiphonon resonances relies on the possibility of looking at exotic particle decay of these states. For example, in Ref. [52], a hydrodynamical model was used to predict the proton and neutron dynamical densities in a multiphonon state of a nucleus. Large proton and neutron excesses at the surface are developed in a multiphonon state. Thus, the emission of exotic clusters from the decay of these states are a natural possibility. A more classical point of view is that the Lorentz contracted Coulomb field in a peripheral relativistic heavy ion collision acts as a hammer on the protons of the nuclei [6]. This (collective) motion of the protons seem only to be probed in relativistic Coulomb excitation. It is not well known how this classical view can be related to microscopic properties of the nuclei in a multiphonon state.

Since there is more energy deposit in the nuclei, other decay channels are open for the multiphonon states. Generally, the GRs in heavy nuclei decay by neutron emission. One expects that the double, or triple, GDR decays mainly in the $2n$ and $3n$ decay channel. In fact, such a picture has been adopted in [38,41] with success to explain the total cross sections for the neutron removal in peripheral collisions. The method is the same that we used to explain the one-neutron removal cross sections, i.e., by replacing f_n by f_{2n} , and f_{3n} , in Eq. (152).

Although the perspectives for an experimental evidence of the DGDR via relativistic Coulomb excitation were good, on the basis of the large theoretical cross sections, it was first found in pion scattering at the Los Alamos Pion Facility [53]. In pion scattering off nuclei the DGDR can be described as a two-step mechanism induced by the pion-nucleus interaction. Using the Axel–Brink hypotheses, the cross sections for the excitation of the DGDR with pions were shown to be well within the experimental possibilities [53]. Only about 5 years later, the first Coulomb excitation experiments for the excitation of the DGDR were performed at the GSI facility in Darmstadt/Germany [39,40]. In Fig. 21 we show the result of one of these experiments, which looked for the neutron decay channels of giant resonances excited in relativistic projectiles. The excitation spectrum of relativistic ^{136}Xe projectiles incident on Pb are compared with the spectrum obtained in C targets. A comparison of the two spectra immediately proves that nuclear contribution to the excitation is very small. Another experiment [39] dealt with the photon decay of the double giant resonance. A clear bump in the spectra of coincident photon pairs was observed around the energy of two times the GDR centroid energy in ^{208}Pb targets excited with relativistic ^{209}Bi projectiles.

The advantages of relativistic Coulomb excitation of heavy ions over other probes (pions, nuclear excitation, etc.) was clearly demonstrated in several GSI experiments [39–41,54]. A collection of the experimental data on the energy and width of the DGDR is shown in Fig. 22. The data points are from a compilation from pion (open symbols), and Coulomb excitation and nuclear excitation (full symbols) experiments [8].

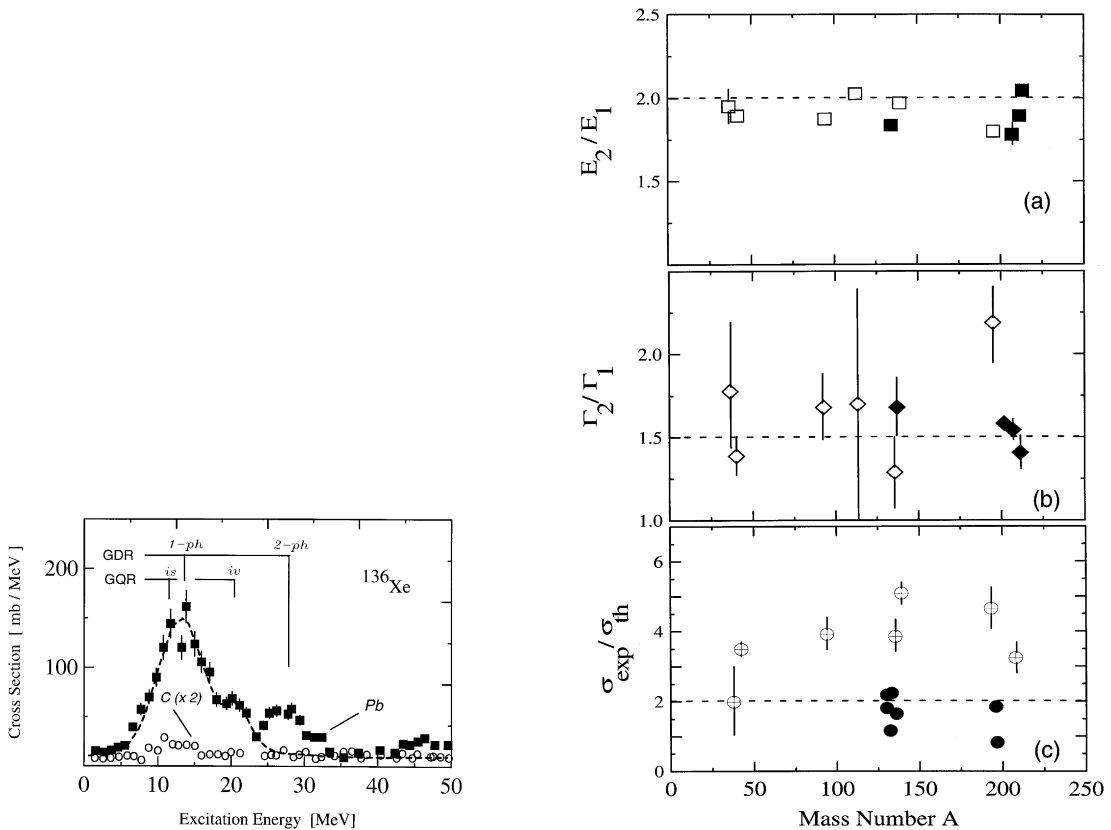


Fig. 21. Experimental results for ^{136}Xe projectile excitation (at 690A MeV) on a Pb target (squares) and a C target (circles). The spectrum for the C target is multiplied by a factor 2 for better presentation. The resonance energies for one- and two-phonon giant resonances are indicated. The dashed curve reflects the results of a first-order calculation for the Pb target. The figure is taken from Ref. [40].

Fig. 22. Compilation of experimental findings with heavy ion (full symbols) and pion induced (open symbols) reactions for the energy, width, and cross sections of the double giant resonance. The data are compared to the energies and widths of the giant dipole resonance, respectively, and to the theoretical values of excitation cross sections.

The dashed lines are guide to the eyes. We see from Fig. 22(a) that the energy of the DGDR agrees reasonably with the expected harmonic prediction that the energy should be about twice the energy of the GDR, although small departures from this prediction are seen, especially in pion and nuclear excitation experiments. The width of the DGDR seems to agree with an average value of $\sqrt{2}$ times that of the GDR, although a factor 2 seems also to be possible, as we see from Fig. 22(b). Fig. 22(c) shows the ratio between the experimentally determined cross sections and the calculated ones. Here is where the data appear to be more dispersed. The largest values of $\sigma_{\text{exp}}/\sigma_{\text{th}}$ come from pion experiments, yielding up to a value of 5 for this quantity.

We now discuss many features of the double GDR excitation theoretically and some attempts to solve the discrepancies between theory and experiment observed in Fig. 22.

3.2. Perturbation theory and harmonic models

3.2.1. Sum rules for single and double resonances

The simplest way to determine the matrix elements of excitation of giant resonances is by means of sum rules under the assumption that those sum rules are exhausted by collective states. We have done this when we used the sum rules (96), (97). Let us look at these with more details, since they will be useful for the determination of the matrix elements for multiphonon excitations. The conventional sum rules for the dipole and quadrupole transitions, derived without exchange and velocity-dependent corrections, are ($\hbar = 1$)

$$\sum_f \omega_{fi} |D_{fi}^{(m)}|^2 = \frac{3}{4\pi} \frac{1}{2m_N} \frac{NZ}{A} e^2, \quad (167)$$

$$\sum_f \omega_{fi} |Q_{fi}^{(m)}|^2 = 2 \frac{1}{2m_N} \frac{3R^2}{4\pi} e^2 \times \begin{cases} Z^2/A, & \text{isoscalar excitations,} \\ NZ/A, & \text{isovector excitations,} \end{cases} \quad (168)$$

where $D^{(m)} \equiv \mathcal{M}(E1m)$ and $Q^{(m)} \equiv \mathcal{M}(E2m)$.

We explain our procedure on the example of the dipole sum rule (167). The right-hand side S_D of (167) being calculated for the fixed initial state $|i\rangle$ in fact does not depend on the choice of $|i\rangle$. (This dependence is rather weak even if the exchange terms are taken into account). Since S_D does not depend on the projection m of the dipole operator $D_1^{(m)}$ as well, it is convenient to introduce in usual way the reduced matrix elements of multipole operators,

$$\langle f; I_f M_f | \mathcal{O}_i^{(m)} | i; I_i M_i \rangle = \langle I_f M_f | I_i l M_i m \rangle \langle f; I_f || \mathcal{O}_i || i; I_i \rangle, \quad (169)$$

where f stands now for all quantum numbers except angular momentum ones, I and M , and to perform the additional summation of Eq. (167) over m . In such a way one obtains

$$\sum_{f, I_f} \omega_{fi} (2I_f + 1) \langle f; I_f || D || i; I_i \rangle^2 = 3(2I_i + 1) S_D. \quad (170)$$

Now let us take the ground state $|0\rangle$ of an even–even nucleus with angular momentum $I_0 = 0$ as an initial one $|i; I_i\rangle$. If we assume that the single GDR $|1\rangle \equiv |1; 1\rangle$ is an isolated state saturating the corresponding sum rule, we just divide the right-hand side of (170) by the excitation energy ω_{10} to obtain the reduced matrix element

$$(1 || D || 0)^2 = S_D / \omega_{10}. \quad (171)$$

In order to be able to calculate the cross section of excitation of the double GDR, we have to take the single GDR state $|1\rangle$ as an initial one. The corresponding sum in Eq. (170), according to our assumption, is saturated by (i) “down” transition to the ground state $|0\rangle$, which has negative transition energy $-\omega_{10}$ and, due to the symmetry properties of the Clebsch–Gordan coefficients, the strength which is 3 times larger than that of Eq. (171), and (ii) “up” transitions to the double GDR states $|2; I_2 = L\rangle$ where L can be equal to 0 and 2. The resulting sum rule for the up transitions is

$$\sum_{L=0,2} (2L + 1) \omega_{21}^{(L)} (2; L || D || 1)^2 = 12 S_D, \quad (172)$$

where $\omega_{21}^{(L)} \equiv E_{2;L} - E_1$ is the energy of the second excitation. Actually, considering, instead of the sum over m , the original dipole sum rule (167) for fixed m , one can separate the two contributions to the sum (172) and find

$$(2; L||D||1)^2 = 2 S_D / \omega_{21}^{(L)}. \quad (173)$$

Obviously, it is consistent with the sum rule (172).

Eqs. (171) and (173) imply the relation between the strengths of sequential excitation processes,

$$(2; L||D||1)^2 = 2(\omega_{10}/\omega_{21}^{(L)})(1||D||0)^2. \quad (174)$$

For the equidistant vibrational spectrum this result is nothing but the standard Bose factor of stimulated radiation; our result is valid under more broad assumptions. The resulting enhancement factor includes, in addition, the ratio of transition frequencies which, according to the data, is slightly larger than 1. The generalization for the third and higher order excitation processes is straightforward.

3.2.2. Spreading widths of single and double resonances

The above assumption of saturation certainly does not account for the fact that the resonances are wide. In fact, this might be also relevant for the calculation of total cross sections since the Coulomb excitation amplitudes given by may vary strongly with the excitation energy. Therefore, they might be sensitive to the shape of the strength function. The widths of the resonances can be taken into account in a simplified approach, as we describe next.

In a microscopic approach, the GDR is described by a coherent superposition of one-particle one-hole states. One of the many such states is pushed up by the residual interaction to the experimentally observed position of the GDR. This state carries practically all the $E1$ strength. This situation is simply realized in a model with a separable residual interaction. We write the GDR state as (one phonon with angular momentum $1M$) $|1, 1M\rangle = A_{1M}^\dagger |0\rangle$ where A_{1M}^\dagger is a proper superposition of particle-hole creation operators. Applying the quasi-boson approximation we can use the boson commutation relations and construct the multiphonon states (N -phonon states). A N -phonon state will be a coherent superposition of N -particle N -hole states. The width of the GDR in heavy nuclei is essentially due to the spreading width, i.e., to the coupling to more complex quasibound configurations. The escape width plays only a minor role. We are not interested in a detailed microscopic description of these states here. We use a simple model for the strength function [15]. We couple a state $|a\rangle$ (i.e. a GDR state) by some mechanism to more complex states $|\alpha\rangle$, for simplicity we assume a constant coupling matrix element $V_{a\alpha} = \langle a|V|\alpha\rangle = \langle \alpha|V|a\rangle = v$. With an equal spacing of D of the levels $|\alpha\rangle$ one obtains a width

$$\Gamma = 2\pi v^2/D, \quad (175)$$

for the state $|\alpha\rangle$. We assume the same mechanism to be responsible for the width of the N -phonon state: one of the N -independent phonons decays into the more complex states $|\alpha\rangle$ while the other $(N - 1)$ -phonons remain spectators. We write the coupling interaction in terms of creation (destruction) operators $c_\alpha^\dagger(c_\alpha)$ of the complex states $|\alpha\rangle$ as

$$V = v(A_{1M}^\dagger c_\alpha + A_{1M} c_\alpha^\dagger). \quad (176)$$

For the coupling matrix elements v_N , which connects an N -phonon state $|N\rangle$ to the state $|N - 1, \alpha\rangle$ ($N - 1$ spectator phonons) one obtains

$$v_N = \langle N - 1, \alpha | V | N \rangle = v \langle N - 1 | A_{1M} | N \rangle = v \sqrt{N} , \quad (177)$$

i.e., one obtains for the width Γ_N of the N -phonon state

$$\Gamma = 2\pi N(v^2/D) = N\Gamma , \quad (178)$$

where Γ is given by Eq. (175).

Thus, the factor N in (178) arises naturally from the bosonic character of the collective states. For the DGDR this would mean $\Gamma_2 = 2\Gamma_1$. The data points shown in Fig. 22(b) seem to favor a lower multiplicative factor.

We will assume that the damping of the collective modes is mostly due to the coupling to the background of complex configurations in the vicinity of the resonance energy. Then the resonance state $|\lambda\rangle$ gets fragmented acquiring the spreading width Γ_λ . The stationary final states $|f\rangle$ in the region of the GR are superpositions (with the same exact quantum numbers as the collective mode) of the form

$$|f\rangle = C_\lambda^{(f)} |\lambda\rangle + \sum_v C_v^{(f)} |v\rangle , \quad (179)$$

where $|\lambda\rangle$ is a pure GR state and $|v\rangle$ are complex many particle-many hole states. If the resonance component dominates in the excitation process as it should be for the one-body multipole operator, we find the first-order amplitude $a_{fi}^{(\lambda)}$ of the excitation of the individual state $|f\rangle$ in the fragmentation region

$$a_{fi}^{(\lambda)} \simeq [C_\lambda^{(f)}]^* a_\lambda^{1st}(\omega_{fi}) . \quad (180)$$

Here a_λ^{1st} stands for the original first-order excitation amplitude. As a function of the transition energy, the probability for the one-phonon excitation is

$$P_\lambda^{1st}(\omega) = \sum_f [|C_\lambda^{(f)}|^2 \delta(\omega - \omega_{fi})] |a_\lambda^{1st}(\omega_{fi})|^2 \equiv \mathcal{F}_\lambda(\omega) |a_\lambda^{1st}(\omega)|^2 , \quad (181)$$

where we introduced the strength function $\mathcal{F}_\lambda(\omega)$.

The traditional derivation of the strength function (see Ref. [55]) is based on the rough assumptions concerning mixing matrix elements and the equidistant spectrum of complex states. The matrix elements $V_{\lambda v}$ which couple the collective mode to the background states are assumed to be of the same average magnitude for all remote states $|v\rangle$ from both sides of the resonance. Under those conditions the resulting strength function has the Breit–Wigner (BW) shape

$$\mathcal{F}_\lambda(\omega) = \frac{1}{2\pi} \frac{\Gamma_\lambda}{(\omega - \omega_\lambda)^2 + \Gamma_\lambda^2/4} , \quad (182)$$

where Γ_λ is the spreading width of the collective resonance,

$$\Gamma_\lambda = 2\pi \langle V_{\lambda v}^2 \rangle_v / d , \quad (183)$$

d is the mean level spacing of complex states, coupling matrix elements are averaged over the states $|v\rangle$ and ω_λ is the energy centroid. We will use in our numerical calculations the BW strength function (182) with the empirical parameters ω_λ and Γ_λ . However, the same procedure can be applied to any specific form of $\mathcal{F}_\lambda(\omega)$. Later we come back to the question of justification of the model leading to Eqs. (182) and (183).

The multiphonon states could also be reached by a direct excitation. Quite similarly, we can repeat the above arguments to calculate the probability for the direct excitation of a multiphonon state, with the appropriate spreading width and energy centroid of that state. The direct (or first-order) probabilities are then given by

$$P_2^{1\text{st}}(\omega) = \mathcal{F}_2(\omega) |a_2^{1\text{st}}(\omega)|^2. \quad (184)$$

Let us now treat the case of the two-step excitation of GR (double-phonon). For simplicity, we denote the single-phonon state by $|1\rangle$ and the double-phonon state by $|2\rangle$, the corresponding centroids being at ω_1 and ω_2 , respectively. The total probability to excite the double-phonon state is obtained by

$$P(\omega) = \sum_f |a_{f_i}^{1\text{st}} + a_{f_i}^{2\text{nd}}|^2 \delta(\omega - \omega_{f_i}) \equiv P^{1\text{st}}(\omega) + P^{2\text{nd}}(\omega) + P^{\text{int}}(\omega), \quad (185)$$

where $P^{1\text{st}}$ is the direct (or first-order) excitation of the double-phonon state, $P^{2\text{nd}}$ is the two-step (or second-order) excitation term, and the last term in Eq. (185) is the interference between the two.

3.2.3. Second-order perturbation theory

To second-order, the amplitude for a two-step excitation to a state $|2\rangle$ via intermediate states $|1\rangle$ is given by

$$a_{20}^{2\text{nd}} = \sum_1 \frac{1}{(i\hbar)^2} \int_{-\infty}^{\infty} dt e^{i\omega_{21}t} V_{21}(t) \int_{-\infty}^t dt' e^{i\omega_{10}t'} V_{10}(t'), \quad (186)$$

where $V_{21}(t)$ is a short notation for the interaction potential inside brackets of the integral of Eq. (186) for the transition $|1\rangle \rightarrow |2\rangle$.

Using the integral representation of the step function

$$\Theta(t - t') = - \lim_{\delta \rightarrow 0^+} \frac{1}{2\pi i} \int_{-\infty}^{\infty} \frac{e^{-iq(t-t')}}{q + i\delta} dq = \begin{cases} 1 & \text{if } t > t', \\ 0 & \text{if } t < t', \end{cases} \quad (187)$$

one finds [16]

$$a_{20}^{2\text{nd}} = \frac{1}{2} \sum_1 a_{21}^{1\text{st}}(\omega_{21}) a_{10}^{1\text{st}}(\omega_{10}) + \frac{i}{2\pi} \sum_1 \mathcal{P} \int_{-\infty}^{\infty} \frac{dq}{q} a_{21}^{1\text{st}}(\omega_{21} - q) a_{10}^{1\text{st}}(\omega_{10} + q), \quad (188)$$

where \mathcal{P} stands for the principal value of the integral. For numerical evaluation it is more appropriate to rewrite the principal value integral in Eq. (188) as

$$\begin{aligned} & \mathcal{P} \int_{-\infty}^{\infty} \frac{dq}{q} a_{21}^{1\text{st}}(\omega_{21} - q) a_{10}^{1\text{st}}(\omega_{10} + q) \\ &= \int_0^{\infty} \frac{dq}{q} [a_{21}^{1\text{st}}(\omega_{21} - q) a_{10}^{1\text{st}}(\omega_{10} + q) - a_{21}^{1\text{st}}(\omega_{21} + q) a_{10}^{1\text{st}}(\omega_{10} - q)]. \end{aligned} \quad (189)$$

To calculate $a^{1\text{st}}(\omega)$ for negative values of ω , we note that the interaction potential can be written as a sum of an even and an odd part. This implies that $a^{1\text{st}}(-\omega) = -[a^{1\text{st}}(\omega)]^*$. For three-phonon excitation we use the third term of the time-dependent perturbation expansion, and the same procedure as above (Eqs. (187)–(189)).

3.2.4. Harmonic vibrator model

A simplified model, often used in connection with multiphonon excitations, is the harmonic vibrator model. In this model, the resonance widths are neglected and the Coupled-Channel equations can be solved exactly, in terms of the first-order excitation amplitudes [15]. The excitation amplitude of the n th harmonic oscillator state, for any time t , is given by

$$a_{\text{h.o.}}^{(n)}(t) = ([a_{1\text{st}}(t)]^n / \sqrt{n!}) \exp\{-|a_{1\text{st}}(t)|^2/2\}, \quad (190)$$

where $a_{1\text{st}}(t)$ is the excitation amplitude for the 0 (g.s.) $\rightarrow 1$ (one phonon) calculated with the first-order perturbation theory.

For the excitation of giant resonances, n can be identified with the state corresponding to a multiple n of the single giant resonance state. This procedure has been often used in order to calculate the cross sections for the excitation of multiphonon giant resonances. Since this result is exact in the harmonic vibrator model, it accounts for all coupling between the states. However, this result can be applied to studies of giant resonance excitation only if the same class of multipole states is involved. I.e., if one considers only electric dipole excitations, and use the harmonic oscillator model, one can calculate the excitation probabilities, and cross sections, of the GDR, double-GDR, triple-GDR, etc. Eq. (190) is not valid if the excitation of other multipolarities are involved, e.g., if the excitation of dipole states and quadrupole states are treated simultaneously. In Ref. [50] a hybrid harmonic oscillator model has been used. In this work, it is assumed that the difference between the amplitudes obtained with the harmonic oscillator model and with n th order perturbation theory is due to the appearance of the exponential term on the r.h.s. of Eq. (190). This exponential takes care of the decrease in the occupation amplitude of the ground state as a function of time. As argued in Ref. [50], the presence of other multipole states, e.g., of quadrupole states, together with dipole states, may be accounted for by adding the first-order excitation amplitudes for the quadrupole states to the exponent in Eq. (190). This would correct for the flux from the ground state to the quadrupole states. In other words, Eq. (190) should be corrected to read

$$a_{\text{h.o.}}^{(n)}(\pi\lambda, t) = ([a_{1\text{st}}(\pi\lambda, t)]^n / \sqrt{n!}) \exp\left\{-\sum_{\pi'\lambda'} |a_{1\text{st}}(\pi'\lambda', t)|^2/2\right\}. \quad (191)$$

The harmonic oscillator model is not in complete agreement with the experimental findings. The double-GDR and -GQR states do not have exactly twice the energy of the respective GDR and GQR states [7–9]. Apparently, the matrix elements for the transition from the GDR (GQR) to the double-GDR (double-GQR) state does not follow the boson rule [42]. This is borne out by the discrepancy between the experimental cross sections for the excitation of the double-GDR and the -GQR with the perturbation theory, and with the harmonic oscillator model [7–9]. Thus, a Coupled-Channels calculation is useful to determine which matrix elements for the transitions among the giant resonance states reproduce the experimental data [121].

Assuming that one has $\sigma_7^{\pi\lambda}(E)$ somehow (either from experiments, or from theory), a simple harmonic model following the discussion above can be formulated to include the widths of the states. As we have mentioned, in the harmonic oscillator model the inclusion of the coupling between all multiphonon states can be performed analytically [15]. One of the basic changes is that the excitation probabilities calculated to first-order, $P_{\pi\lambda}^{1st}(E, b)$, are modified to include the flux of probability to the other states. That is,

$$P_{\pi\lambda}(E, b) = P_{\pi\lambda}^{1st}(E, b) \exp\{-P_{\pi\lambda}^{1st}(b)\}, \quad (192)$$

where $P_{\pi\lambda}^{1st}(b)$ is the integral of over the excitation energy E . In general, the probability to reach a multiphonon state with the energy $E^{(n)}$ from the ground state, with energy $E^{(0)}$, is obtained by an integral over all intermediate energies

$$P_{\pi\lambda}^{(n)}(E^{(n)}, b) = \frac{1}{n!} \exp\{-P_{\pi\lambda}^{1st}(b)\} \int dE^{(n-1)} dE^{(n-2)} \dots dE^{(1)} \\ \times P_{\pi\lambda}^{1st}(E^{(n)} - E^{(n-1)}, b) P_{\pi\lambda}^{1st}(E^{(n-1)} - E^{(n-2)}, b) \dots P_{\pi\lambda}^{1st}(E^{(1)} - E^{(0)}, b). \quad (193)$$

3.2.5. Comparison with experiments

The reactions $^{136}\text{Xe} + ^{208}\text{Pb}$ at 0.69A GeV and $^{209}\text{Bi} + ^{208}\text{Pb}$ at 1A GeV have been measured at GSI [39,40]. We apply the formalism developed in the preceding sections to calculate the excitation probabilities and cross sections for these systems.

Cross sections (in mb) for the Coulomb excitation of the GDR_{iv} , GQR_{is} and GQR_{iv} in ^{136}Xe incident on Pb at 0.69A GeV are given in Table 3. We have assumed that the GDR_{iv} , GQR_{is} and the GQR_{iv} are located at 15.3, 12.3 and 24 MeV, and that they exhaust 100%, 70% and 80% of the corresponding sum rules, respectively [56]. We used $b_{\min} = 1.2(A_1^{1/3} + A_2^{1/3}) \text{ fm} = 13.3 \text{ fm}$ as a lower limit guess and $b_{\min} = 15.6 \text{ fm}$ suggested by the parameterization [44] as an upper limit (number inside parentheses). The parameterization [43] yields an intermediate value for this quantity. The contributions to various angular momentum projections of each state are shown separately. In the last column the total cross sections are calculated with the widths of the states taken into account. We use for the GDR_{iv} , GQR_{is} and GQR_{iv} the BW strength functions (182) with the resonance widths $\Gamma = 4.8, 4$ and 7 MeV , respectively [56]. We see that states with higher angular momentum projections are more populated. The inclusion of the widths of the resonances

Table 3

Cross sections (in mb) for the Coulomb excitation of the GDR_{iv} , GQR_{is} and GQR_{iv} in ^{136}Xe incident on ^{208}Pb at 0.69A GeV. The cross sections in the last column are calculated with the widths of the states taken into account. The values outside (inside) parentheses use $b_{\min} = 13.3$ (15.6) fm

| | $m = \pm 2$ | $m = \pm 1$ | $m = 0$ | σ_{total} | σ_{width} |
|-------------------|-------------|-------------|-------------|-------------------------|-------------------------|
| GDR_{iv} | — | 949 (712) | 264 (201) | 2162 (1630) | 2482 (1820) |
| GQR_{is} | 90 (64) | 8.4 (6.09) | 14.3 (10.6) | 211 (150) | 241 (169) |
| GQR_{iv} | 29.7 (25.6) | 6.1 (5.46) | 14 (12.4) | 84.1 (74.5) | 102 (93) |

in the calculation increases the cross sections by about 10–20%. The experimental value [40] 1110 ± 80 mb for the GDR is much smaller which made the authors of [40] to claim that the GDR absorbs only 65% of the sum rule (this number apparently contradicts to the systematics of data for real monochromatic photons [56]). Using this value, our result reduces to 1613 (1183) mb which seems to prefer the upper value of b_{\min} . The numbers in parentheses are also in rough agreement with the data [40] for the GQR_{is} and GQR_{iv} .

Using the formalism developed in Section 2.8 we have also calculated the cross sections for the nuclear excitation of the GQR_{is} in the same reaction. The cross sections for the excitation of isovector modes are reduced by a factor $[(N - Z)/A]^2$ since the isovector mode is excited due to the difference in strength of the nuclear interaction between the target and the protons and neutrons of the projectile [55]. This implies that the isovector excitations are strongly suppressed in nuclear excitations. Therefore, we do not consider them here. For the excitation of the GQR_{is} we find $\sigma^N = 5.3$ mb, if we use the deformation parameter $\beta R = 0.7$ fm for ^{136}Xe . In the calculation of the nuclear potential we used Fermi density distributions with parameters $\rho_0 = 0.17 \text{ fm}^{-3}$ and $R = 5.6$ (6.5) fm, $a = 0.65$ (0.65) fm for Xe (Pb). The nucleon–nucleon cross section used was 40 mb. Again we see that the nuclear contribution to the total cross section is very small.

The double dipole phonon state can couple to total angular momentum 0 or 2. For the state with $L = 2$ there is the possibility of a direct quadrupole Coulomb excitation ($L = 0$ states cannot be Coulomb excited [6]). For simplicity, we do not consider here the physics of the isospin coupling of the two GDR.

We calculated the direct and the two-step probabilities for the excitation of the double-phonon state according to the approach discussed in the previous sections. The total cross sections obtained are shown in Table 4. We found that the principal value term in Eq. (188) contributes very little (less than 1%) to the $GDR \times GDR$ cross section via a two-step process.

From Table 5 we see that the inclusion of the widths of the final ($GDR \times GDR$) and the intermediate (GDR) state increase the cross sections by 10–20%. For the position and width of the $GDR \times GDR$ state we took $E = 28.3$ MeV and $\Gamma = 7$ MeV, respectively [40] which corresponds to $\omega_{10} = 15.3$ MeV and $\omega_{21} = 13$ MeV, both for $L = 2$ and $L = 0$. For the calculation of the direct excitation we assumed that the resonance would exhaust 20% of the GQR_{is} sum rule. It is based on the hypotheses that the missing strength of the low-lying GQR_{is} could be located at the double dipole phonon state as a consequence of the anharmonic phonon coupling of the (QDD)-type. Obviously, it should be considered as highly overestimated upper boundary of the direct excitation.

Table 4

Excitation cross sections (in mb) of the GDR_{iv} , and of the $[GDR]^n$ states in the reaction $^{208}\text{Pb} + ^{208}\text{Pb}$ at 640A MeV. A comparison with first-order perturbation theory and the harmonic oscillator is made

| State | 1st pert. th. | Harm. osc. | c.c. |
|----------------|---------------|------------|------|
| GDR_{iv} | 3891 | 3235 | 3210 |
| $[GDR_{iv}]^2$ | 388 | 281 | 280 |
| $[GDR_{iv}]^3$ | 39.2 | 27.3 | 32.7 |
| $[GDR_{iv}]^4$ | 4.2 | 2.4 | 3.2 |

Table 5

Cross sections (in mb) for the Coulomb excitation of the double GDR in ^{136}Xe incident on Pb at 0.69A GeV. The cross sections in the last column are calculated with the widths of the states taken into account. The values outside (inside) parentheses use $b_{\min} = 13.3$ (15.6) fm

| DGDR state | $m = \pm 2$ | $m = \pm 1$ | $m = 0$ | σ_{total} | σ_{width} |
|----------------------------|-------------|-------------|-------------|-------------------------|-------------------------|
| L = 0 (two-step) | — | — | 22.8 (10.7) | 22.8 (10.7) | 28.4 (13.3) |
| L = 2 (two-step) | 23.3 (11.2) | 13.4 (6.6) | 51.4 (26.8) | 124.8 (62.4) | 154 (77) |
| L = 2 (direct – 20% of SR) | 3.27 (2.85) | 0.86 (0.77) | 2.12 (1.88) | 10.3 (9.12) | 11.8 (10.8) |

In Ref. [57] the reduced transition probability for the excitation of double-phonon states within the quasiparticle-phonon model have been calculated. The value $B(2^+, E2) = 4.2e^2\text{fm}^4$ has been obtained. Using this value we get that the cross section for the direct excitation of the $L = 2$ state is $12\ \mu\text{b}$, much smaller than what we quote above. We conclude that even in the more optimistic cases the contribution of the direct mechanism to the total cross section for Coulomb excitation of the double-phonon state is much less than that of the two-step process.

Another conclusion drawn from the numbers of Table 5 is that the excitation of the $L = 2$ double-phonon state is much stronger than for the $L = 0$ state. Adding the two contributions we find that the total cross section for the excitation of the double-phonon state (excluding the direct mechanism) in the reaction above is equal to 182 (101) mb. The experimental value of Ref. [40] is about 215 ± 50 mb. As stated above, the nuclear contribution to the (direct) excitation of the double-phonon state is not relevant. If we assume again that about 20% of the sum rule strength is exhausted by this state (using e.g. $\beta R = 0.1$ fm), we get 1.1 mb for the nuclear excitation of the $L = 2$ double-phonon state. Contrary to the single phonon case, the appropriate value of b_{\min} for the double GDR experiment [40] is $b_{\min} = 13.3$ fm.

We also compare our results with the experiment of Ritman et al. [39]. They measured the excitation of a ^{208}Pb target by means of ^{209}Bi projectiles at 1A GeV and obtained 770 ± 220 mb for the excitation cross section of the double resonance. We calculate the cross sections for the same system, using $E_1 = 13.5$ MeV, $\Gamma_1 = 4$ MeV, $E_2 = 27$ MeV and $\Gamma_2 = 6$ MeV for the energy position and widths of the GDR and the GDR \times GDR in ^{208}Pb , respectively. Using the formalism developed in Sections 3.2.2 and 3.2.3 and including the effects of the widths of the states, we find $\sigma_1 = 5234$ b for the excitation of the GDR and $\sigma_2 = 692$ mb for the excitation of the GDR \times GDR, using $b_{\min} = 1.2(A_p^{1/3} + A_T^{1/3})\text{fm} = 14.2$ fm. Thus, while the cross section for the excitation of single phonons is a factor 2.8 larger than that of the experiment of Ref. [40], the cross sections for the excitation of double phonons is larger by a factor 3.8. This is due to the larger value for the excitation probabilities caused by a larger $B(E1)$ value for this reaction. The parameterization [44] with $b_{\min} = b_{\text{min}} = 16.97$ fm would lead to smaller cross sections $\sigma_1 = 4130$ mb and $\sigma_2 = 319$ mb.

We found the ratio of $(P_{m=+1} + P_{m=-1})/P_{m=0} = 9.4$ for the excitation of the GDR in the experiment of Ref. [39]. They quote the value 28 in their calculations and fit the gamma-ray angular distribution according to this value. We think that this result could somewhat change the extracted value of the GDR \times GDR cross section which is quoted in Ref. [39].

Using the formalism shown in Section 3.2.4 we find that the cross sections for the excitation of three-phonon states in the experiment of Schmidt et al. [40] is equal to 19.2 mb (with $b_{\min} = 13.3$ fm) while it is equal to 117 mb (with $b_{\min} = 14.2$ fm) for the experiment of Ritman et al. [39]. The identification of these resonances is therefore more difficult, but possible with the present experimental techniques. Using the same arguments leading to Eq. (174) we find for the reduced matrix elements, in obvious notations, $|D_{32}|^2 = 3(\omega_{10}/\omega_{32})|D_{10}|^2$, which we used in our calculation. We assumed that $\omega_{10}/\omega_{32} \simeq \omega_{10}/\omega_{21}$. These enhancement factors for the excitation of higher phonon states are very important to explain the magnitude of the cross sections. The anharmonic effects, suggested in [40] to explain the large excitation of double GDR, are expected to be small since the mixing of single- and double-phonon states is forbidden by the angular momentum and parity. The main anharmonic effect, apart from the weak coupling of the double GDR with $L = 2$ to GQR, is the IBM-like scattering of dipole phonons which splits $L = 0$ and $L = 2$ states but hardly changes excitation and decay properties.

Another important question is related to the expected width of the multiphonon states. Early estimates [15] presented in Section 3.2.2 indicated that these widths should scale as $\Gamma_n = n\Gamma_1$. The experiments show however that a scaling as $\Gamma_n = \sqrt{n}\Gamma_1$ is more appropriate, at least for the double GDR. We next address in detail different aspects of physics responsible for the width of the double-phonon state.

3.3. General arguments on the width of the double-phonon state

Here we discuss in qualitative terms the problem of the width of a collective state which can be thought of as being created by the excitation of two quanta in a complex many-body system. We assume that the genuine decay to continuum is of minor importance at the given excitation energy. Therefore, we focus on the damping width which comes from the fact that the collective mode is a specific coherent superposition of simple configurations (for instance, of a particle-hole character) rather than a pure stationary state.

In the actual excitation process the predominant mechanism is that of the sequential one-phonon excitation. Under our assumption that the sum rule is saturated by the GR the intermediate states contribute to this process as far as they contain a significant collective component. Therefore the interference of many incoherent paths can be neglected so that we are interested in the shape $P(E)$ of the excitation function at a given energy $E = E_1 + E_2$ which can be obtained as a convolution of the single-phonon excitation functions,

$$P(E) = \int dE_1 dE_2 P_1(E_1)P_2(E_2)\delta(E - E_1 - E_2). \quad (194)$$

The same shape should be revealed in the deexcitation process.

In this formulation the problem is different from what is usually looked at when one is interested, for example, in sound attenuation. In such classical problems the conventional exponential decrease of the wave intensity does not correspond to the decay of the state with a certain initial number of quanta. Contrary to that, here we have to compare the damping rates of individual quantum states with the fixed number of quanta, single- and double-phonon states in particular.

We have to mention also that in the nuclear GR case quantum effects are more pronounced since the temperature corresponding to the relevant excitation energy is less than $\hbar\omega$, whereas in the measurements of the attenuation of the zero and first sound in the macroscopic Fermi liquid [58] the situation is always inverse and the quantum limit is hardly attainable. (In nuclear physics the classical case can be studied with low-lying quadrupole vibrations.)

Independently of specific features of nuclear structure (level density, A -dependence, shell effects, finiteness of the system leading to the linear momentum nonconservation and, therefore, to the estimate of the available phase space which could be different from that for infinite matter, and so on) we can try to make several comments of general nature.

If the anharmonic effects could be considered to be small we can assume that the phonons decay independently by what can be described, using the language of stationary quantum mechanics, as mixing to complex background states. The decay rate $\Gamma_1(e)$ of an individual quasiparticle (elementary excitation) with energy e depends on the background level density and, whence, on the excitation energy. The decay of a state with n quasiparticles occurs as far as one of the constituents decays. It implies the simple estimate of the width Γ_n of the n -quantum state, $\Gamma_n \simeq n\Gamma_1(E/n)$. For the decay of typical many particle-many hole configurations [59–61] one usually takes the Fermi-liquid estimate $\Gamma_1(e) \propto e^2$ which leads to $\Gamma_n \propto T^3 \propto E^{3/2}$ since the average number of quasiparticles in a typical thermal configuration at temperature T is $n \propto T$. This estimate agrees with data. In the case of the pure n -phonon state $E/n = \hbar\omega$ which results in the ratio $r_n \equiv \Gamma_n/\Gamma_1 \simeq n$.

Thus, the simplest line of reasoning favors the width of the double GR to be twice as big as the width of the single GR. At the first glance, this estimate is especially reasonable for the giant dipole since here the anharmonic effects, determining the whole pattern of low-lying vibrations, are expected to be very weak. Angular momentum and parity conservation forbids cubic anharmonicity which would mix single- and double-quantum states and influence both excitation cross sections and spreading widths. The main anharmonic term, apart from mentioned in Section 3.2.2 weak mixing of the giant quadrupole to the double dipole state with $L = 2$, probably corresponds to the phonon scattering similar to that in the IBM. It results in the shift of the double-phonon state from $2\hbar\omega$ and splitting of $L = 0$ and $L = 2$ states hardly changing the decay properties. Experimentally, the energy shift seems to be rather small.

There are also other arguments for the width ratio $r_2 = 2$. In our calculation of cross sections we assumed the BW shape (182) of strength functions (181). If the sequential excitation is described by the BW functions $P_1(E_1)$ with the centroid at e and the width Γ , and $P_2(E_2)$ with corresponding parameters e' and Γ' , the convolution (194) restores the BW shape with the centroid at $e + e'$ and the total width $\Gamma + \Gamma'$. For identical phonons it means that the width ratio $r_2 = 2$.

As we mentioned in Section 3.2.2, the BW shape of the strength function is derived analytically within the simple model [55] of coupling between a phonon and complex background states. One diagonalizes first the Hamiltonian in the subspace of those complex states and get their energies ε_ν . If the underlying dynamics is nearly chaotic, the resulting spectrum will show up level repulsion and rigid structure similar to that of the Gaussian Orthogonal Ensemble (GOE), with the mean level spacing d . Roughly speaking, one can assume the equidistant energy spectrum. The collective phonon $|1\rangle$ at energy E_1 is coupled to those states and corresponding matrix elements $V_{1\nu}$ are assumed to be of the same order of magnitude (much larger than the level spacing d) for all states $|\nu\rangle$ in the large energy interval around the collective resonance. Then the energies of the stationary

states (final states $|f\rangle$ in the notations of previous sections) are the roots $E = E_f$ of the secular equation

$$F(E) \equiv E - E_1 - \sum_v \frac{V_{1v}^2}{E - \varepsilon_v} = 0, \quad (195)$$

and the distribution of the collective strength, Eq. (179),

$$|C_1^{(f)}|^2 = [dF/dE]_{E=E_f}^{-1} = \left[1 + \sum_v \frac{V_{1v}^2}{(E_f - \varepsilon_v)^2} \right]^{-1} \quad (196)$$

reveals the BW shape (182) and the “golden rule” expression (183) for the width Γ_1 .

We can repeat the procedure for the double phonon state. Phonons of different kind would couple to different background states with different level spacing and coupling matrix elements. It corresponds to independent decay leading as we discussed above to $\Gamma_2 = \Gamma + \Gamma'$. For the identical phonons, we should take into account that the double phonon state $|2\rangle$ is coupled to the states “single phonon + background” and the background states here are the same as those determining the width of the single phonon state $|1\rangle$. This picture is in accordance with the famous Axel–Brink hypotheses. Therefore, the expression for the width, Eq. (183), contains the same level density whereas all coupling matrix elements for the transition to a complex state $|v\rangle$ (plus a remaining phonon) have to be multiplied by the Bose factor, $V_{2v} = \sqrt{2}V_{1v}$. Thus, we come again to $r_2 = 2$.

The approach of the preceding paragraph can be slightly modified by introducing explicitly coupling via a doorway state [62] or GOE internal dynamics [63]. In both cases the Bose factor $\sqrt{2}$ leads to the same result $r_2 = 2$.

In addition, the collective resonance might be further broadened by the coupling to low-lying collective vibrational or rotational modes. For example, in the simplest model where the dipole phonon radiates and absorbs low-energy scalar quanta, it is easy to show that, in the stationary cloud of scalar quanta, their average number, which determines the fragmentation region of the dipole mode, is proportional to the squared number of dipole phonons. Hence it gives a large width ratio $r_2 = 4$. For the nuclei where actual data exist, this is not important since they are rather rigid spherical nuclei with no adiabatic collective modes.

On the other hand, one can present some arguments in favor of the width ratio $r_2 = \sqrt{2}$ which apparently is preferred by the existing data.

First of all, this value follows from the convolution (194) of Gaussian distribution functions (instead of BW ones). Of course, this is the inconsistent approach since the experimentalists use BW or Lorentzian fit. But one can easily understand that the result $r_2 = \sqrt{2}$ is not restricted to Gaussian fit. For an arbitrary sequence of two excitation processes we have $\langle E \rangle = \langle E_1 + E_2 \rangle$ and $\langle E^2 \rangle = \langle (E_1 + E_2)^2 \rangle$; for uncorrelated steps it results in the addition of fluctuations in quadrature $(\Delta E)^2 = (\Delta E_1)^2 + (\Delta E_2)^2$. Identifying these fluctuations with the widths up to a common factor, we get for the identical phonons $\Gamma_2^2 = 2\Gamma_1^2$, or $r_2 = \sqrt{2}$.

The same conclusion will be valid for any distribution function which, as the Gaussian one, has a finite second moment, contrary to the BW or Lorentzian ones with the second moment diverging. In some sense we may conclude that, in physical terms, the difference between $r_2 = 2$ and $r_2 = \sqrt{2}$

is due to the different treatment of the wings of the distribution functions which reflect small admixtures of far remote states.

In the standard model of the strength function [55] all remote states are coupled to the collective mode equally strong. This is obviously an unrealistic assumption. The shell model (more generally, mean field) basis is the “natural” one [64] for estimating a degree of complexity of various states in a Fermi system at not very high excitation energy. In this representation matrix elements of residual interaction couple the collective state (coherent superposition of particle–hole excitations found for example in the framework of the RPA) only to the states of the next level of complexity (exciton class). Those states, in turn, become mixed with more complex configurations. This process proliferates and each simple state acquires its spreading, or fragmentation, width $2a = Nd$ where N stands for a typical number of stationary states carrying the noticeable weight of the ancestor state and the level spacing d is basically the same as in the mean field approximation. Inversely, N can be viewed as the localization length of a stationary complex state in the mean field basis.

In the stochastic limit the local background dynamical properties can be modeled by those of the GOE with the semicircle radius a . This intrinsic spreading width a , which is expected to be of the order of magnitude of typical matrix elements of the original residual interaction between simple configurations, is the dynamical scale missed in the standard model which corresponds to the limit $a \rightarrow \infty$. The existence of this intrinsic scale can be associated with the saturation [65] of the width of a single GR at high temperature.

The standard model supposedly is valid for the spreading width Γ small in comparison with a . Because of the relatively weak interaction leading to the isospin impurity, this is the case for the isobaric analog states (IAS) [66,67] where typical spreading widths are less than 100 keV. This approach allows one to explain, at least qualitatively, small variations of the spreading widths of the IAS. The tunneling mixing of superdeformed states with the normal deformed background presents an extreme example of the small spreading width. However, in the case of GR the situation might be different.

To illustrate the new behavior in the opposite case of $\Gamma \geq a$, we can imagine the limit of the almost degenerate intrinsic states with very strong coupling to a collective mode. (The actual situation presumably is intermediate.) Assuming that the unperturbed phonon state has an energy in the same region, one can easily see from Eqs. (195) and (196) that the coupling results in the appearance of the two collective states sharing evenly the collective strength and shifted symmetrically from the unperturbed region by $\Delta E = \pm \sqrt{\sum_v V_v^2}$. The physical reason is evident: the interaction of the background states through the collective mode creates a specific coherent superposition which is hybridized with and repelled from the original collective state. The similar effect was discussed in different context in [68] and observed in numerical simulations [69]. The well-known doubling of the resonance peak at the passage of a laser beam through a cavity containing a two-level atom is the simplest prototype of such a phenomenon.

In this limit one gets the effective width of collective response $2\Delta E = 2\sqrt{N\langle V_v^2 \rangle} = 2\sqrt{a\Gamma_s/\pi}$ where Γ_s is the standard spreading width (183). This effective width is linearly proportional to the average coupling matrix element. Therefore it should increase by factor \sqrt{n} when applied to a n -phonon collective state. Thus, we anticipate in this limit $r_2 = \sqrt{2}$. One may say that the phonons do not decay independently being correlated via common decay channels. In the literature the similar result, due to apparently the same physical reasons, was mentioned in [70] referring to the unpublished calculations in the framework of the second RPA.

3.4. Coupled-channel calculations with inclusion of the GR widths

We have seen that the excitation probabilities of excitation of single- and double-giant resonances are quite large. It is worthwhile to study the excitation process with a coupled channels calculation and compare to the other approximations. We will now study this effect by using the Coupled-Channels Born approximation. This approximation was used in Ref. [71] to describe the excitation of the double-giant resonance in relativistic heavy ion collisions. It is based on the idea that in such cases only the coupling between the ground state and the dominant giant dipole state has to be treated exactly. The reason is that the transitions to giant quadrupole and to the double-phonon states have low probability amplitudes, even for small impact parameters. However, an exact treatment of the back-and-forth transitions between the ground state and the giant dipole state is necessary. This leads to modifications of the transitions amplitudes to the remaining resonances, which are populated by the ground state and the GDR. In Ref. [71] the application of the method was limited to the use of an schematic interaction, and the magnetic substates were neglected. These deficiencies are corrected here. The method allows the inclusion of the width of the giant resonances in a very simple and straightforward way. It will be useful for us to compare with the coupled-channels calculations with isolated states, as we described in the previous sections. Fig. 23 represents the procedure. The GDR is coupled to the ground state while the remaining resonances are fed by these two states according to first-order perturbation theory. The coupling matrix elements involve the ground state and a set of doorway states $|\mathcal{D}_{\lambda\mu}^{(n)}\rangle$, where n specifies the kind of resonance and $\lambda\mu$ are angular momentum quantum numbers. The amplitudes of these resonances in real continuum states are

$$\alpha^{(n)}(\varepsilon) = \langle \phi(\varepsilon) | \mathcal{D}_{\lambda\mu}^{(n)} \rangle, \quad (197)$$

where $\phi(\varepsilon)$ denotes the wave function of one of the numerous states which are responsible for the broad structure of the resonance. In this equation $\varepsilon = E_x - E_n$, where E_x is the excitation energy and E_n is the centroid of the resonance considered.

As we have stated above, in this approach we use the coupled-channels equations for the coupling between the ground state and the GDR. This results in the following coupled-channels equations:

$$\begin{aligned} i\hbar \dot{a}_0(t) &= \sum_{\mu} \int d\varepsilon \langle \phi(\varepsilon) | \mathcal{D}_{1\mu}^{(1)} \rangle \langle \mathcal{D}_{1\mu}^{(1)} | V_{E_1, \mu}(t) | 0 \rangle \exp\left\{ -\frac{i}{\hbar}(E_1 + \varepsilon)t \right\} a_{\varepsilon, 1\mu}^{(1)}(t) \\ &= \sum_{\mu} \int d\varepsilon \alpha^{(1)}(\varepsilon) V_{\mu}^{(01)}(t) \exp\left\{ -\frac{i}{\hbar}(E_1 + \varepsilon)t \right\} a_{\varepsilon, 1\mu}^{(1)}(t) \end{aligned} \quad (198)$$

and

$$i\hbar \dot{a}_{\varepsilon, 1\mu}^{(1)}(t) = [(\alpha^{(1)}(\varepsilon) V_{\mu}^{(01)}(t))^* \exp\{i(E_1 + \varepsilon)t/\hbar\} a_0(t)]. \quad (199)$$

Above, $n = 1$ stands for the GDR, a_0 denotes the occupation amplitude of the ground state and $a_{\varepsilon, 1\mu}^{(1)}$ the occupation amplitude of a state located at an energy ε away from the GDR centroid, and with magnetic quantum number μ ($\mu = -1, 0, 1$). We used the short-hand notation $V_{\mu}^{(01)}(t) = \langle \mathcal{D}_{1\mu}^{(1)} | V_{E_1, \mu}(t) | 0 \rangle$.

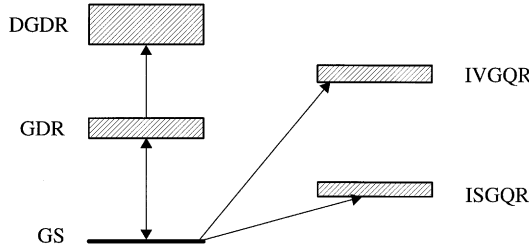


Fig. 23. Schematic representation of the excitation of giant resonances, populated in heavy ion collisions.

Integrating Eq. (199) and inserting the result in Eq. (198), we get the integro-differential equation for the ground state occupation amplitude

$$\ddot{a}_0(t) = -\frac{1}{\hbar^2} \sum_{\mu} V_{\mu}^{(01)}(t) \int d\varepsilon |\alpha^{(1)}(\varepsilon)|^2 \int_{-\infty}^t dt' [V_{\mu}^{(01)}(t')]^* \exp\{-i(E_1 + \varepsilon)(t - t')/\hbar\} a_0(t'), \quad (200)$$

where we used that $a_{\varepsilon,1\mu}^{(1)}(t = -\infty) = 0$. To carry out the integration over ε , we should use an appropriate parametrization for the doorway amplitude $\alpha^{(1)}(\varepsilon)$. A convenient choice is the Breit–Wigner (BW) form

$$|\alpha^{(1)}(\varepsilon)|^2 = \frac{1}{2\pi} \left[\frac{\Gamma_1}{\varepsilon^2 + \Gamma_1^2/4} \right], \quad (201)$$

where Γ_1 is chosen to fit the experimental width. In this case, this integral will be the simple exponential

$$\int d\varepsilon |\alpha^{(1)}(\varepsilon)|^2 \exp\left\{-i\frac{(E_1 + \varepsilon)t}{\hbar}\right\} = \exp\left\{-i\frac{(E_1 - i\Gamma_1/2)t}{\hbar}\right\}. \quad (202)$$

A better agreement with the experimental line shapes of the giant resonances is obtained by using a Lorentzian (L) parametrization for $|\alpha^{(1)}(\varepsilon)|^2$, i.e.,

$$|\alpha^{(1)}(\varepsilon)|^2 = \frac{2}{\pi} \left[\frac{\Gamma_1 E_x^2}{(E_x^2 - E_1^2)^2 + \Gamma_1^2 E_x^2} \right], \quad (203)$$

where $E_x = E_1 + \varepsilon$. The energy integral can still be performed exactly [72] but now it leads to the more complicated result

$$\int d\varepsilon |\alpha^{(1)}(\varepsilon)|^2 \exp\left\{-i\frac{(E_1 + \varepsilon)t}{\hbar}\right\} = \left(1 - i\frac{\Gamma_1}{2E_1}\right) \exp\left\{-i\frac{(E_1 - i\Gamma_1/2)t}{\hbar}\right\} + \Delta C(t), \quad (204)$$

where $\Delta C(t)$ is a non-exponential correction to the decay. For the energies and widths involved in the excitation of giant resonances, this correction can be shown numerically to be negligible. It will therefore be ignored in our subsequent calculations. After integration over ε , Eq. (200) reduces to

$$\ddot{a}_0(t) = -\mathcal{S}_1 \sum_{\mu} V_{\mu}^{(01)}(t) \int_{-\infty}^t dt' [V_{\mu}^{(01)}(t')]^* \exp\left\{-i\frac{(E_1 - i\Gamma_1/2)(t - t')}{\hbar}\right\} a_0(t'), \quad (205)$$

where the factor \mathcal{S}_1 is $\mathcal{S}_1 = 1$ for BW-shape and $\mathcal{S}_1 = 1 - i\Gamma_1/2E_1$ for L-shape.

We can take advantage of the exponential time dependence in the integral of the above equation, to reduce it to a set of second-order differential equations. Introducing the auxiliary amplitudes $A_\mu(t)$, given by the relation

$$a_0(t) = 1 + \sum_{\mu} A_\mu(t), \quad (206)$$

with initial conditions $A_\mu(t = -\infty) = 0$, and taking the derivative of Eq. (205), we get

$$\ddot{A}_\mu(t) - \left[\frac{\dot{V}_\mu^{(01)}(t)}{V_\mu^{(01)}(t)} - \frac{i}{\hbar} \left(E_1 - i\frac{\Gamma_1}{2} \right) \right] \dot{A}_\mu(t) + \mathcal{S}_1 \frac{|V_\mu^{(01)}(t)|^2}{\hbar^2} \left[1 + \sum_{\mu'} A_{\mu'}(t) \right] = 0. \quad (207)$$

Solving the above equation, we get $a_0(t)$. Using this amplitude and integrating Eq. (199), one can evaluate $a_{e,1\mu}^{(1)}(t)$. The probability density for the population of a GDR continuum state with energy E_x in a collision with impact parameter b , $P_1(b, E_x)$, is obtained through the summation over the asymptotic ($t \rightarrow \infty$) contribution from each magnetic substate. We get

$$P_1(b, E_x) = |\alpha^{(1)}(E_x - E_1)|^2 \sum_{\mu} \left| \int_{-\infty}^{\infty} dt' \exp\{iE_x t'\} [V_\mu^{(01)}(t')]^* a_0(t') \right|^2, \quad (208)$$

where $|\alpha^{(1)}(E_x - E_1)|^2$ is given by Eq. (201) or by Eq. (203), depending on the choice of the resonance shape.

To first order, DGDR continuum states can be populated through $E2$ -coupling from the ground state or through $E1$ -coupling from GDR states. The probability density arising from the former is given by Eq. (208), with the replacement of the line shape $|\alpha^{(1)}|^2$ by its DGDR counterpart $|\alpha^{(2)}|^2$ (defined in terms of parameters E_2 and Γ_2) and the use of the appropriate coupling-matrix elements $V_\mu^{(02)}(t)$ with the $E2$ time dependence given by (29). On the other hand, the contribution from the latter process is

$$P_2(b, E_x) = |\alpha^{(2)}(E_x - E_2)|^2 \mathcal{S}_1 \sum_{\nu} \left| \int_{-\infty}^{\infty} dt' \exp\{iE_x t'\} \sum_{\mu} (V_{\nu\mu}^{(12)}(t'))^* \right. \\ \left. \times \int_{-\infty}^{t'} dt'' (V_\mu^{(01)}(t'')) \exp\left\{ -i \frac{(E_1 - i\Gamma_1/2)(t - t'')}{\hbar} \right\} a_0(t'') \right|^2. \quad (209)$$

We should point out that Eq. (209) is *not* equivalent to second-order perturbation theory. This would be true only in the limit $a_0(t) \rightarrow 1$. In this approach, $a_0(t) \neq 1$, since it is modified by the time-dependent coupling to the GDR state. This coupling is treated exactly by means of the Coupled-Channels equations. We consider that this is the main effect on the calculation of the DGDR excitation probability. This approach is justified due to the small excitation amplitude for the transition $1 \rightarrow 2$, since $a_1(t) \ll a_0(t)$.

Equations similar to (208) can also be used to calculate the GQR_{is} and GQR_{iv} excitation probabilities, with the proper choice of energies, widths, and transition potentials (e.g., $V_{E2}(t)$, or $V_{N2}(t)$, or both).

In the next section we will apply the results of this section to analyze the effect of the widths of the GRs in a Coupled-Channels approach to relativistic Coulomb excitation.

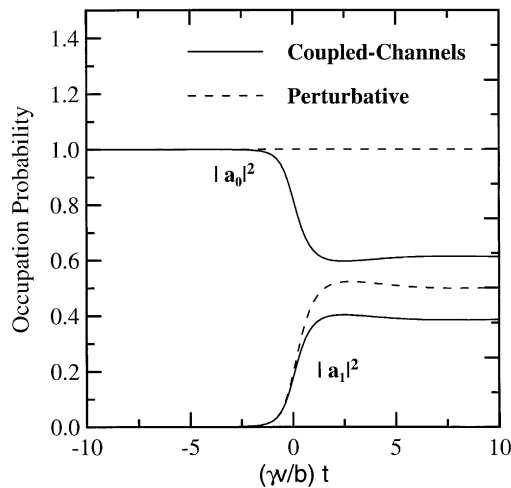


Fig. 24. Time dependence of the occupation probabilities $|a_0|^2$ and $|a_1|^2$, in a collision with impact parameter $b = 15$ fm. The time is measured in terms of the dimensionless variable $\tau = (\gamma v/b) t$. The system is ^{208}Pb (640A MeV) + ^{208}Pb .

3.4.1. Zero-width calculations

We consider the excitation of giant resonances in ^{208}Pb projectiles, incident on ^{208}Pb targets at 640A MeV, which has been studied at the GSI/SIS, Darmstadt [7,9]. For this system the excitation probabilities of the isovector giant dipole (GDR_{iv}) at 13.5 MeV are large and, consequently, high-order effects of channel coupling should be relevant. To assess the importance of these effects, we assume that the GDR state depletes 100% of the energy-weighted sum-rule and neglect the resonance width.

As a first step, we study the time evolution of the excitation process, solving the Coupled-Channels equations for a reduced set of states. We consider only the ground state (g.s.) and the GDR. The excitation probability is then compared with that obtained with first-order perturbation theory. This is done in Fig. 24, where we plot the occupation probabilities of the g.s., $|a_0(t)|^2$, and of the GDR, $|a_1(t)|^2$, as functions of time, for a collision with impact parameter $b = 15$ fm. As discussed earlier, the Coulomb interaction is strongly peaked around $t = 0$, with a width of the order $\Delta t \simeq b/\gamma v$. Accordingly, the amplitudes are rapidly varying in this time range. A comparison between the CC-calculation (solid line) and first-order perturbation theory (dashed line) shows that the high-order processes contained in the former lead to an appreciable reduction of the GDR excitation probability. From this figure we can also conclude that our numerical calculations can be restricted to the interval $-10 < \tau < 10$, where $\tau = (\gamma v/b) t$ is the time variable measured in natural units. Outside this range, the amplitudes reach asymptotic values.

It is worthwhile to compare the predictions of first-order perturbation theory with those of the harmonic oscillator model and the CC calculations. In addition to the GDR, we include the following multiphonon states: a double-giant dipole state ($[\text{GDR}_{iv}]^2$) at 27 MeV, a triple-giant dipole state ($[\text{GDR}_{iv}]^3$) at 40.5 MeV, and a quadruple giant dipole state ($[\text{GDR}_{iv}]^4$) at 54 MeV. The

coupling between the multiphonon states are determined by boson factors, i.e., for $0 \rightarrow 1$ and $n - 1 \rightarrow n$ [42]:

$$|\langle n - 1 || V_{E/N,1} || n \rangle|^2 = n |\langle 0 || V_{E/N,1} || 1 \rangle|^2 . \quad (210)$$

Direct excitations of the multiphonon states from the g.s. are not considered. The angular momentum addition rules for bosons yields the following angular momentum states: $L = 0$ and 2, for the $[\text{GDR}]^2$ state; $L = 1, 2$, and 3, for the $[\text{GDR}]^3$ state; and $L = 0, 1, 2, 3$, and 4, for the $[\text{GDR}]^4$ state. We assume that states with the same number of phonons are degenerate. In Table 5, we show the resulting cross sections. The excitation probabilities and the cross section were calculated with the formalism of Section 3.4. The integration over impact parameter was carried out in the interval $b_{\min} < b < \infty$. As we discuss below, the low- b cut-off value [42] $b_{\min} = 14.3$ fm mocks up absorption effects. We have checked that the CC results are not significantly affected by the unknown phases of the transition matrix elements. Since the multiphonon spectrum is equally spaced, and the coupling matrix elements are related through boson factors (as in Eq. (210)), the harmonic oscillator and the CC cross sections should be equal. In fact the numerical results of these calculations given in the table are very close. We also see that the excitation cross sections of triple- and quartic-phonon states are much smaller than that for the $[\text{GDR}]^2$. Therefore, we shall concentrate our studies on the $[\text{GDR}]^2$, neglecting other multiphonon states.

Next, we include the remaining important giant resonances in ^{208}Pb . Namely, the isoscalar giant quadrupole (GQR_{is}) at 10.9 MeV and the isovector giant quadrupole (GDR_{iv}) at 22 MeV. Also in this case, we use 100% of the energy-weighted sum rules to deduce the strength matrix elements. In Table 6, we show the excitation probabilities in a grazing collision, with $b = 14.3$ fm. We see that first-order perturbation theory yields a very large excitation probability for the GDR_{iv} state. This is strongly reduced in a c.c. calculation, as we have already discussed in connection with Fig. 24. The excitations of the remaining states are also influenced. They are reduced due to the lowering of the occupation probabilities of the g.s. and of the GDR_{iv} state in the c.c. calculation. As expected, perturbation theory and c.c. calculations agree at large impact parameters, when the transition probabilities are small. For the excitation of the $[\text{GDR}_{\text{iv}}]^2$ state we used second-order perturbation theory to obtain the value in the second column. The presence of the GQR_{is} and the GQR_{iv} influence the c.c. probabilities for the excitation of the GDR and the $[\text{GDR}_{\text{iv}}]^2$, respectively.

Table 6

Transition probabilities at $b = 14.3$ fm, for the reaction $^{208}\text{Pb} + ^{208}\text{Pb}$ at 640A MeV. A comparison with first order perturbation theory is made

| Trans. | 1st pert. th. | c.c. |
|---|---------------|-------|
| g.s. \rightarrow g.s. | — | 0.515 |
| g.s. \rightarrow GDR_{iv} | 0.506 | 0.279 |
| g.s. \rightarrow GQR_{is} | 0.080 | 0.064 |
| g.s. \rightarrow GQR_{iv} | 0.064 | 0.049 |
| g.s. \rightarrow $[\text{GDR}_{\text{iv}}]^2$ | 0.128 | 0.092 |

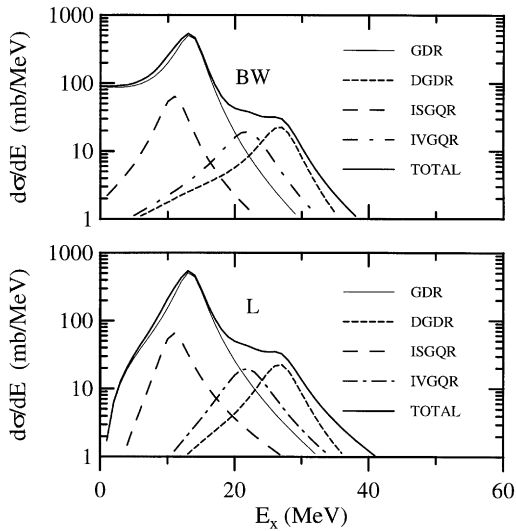


Fig. 25. Excitation energy spectra of the main giant resonances for both Breit–Wigner and Lorentzian line shapes. The system is ^{208}Pb (640A MeV) + ^{208}Pb .

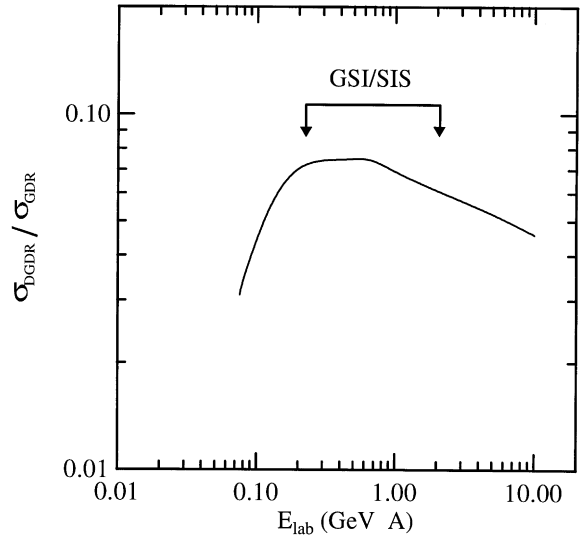


Fig. 26. Ratio between the DGDR and the GDR cross sections in $^{208}\text{Pb} + ^{208}\text{Pb}$ collisions, as a function of the bombarding energy.

Table 7

Centroid energies and widths of the main giant resonances in ^{208}Pb

| | GDR | DGDR | GQR _{is} | GQR _{iv} |
|----------------|------|------|-------------------|-------------------|
| E (MeV) | 13.5 | 27.0 | 10.9 | 20.2 |
| Γ (MeV) | 4.0 | 5.7 | 4.8 | 5.5 |

3.4.2. Effect of resonance widths

We now turn to the influence of the giant resonance widths on the excitation dynamics. We had considered this in Section 3.2. But, now we show that the coupled-channels effects lead to important quantitative modifications of the results. We use the CCBA formalism developed in Section 3.4. Schematically, the CC problem is that represented Fig. 23. As we have seen above, the strongest coupling occurs between the g.s. and the GDR.

In Fig. 25, we show the excitation energy spectrum for the GDR, the DGDR (a notation for the $[\text{GDR}_{iv}]^2$), GQR_{is} and GQR_{iv}. The centroid energies and the widths of these resonances are listed in Table 7. The figure shows excitation spectra obtained with both Breit-Wigner (BW) and Lorentzian (L) line shapes. One observes that the BW and L spectra have similar strengths at the resonance maxima. However, the low-energy parts (one or two widths below the centroid) of the spectra are more than one order of magnitude higher in the BW calculation. The reason for this behavior is that Coulomb excitation favors low energy transitions and the BW has a larger low

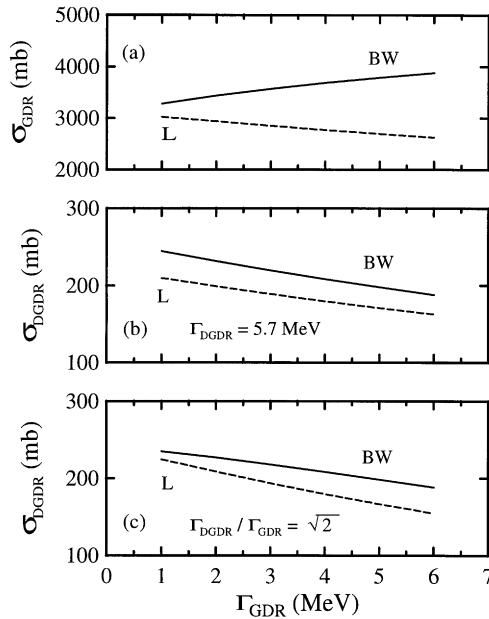


Fig. 27. Dependence of σ_{GDR} and σ_{DGDR} on the GDR width, treated as a free parameter. For details see the text. The system is ^{208}Pb (640A MeV) + ^{208}Pb .

energy tail as compared with the Lorentzian line shape. The contribution from the DGDR leads to a pronounced bump in the total energy spectrum. This bump depends on the relative strength of the DGDR with respect to the GDR. In Fig. 26, we show the ratio $\sigma_{\text{DGDR}}/\sigma_{\text{GDR}}$ as a function of the bombarding energy. We observe that this ratio is roughly constant in the energy range $E_{\text{lab}}/A = 200\text{--}1000 \text{ MeV}$ and it falls beyond these limits. This range corresponds to the SIS-energies at the GSI-Darmstadt facility.

We now study the influence of the resonance widths and shapes on the GDR and DGDR cross sections. This study is similar to that presented in Ref. [71], except that we now have a realistic three-dimensional treatment of the states and consider different line shapes. In the upper part of Fig. 27, denoted by (a), we show σ_{GDR} as a function of Γ_{GDR} , treated as a free parameter. We note that the BW and L parameterizations lead to different trends. In the BW case the cross section grows with Γ_{GDR} while in the L case it decreases. The growing trend is also found in Ref. [71], which uses the BW line shape. The reason for this trend in the BW case is that an increase in the GDR width enhances the low energy tail of the line shape, picking up more contributions from the low energy transitions, favored in Coulomb excitation. On the other hand, an increase of the GDR width enhances the doorway amplitude to higher energies where Coulomb excitation is weaker. In Fig. 27(b) and (c), we study the dependence of σ_{GDR} on Γ_{GDR} . In (b), the DGDR width is kept fixed at the value 5.7 MeV while in (c) it is kept proportional to σ_{GDR} , fixing the ratio $\Gamma_{\text{DGDR}}/\Gamma_{\text{GDR}} = \sqrt{2}$. The first point to be noticed is that the BW results are systematically higher than the L ones. This is a consequence of the different low-energy tails of these functions, as discussed above. One notices also that σ_{DGDR} decreases with Γ_{GDR} both in the BW and L cases. This trend can be understood in

Table 8

Cross sections (in mb) for the excitation of giant resonances in lead, for the reaction $^{208}\text{Pb} + ^{208}\text{Pb}$ at 640A MeV. See text for details

| GDR | DGDR | GQR _{is} | GQR _{iv} |
|------|-----------------|-------------------|-------------------|
| 2704 | 184 (199) [198] | 347 | 186 |

terms of the uncertainty principle. If the GDR width is increased, its lifetime is reduced. Since the DGDR is dominantly populated from the GDR, its short lifetime leads to decay before the transition to the DGDR.

To assess the sensitivity of the DGDR cross section on the strength of the matrix elements and on the energy position of the resonance, we present in Table 8 the cross sections for the excitation of the GDR, DGDR, GQR_{is} and GQR_{iv}, obtained with the CCBA approximation and 100% of the sum-rules for the respective modes. In this calculation we have included the strong absorption, as explained in Section 2.7. For comparison, the values inside parenthesis (and brackets) of the DGDR excitation cross section include a direct excitation of the $L = 2$ DGDR state. We assumed that 20% of the $E2$ sum rule could be allocated for this excitation mode of the DGDR. The cross sections increase by less than 10% in this case. The value inside parentheses (brackets) assume a positive (negative) sign of the matrix element for the direct excitation.

Since the excitation of the DGDR is weak, it is very well described by Eq. (209) and the DGDR population is approximately proportional to the squared strength of $V^{(12)}$. Therefore, to increase the DGDR cross section by a factor of 2, it is necessary to violate the relation $E_{\text{DGDR}} = 2E_{\text{GDR}}$ by the same factor. This would require a strongly anharmonic Hamiltonian for the nuclear collective modes, which would not be supported by traditional nuclear models [42]. Arguments supporting such anharmonicities have recently been presented in Refs. [73–75]. Another effect arising from anharmonicity would be the spin or isospin splitting of the DGDR. Since the Coulomb interaction favors lower energy excitations, it is clear that a decrease of the DGDR centroid would increase its cross section. A similar effect would occur if a strongly populated substate is splitted to lower energies. To study this point, we have varied the energy of the DGDR centroid in the range $20 \text{ MeV} \leq E_{\text{DGDR}} \leq 27 \text{ MeV}$. The obtained DGDR cross sections (including direct excitations) are equal to 620 mb, 299 mb and 199 mb, for the centroid energies of 20, 24 and 27 MeV, respectively. Although the experimental data on the DGDR excitation [7–9] seem to indicate that $E_{\text{DGDR}} \sim 2E_{\text{GDR}}$, a small deviation (in the range of 10–15%) of the centroid energy from this value might be possible. However, the data are not conclusive, and more experiments are clearly necessary. We conclude, that from the arguments analyzed here, the magnitude of the DGDR cross section is more sensitive to the energy position of this state. The magnitude of the DGDR cross section would increase by a factor 2 if the energy position of the DGDR decreases by 20%, as found in Refs. [73–75], due to anharmonic effects. In Ref. [19] one obtained $\sigma_{\text{DGDR}} = 620, 299$ and 199 mb for the centroid energies of $E_{\text{DGDR}} = 20, 24$ and 27 MeV, respectively. This shows that anharmonic effects can play a big role in the Coulomb excitation cross sections of the DGDR, depending on the size of the shift of E_{DGDR} . However, in Ref. [42] the source for anharmonic effects were discussed and it was suggested that it should be very small, i.e., $\Delta^{(2)}E = E_{\text{DGDR}} - 2E_{\text{GDR}} \simeq 0$.

The anharmonic behavior of the giant resonances as a possibility to explain the increase of the Coulomb excitation cross sections has been studied by several authors (see also Ref. [76], and references therein). It was found that the effect is indeed negligible and it could be estimated [76] as $\Delta^{(2)}E < E_{\text{GDR}}/(50.A) \sim A^{-4/3} \text{ MeV}$.

One attempt to explain the larger experimental cross section is to include contributions from excitation of a single coherent phonon on “hot” fine structure states (Brink–Axel mechanism). Recently [77,78] this has been done through two different approaches. In the first one [77], the nucleus is described as a collective harmonic oscillator interacting with a set of oscillators representing statistical degrees of freedom. In the second [78], a statistical approach along the lines proposed by Ko [79] (see also [15]) is used. These works indicate that the Brink–Axel mechanism should play an important role, being able to explain, in part, some discrepancies between theory and experimental cross sections. Further work along these lines were published by, Hussein and collaborators [80–82]. In a recent publication [83], the influence of the isospin structure of the double-giant resonance was studied in detail. It was shown that this structure also leads to an enhancement of the calculated cross sections.

The calculations discussed so far are based on macroscopic properties of the nuclei, sum rules, etc. Now we show that, in order to obtain a better quantitative description of double-giant resonances it is necessary to include the internal degrees of freedom of the nuclei appropriately. We will discuss this next. But, we first describe the formalism that we will use for this purpose.

4. Description of one- and multi-phonon excited states within the quasiparticle-phonon model

4.1. The model Hamiltonian and phonons

The Hamiltonian, H , of the quasiparticle-phonon model (QPM) (see Refs. [84–86] for more details) is introduced on the basis of physical ideas of nucleons moving in an average field and interacted among each other by means of a residual interaction. Schematically it can be written in the form

$$H = H_{\text{s.p.}} + H_{\text{pair}} + H_{\text{r.i.}} \quad (211)$$

We limit ourselves here only by the formalism for even–even spherical nuclei. The first term of Eq. (211), $H_{\text{s.p.}}$, corresponds to the average field for neutrons (n) and protons (p). In the second-quantized representation it can be written in terms of creation (annihilation) a_{jm}^+ (a_{jm}) operators of particles on the level of the average field with quantum numbers $j \equiv [n, l, j]$ and m as follows:

$$H_{\text{s.p.}} = \sum_{\tau} \sum_{j,m}^{n,p} E_j a_{jm}^+ a_{jm} \quad (212)$$

where E_j is the energy of the single-particle level degenerated in spherical nuclei by magnetic quantum number m . The second term of Eq. (211), H_{pair} , corresponds to residual interaction responsible for pairing in non-magic nuclei. In the QPM this interaction is described by monopole pairing with a constant matrix element $G_{\tau}^{(0)}$

$$H_{\text{pair}} = \sum_{\tau}^{n,p} G_{\tau}^{(0)} \sum_{j,j'} \sqrt{(2j+1)(2j'+1)} [a_{jm}^+ a_{j'-m}^+]_{00} [a_{j'-m} a_{jm}]_{00} \quad (213)$$

$$[a_j^+ a_{j'}^+]_{\lambda\mu} = \sum_{m,m'} C_{jmj'm'}^{\lambda\mu} a_{jm}^+ a_{j'm'}^+, \quad (214)$$

where $C_{jmj'm'}^{\lambda\mu}$ is the Clebsch–Gordan coefficient. Since the QPM is usually applied for a description of properties of medium and heavy nuclei with a filling of different subshells for neutrons and protons, the neutron–proton monopole pairing is neglected. The residual interaction, $H_{r.i.}$, is taken in the QPM in a separable form as a multipole decomposition. Its part in the particle–hole channel can be written as

$$H_{r.i.}^{(p-h)} = \sum_{\lambda\mu} \sum_{\tau\rho}^{\pm 1} (\kappa_0^{(\lambda)} + \rho\kappa_1^{(\lambda)}) M_{\lambda\mu}^+(\tau) M_{\lambda\mu}(\rho\tau), \quad (215)$$

where $\kappa_0^{(\lambda)}$ are the model parameters which determine the strength of isoscalar (isovector) residual interaction. The multipole operator $M_{\lambda\mu}^+(\tau)$ has the form

$$M_{\lambda\mu}^+(\tau) = \sum_{j,m,j',m'} \langle jm | i^\tau f_\lambda^\tau(r) Y_{\lambda\mu}(\Omega) | j'm' \rangle a_{jm}^+ a_{j'm'} \quad (216)$$

for the natural parity states and the form

$$M_{\lambda\mu}^+(\tau) = \sum_{j,m,j',m',l_{m_1}} \langle jm | i^\tau f_l^\tau(r) [\boldsymbol{\sigma} \cdot \mathbf{Y}_{lm_1}(\Omega)]_{\lambda\mu} | j'm' \rangle a_{jm}^+ a_{j'm'} \quad (217)$$

for the unnatural parity states. The function $f_\lambda^\tau(r)$ is a radial formfactor which in actual calculations is taken either as r^λ or as a derivative of the central part of the average field: $f_\lambda^\tau(r) = dU^\tau(r)/dr$. The value $\tau = -1(+1)$ corresponds to neutrons (protons). We will not consider here the residual interaction in the particle–particle channel which is the most important for the description of two-nucleon transfer reactions.

The basic QPM equations are obtained by means of step-by-step diagonalization of the model Hamiltonian (211). In the first step its first two terms (212) and (213) are diagonalized. For that the Bogoliubov’s canonical transformation from particle creation (annihilation) operators to quasiparticle creation (annihilation) operators α_{jm}^+ (α_{jm}) is applied:

$$a_{jm}^+ = u_j \alpha_{jm}^+ + (-1)^{j-m} v_j \alpha_{j-m}. \quad (218)$$

The ground state of even–even nucleus, $|\rangle_q$, is assumed as a quasiparticle vacuum: $\alpha_{jm} |\rangle_q \equiv 0$. Then the energy of the ground state is minimized:

$$\delta \left\langle \left\langle H_{s.p.} + H_{\text{pair}} \right\rangle_q + \sum_j \mu_j (u_j^2 + v_j^2 - 1) \right\rangle = 0, \quad (219)$$

where μ_j are Lagrange coefficients. The result of this minimization are the well-known BCS equations solving which one obtains correlation functions $C_\tau = G_\tau^{(0)} \sum_j \mu_j v_j$ and chemical potentials λ_τ for neutron and proton systems. The coefficients of the Bogoliubov transformation u_j and v_j can be calculated from these values as follows:

$$v_j^2 = \frac{1}{2} \left\{ 1 - \frac{E_j - \lambda_\tau}{\varepsilon_j} \right\}, \quad u_j^2 = 1 - v_j^2, \quad (220)$$

where ε_j is the quasiparticle energy:

$$\varepsilon_j = \sqrt{C_\tau^2 + [E_j - \lambda_\tau]^2} . \quad (221)$$

In magic nuclei the BCS equations yield a zero value for the correlation function and the position of the chemical potential in the gap between particles and hole is uncertain. This results in vanishing of monopole pairing correlations and the Bogoliubov's coefficients $u_j(v_j)$ equal to 0(1) for holes and to 1(0) for particles, respectively.

After diagonalization of the first two terms of the model Hamiltonian (211) they can be written as:

$$H_{\text{s.p.}} + H_{\text{pair}} = \sum_{\tau} \sum_{j,m}^{n,p} \varepsilon_j \alpha_{jm}^+ \alpha_{jm} \quad (222)$$

and the multiple operator (216) in terms of quasiparticle operators has the form

$$M_{\lambda\mu}^+(\tau) = \sum_{jj'}^{\tau} \frac{f_{jj'}^{(\lambda)}}{\sqrt{2\lambda+1}} \left\{ \frac{u_{jj'}^{(+)}}{2} ([\alpha_j^+ \alpha_{j'}^+]_{\lambda\mu} + (-1)^{\lambda-\mu} [\alpha_{j'} \alpha_j]_{\lambda-\mu}) - v_{jj'}^{(-)} B_{\tau}(jj'; \lambda\mu) \right\}, \quad (223)$$

$$B_{\tau}(jj'; \lambda\mu) = \sum_{mm'} (-1)^{j'+m'} C_{jmj'm'}^{\lambda\mu} \alpha_{jm}^+ \alpha_{j'-m'} \quad (224)$$

where $f_{jj'}^{(\lambda)} = \langle j || i^\lambda f_{\lambda}^{\tau}(r) Y_{\lambda}(\Omega) || j' \rangle$ is the reduced matrix element of the multipole operator. We also introduced the following combinations of the Bogoliubov's coefficients: $u_{jj'}^{(\pm)} = u_j v_{j'} \pm u_{j'} v_j$ and $v_{jj'}^{(\mp)} = u_j u_{j'} \mp v_j v_{j'}$ to be used below.

We have determined the ground state of even-even nuclei as the quasiparticle vacuum. In this case, the simplest excited states of nucleus are two-quasiparticle states, $\alpha_{jm}^+ \alpha_{j'm'}^+ | \rangle_q$, which correspond to particle-hole transitions if monopole pairing vanishes. Two fermion quasiparticle operators couple to the total integer angular momentum corresponding to the Bose statistics. Thus, it is convenient to project the bi-fermion terms $[\alpha_j^+ \alpha_{j'}^+]_{\lambda\mu}$ and $[\alpha_{j'} \alpha_j]_{\lambda-\mu}$ in Eq. (223) into the space of quasi-boson operators. Following this boson mapping procedure, we introduce the phonon operators of the multipolarity λ and projection μ as

$$Q_{\lambda\mu}^+ = \frac{1}{2} \sum_{\tau} \sum_{jj'}^{n,p} \{ \psi_{jj'}^{\lambda i} [\alpha_j^+ \alpha_{j'}^+]_{\lambda\mu} - (-1)^{\lambda-\mu} \varphi_{jj'}^{\lambda i} [\alpha_{j'} \alpha_j]_{\lambda-\mu} \} . \quad (225)$$

The total number of different phonons for the given multipolarity λ should be equal to the sum of neutron and proton two-quasiparticle states coupled to the same angular momentum. The index i is used to number these different phonons.

One obtains the coefficients $\psi_{jj'}^{\lambda i}$ and $\varphi_{jj'}^{\lambda i}$ of the linear transformation (225) by diagonalization of the model Hamiltonian in the space of one-phonon states, $Q_{\lambda\mu}^+ | \rangle_{ph}$. This can be done for example by applying again the variation procedure

$$\delta \left\{ \langle | Q_{\lambda\mu} H Q_{\lambda\mu}^+ | \rangle_{ph} - (\omega_{\lambda i} / 2) \left[\sum_{jj'} \{ (\psi_{jj'}^{\lambda i})^2 - (\varphi_{jj'}^{\lambda i})^2 \} - 2 \right] \right\} = 0 . \quad (226)$$

It yields the well-known equations of the random-phase approximation (RPA) which for the case of the separable form of the residual interaction in ph -channel may be written as

$$\left\| \begin{pmatrix} (\kappa_0^{(\lambda)} + \kappa_1^{(\lambda)})X_n^\lambda(\omega) - 1 & (\kappa_0^{(\lambda)} - \kappa_1^{(\lambda)})X_n^\lambda(\omega) \\ (\kappa_0^{(\lambda)} - \kappa_1^{(\lambda)})X_p^\lambda(\omega) & (\kappa_0^{(\lambda)} + \kappa_1^{(\lambda)})X_p^\lambda(\omega) - 1 \end{pmatrix} \right\| = 0, \quad (227)$$

where the following notation have been used:

$$X_\tau^\lambda(\omega) = \frac{1}{2\lambda + 1} \sum_{jj'}^\tau \frac{(f_{jj'}^\lambda u_{jj'}^{(+)})^2 (\varepsilon_j + \varepsilon_{j'})}{(\varepsilon_j + \varepsilon_{j'})^2 - \omega^2}. \quad (228)$$

The determinant equation (227) is a function of the nucleus excitation energy ω . Solving this equation for each multipolarity λ^π , one obtains the spectrum of nuclei one-phonon excitation $\omega_{\lambda i}$. The index i in the definition of the phonon operator (225) gets the meaning of the order number of the solution of Eq. (227). The fermion structure of phonon excitation, i.e. the amplitudes ψ and φ , corresponding to the contribution of different two-quasiparticle components to the phonon operator, are obtained from the following equation:

$$\begin{pmatrix} \psi \\ \varphi \end{pmatrix}_{jj'}^{\lambda i}(\tau) = \frac{1}{\sqrt{2\mathcal{Y}_\tau^{\lambda i}}} \frac{f_{jj'}^\lambda(\tau) u_{jj'}^{(+)}}{\varepsilon_j + \varepsilon_{j'} \mp \omega_{\lambda i}}, \quad (229)$$

where the value $\mathcal{Y}_\tau^{\lambda i}$ is determined from normalization condition for phonon operators:

$$\langle |Q_{\lambda\mu i} Q_{\lambda\mu i}^+| \rangle_{ph} = \sum_\tau^{n,p} \sum_{jj'} \{ (\psi_{jj'}^{\lambda i})^2 - (\varphi_{jj'}^{\lambda i})^2 \} = 2 \quad (230)$$

and one obtains

$$\begin{aligned} \mathcal{Y}_\tau^{\lambda i} &= Y_\tau^{\lambda i} + Y_{-\tau}^{\lambda i} \left\{ \frac{1 - (\kappa_0^{(\lambda)} + \kappa_1^{(\lambda)})X_\tau^\lambda(\omega_{\lambda i})}{(\kappa_0^{(\lambda)} - \kappa_1^{(\lambda)})X_{-\tau}^\lambda(\omega_{\lambda i})} \right\}^2, \\ Y_\tau^{\lambda i} &= \frac{1}{2\lambda + 1} \sum_{jj'}^\tau \frac{(f_{jj'}^\lambda u_{jj'}^{(+)})^2 (\varepsilon_j + \varepsilon_{j'}) \omega_{\lambda i}}{[(\varepsilon_j + \varepsilon_{j'})^2 - \omega^2]^2}. \end{aligned} \quad (231)$$

Equations (227), (229) and (231) correspond to natural parity phonons. Similar equations are valid for unnatural parity phonons by substituting the reduced spin-multipole matrix element $f_{jj'}^{[\sigma] \lambda}$ and combination of coefficients of Bogoliubov transformation $u_{jj'}^{(-)}$ for $f_{jj'}^\lambda$ and $u_{jj'}^{(+)}$, respectively. Also, amplitude $\varphi_{jj'}^{\lambda i}$ changes the sign in Eq. (229) for unnatural parity phonons.

The RPA equations have been obtained under the assumption that the nucleus ground state is the phonon vacuum, $Q_{\lambda\mu i} | \rangle_{ph} \equiv 0$. This means that the ground-state correlations due to the last term of the model Hamiltonian, $H_{r,i}$, are taken into account. If they are not accounted for and the ground state is still considered as a quasiparticle vacuum $| \rangle_q$, one obtains the so-called Tamm–Dankov approximation (TDA). The TDA equations can be easily obtained from the RPA ones by neglecting backward going amplitudes in the definition of the phonon operator (225), i.e. applying $\varphi_{jj'}^{\lambda i} \equiv 0$.

Table 9
Parameters of Woods–Saxon potential, Eq. (233), for different A-mass regions

| A | Neutrons | | | | Protons | | | |
|-----|------------------|-----------------|-----------------|---------------------|------------------|-----------------|-----------------|---------------------|
| | V_0^n (MeV) | R_0^n (fm) | a_0^n (fm) | V_{ls}^n (MeV) | V_0^p (MeV) | R_0^p (fm) | a_0^p (fm) | V_{ls}^p (MeV) |
| 49 | – 41.35 | 4.852 | 0.6200 | – 9.655 | – 58.65 | 4.538 | 0.6301 | – 9.506 |
| 59 | – 46.20 | 5.100 | 0.6200 | – 9.540 | – 53.70 | 4.827 | 0.6301 | – 8.270 |
| 91 | – 44.70 | 5.802 | 0.6200 | – 9.231 | – 56.86 | 5.577 | 0.6301 | – 9.609 |
| 121 | – 43.20 | 6.331 | 0.6200 | – 8.921 | – 59.90 | 6.133 | 0.6301 | – 10.363 |
| 141 | – 45.95 | 6.610 | 0.6200 | – 9.489 | – 57.70 | 6.454 | 0.6301 | – 10.069 |
| 209 | – 44.83 | 7.477 | 0.6301 | – 8.428 | – 60.30 | 7.359 | 0.6301 | – 11.186 |

The relation between the wave functions of the phonon and quasiparticle vacuums is the following [84]:

$$|\rangle_{ph} = \frac{1}{\mathcal{N}} \prod_{\lambda} \exp \left\{ -\frac{1}{4} \sum_{j_1 j_2} \sum_{j_3 j_4} (\psi_{j_3 j_4}^{\lambda i})^{-1} \varphi_{j_1 j_2}^{\lambda i} (-1)^{\lambda - \mu} [\alpha_{j_1}^+ \alpha_{j_2}^+]_{\lambda \mu} [\alpha_{j_3}^+ \alpha_{j_4}^+]_{\lambda - \mu} \right\} \Big|_q, \quad (232)$$

where \mathcal{N} is a normalization factor.

For actual numerical calculations one needs to determine the model parameters. The average field for neutrons and protons is described in the QPM by phenomenologic Woods–Saxon potential:

$$U^{\tau}(r) = \frac{V_0^{\tau}}{1 + e^{(r-R_0^{\tau})/a_0^{\tau}}} - \frac{\hbar^2}{\mu^2 c^2} \frac{1}{r} \frac{d}{dr} \left(\frac{V_{ls}^{\tau}}{1 + e^{(r-R_{ls}^{\tau})/a_{ls}^{\tau}}} \mathbf{l} \cdot \mathbf{s} \right) + V_C(r). \quad (233)$$

The parameters of this potential for different A-mass regions are listed in Table 9 (see, also Ref. [87]). We usually use $R_{ls}^{\tau} = R_0^{\tau}$, $a_{ls}^{\tau} = a_0^{\tau}$, and $R_C = R_0^p$. All single-particle levels from the bottom are included in calculation. The single-particle continuum is approximated by narrow quasibound states. This approximation gives a good description of the exhaust of the energy weighted sum rules (EWSR) for low values of λ in medium and heavy nuclei. For the lead region we use the single-particle spectrum near the Fermi surface from Ref. [88] which was adjusted to achieve a correct description of low-lying states in neighboring odd nuclei. The parameters of the monopole $G_{\tau}^{(0)}$ have been fitted to reproduce the pairing energies.

The parameters of the residual interaction are obtained the following way. The strength of the residual interaction for $\lambda^{\pi} = 2^+$ and 3^- is adjusted to reproduce the properties (excitation energy and $B(E\lambda)$ value, known from experiment) of the 2_1^+ and 3_1^- states. Usually it is not possible within one-phonon approximation, discussed in this subsection, if sufficiently large single-particle spectrum is used. When the energy of the lowest excitation is adjusted to the experimental value, the RPA equation yields an overestimated collectivity, $B(E\lambda)$ value, for this state. And vice versa, if the collectivity of this state is reproduced, the excitation energy is too high as compared to the experimental value. The situation sufficiently improves when the coupling of one-phonon states to

more complex configurations is taken into account as will be discussed in the next subsection. For the lowest excited state the coupling to complex configurations results in the energy shift downwards. Thus, for nuclei not very far from a closed shell it becomes possible to achieve a good description of both, the excitation energy and the $B(E\lambda)$ value. The ratio between isoscalar and isovector strength of the residual interaction is usually fixed as $\kappa_1^{(\lambda)}/\kappa_0^{(\lambda)} = -1.2$ in calculation with the radial formfactor of the multipole operator as a derivative of the average field. With this ratio the best description of isovector multipole resonances with $\lambda > 1$ is achieved although the experimental information on these resonances is still sparse. For the dipole–dipole residual interaction the strength parameter are adjusted to exclude the spurious center of mass motion and to obtain a correct position of the GDR centroid. For the phonons with the multipolarity $\lambda \geq 4$ the same procedure of adjusting the strength parameters as for $\lambda^\pi = 2^+$ and 3^- cannot be applied. First, it is because the lowest states of high multipolarity are much less collective and their properties are more sensitive to description of single-particle levels near the Fermi surface than to the strength of the residual interaction. Second, in many cases the lowest states with $\lambda \geq 4$ are either two-phonon states or the states with a large admixture of two-phonon configurations, thus, their properties are determined by phonons of another multipolarity. For these reasons we use $\kappa_{0,1}^{(\lambda)} = \kappa_{0,1}^{(2^+)}$ for even parity phonons and $\kappa_{0,1}^{(\lambda)} = \kappa_{0,1}^{(3^-)}$ for odd parity in calculation with $f_\lambda^\tau(r) = dU^\tau(r)/dr$. In fact, the difference between $\kappa_{0,1}^{(2^+)}$ and $\kappa_{0,1}^{(3^-)}$ does not exceed a few percent with this radial formfactor of residual force.

4.2. Mixing between simple and complex configurations in wave functions of excited states

Diagonalization of the model Hamiltonian in the space of one-phonon states allows us to write it in the form

$$H = \sum_{\lambda\mu i} \omega_{\lambda i} Q_{\lambda\mu i}^+ Q_{\lambda\mu i} + H_{\text{int.}}, \quad (234)$$

$$H_{\text{int.}} = -\frac{1}{2} \sum_{\lambda\mu i} \left\{ [(-1)^{\lambda-\mu} Q_{\lambda\mu i}^+ + Q_{\lambda-\mu i}] \sum_{jj'\tau} \frac{f_{jj'}^\lambda v_{jj'}^{(-)}}{\sqrt{2\mathcal{Y}_{\tau}^{\lambda i}}} B_\tau(jj'; \lambda - \mu) + \text{h.c.} \right\}, \quad (235)$$

where the origin of the second term in Eq. (234) can be traced back to the last term of multipole operator (223) which cannot be projected onto the space of the phonon operators. On the other hand, applying Marumori expansion technique [89], one may expand the operator $B_\tau(jj'; \lambda - \mu) \sim \alpha^+ \alpha$ in an infinite sum of even-number phonon operators. Keeping only the first term of this expansion, the non-diagonal term of the model Hamiltonian, $H_{\text{int.}}$, in the space of phonon operators may be re-written as

$$H_{\text{int.}} = \sum_{\substack{\lambda \\ \lambda\mu i \\ \lambda_1\mu_1 i_1 \\ \lambda_2\mu_2 i_2}}^{\lambda} U_{\lambda_2 i_2}^{\lambda_1 i_1}(\lambda i) Q_{\lambda\mu i}^+ [Q_{\lambda_1\mu_1 i_1} Q_{\lambda_2\mu_2 i_2}]_{\lambda\mu} + \text{h.c.}, \quad (236)$$

where the matrix element of interaction between one- and two-phonon configurations, $U_{\lambda_2 \lambda_1}^{\lambda_1 i_1}(\lambda i)$, can be calculated by making use of the internal fermion structure of phonons, i.e. ψ and φ coefficients, and reduced matrix elements of the separable force formfactor, $f_{j_1 j_2}^\lambda$. It has the form

$$\begin{aligned}
 U_{\lambda_2 \lambda_1}^{\lambda_1 i_1}(\lambda i) &= \langle Q_{\lambda i} | H [Q_{\lambda_1 i_1}^+ Q_{\lambda_2 i_2}^+]_{\lambda} \rangle = (-1)^{\lambda_1 + \lambda_2 - \lambda} \sqrt{\frac{(2\lambda_1 + 1)(2\lambda_2 + 1)}{2}} \\
 &\times \sum_{\tau} \sum_{j_1 j_2 j_3}^{n, p} \left[\frac{f_{j_1 j_2}^{\lambda} v_{j_1 j_2}^{(\mp)}}{\sqrt{\mathcal{Y}_{\tau}^{\lambda i}}} \begin{Bmatrix} \lambda_1 & \lambda_2 & \lambda \\ j_2 & j_1 & j_3 \end{Bmatrix} \left\{ \psi_{j_3 j_1}^{\lambda_1 i_1} \varphi_{j_2 j_3}^{\lambda_2 i_2} \pm \psi_{j_2 j_3}^{\lambda_2 i_2} \varphi_{j_3 j_1}^{\lambda_1 i_1} \right\} \right. \\
 &+ \frac{f_{j_1 j_2}^{\lambda} v_{j_1 j_2}^{(\mp)}}{\sqrt{\mathcal{Y}_{\tau}^{\lambda_1 i_1}}} \begin{Bmatrix} \lambda_1 & \lambda_2 & \lambda \\ j_3 & j_2 & j_1 \end{Bmatrix} \left\{ \varphi_{j_2 j_3}^{\lambda_2 i_2} \varphi_{j_3 j_1}^{\lambda_1 i_1} \pm \psi_{j_2 j_3}^{\lambda_2 i_2} \psi_{j_3 j_1}^{\lambda_1 i_1} \right\} \\
 &\left. + \frac{f_{j_1 j_2}^{\lambda} v_{j_1 j_2}^{(\mp)}}{\sqrt{\mathcal{Y}_{\tau}^{\lambda_2 i_2}}} \begin{Bmatrix} \lambda_1 & \lambda_2 & \lambda \\ j_1 & j_3 & j_2 \end{Bmatrix} \left\{ \psi_{j_3 j_1}^{\lambda_1 i_1} \psi_{j_2 j_3}^{\lambda_2 i_2} \pm \varphi_{j_3 j_1}^{\lambda_1 i_1} \varphi_{j_2 j_3}^{\lambda_2 i_2} \right\} \right]. \quad (237)
 \end{aligned}$$

The upper (lower) sign in each of three terms in Eq. (237) correspond to multipole (spin-multipole) matrix element $f_{j_1 j_2}^{\lambda}$, $f_{j_1 j_2}^{\lambda_1}$ or $f_{j_1 j_2}^{\lambda_2}$, respectively.

Thus, we have completed a projection of the nuclear Hamiltonian into the space of phonon operators. Now we may assume that phonons obey boson statistics and work in the space of boson operators only. The presence of the term of interaction, H_{int} , in the model Hamiltonian means that the approximation, in which excited states of the nucleus are considered as pure one-, two-, multi-phonon states, is not sufficient. In fact, we have already mentioned above that it is not possible to describe the properties of the lowest collective vibrations in spherical nuclei in one-phonon approximation. It is also well-known that the coupling between one- and two-phonon configurations is the main mechanism for the damping of giant resonances. All this means that one needs to go beyond the approximation of independent phonons and take into account a coupling between them. To accomplish this task we write the wave function of excited states with angular momentum J and projection M in even-even nuclei in the most general form as a mixture of one-, two-, etc. phonon configurations:

$$\begin{aligned}
 \Psi^v(JM) &= \left\{ \sum_{\alpha_1} S_{\alpha_1}^v(J) Q_{\alpha_1}^+ + \sum_{\alpha_2 \beta_2} \frac{D_{\alpha_2 \beta_2}^v(J)}{\sqrt{1 + \delta_{\alpha_2, \beta_2}}} [Q_{\alpha_2}^+ Q_{\beta_2}^+]_{JM} \right. \\
 &\left. + \sum_{\alpha_3 \beta_3 \gamma_3} \frac{T_{\alpha_3 \beta_3 \gamma_3}^v(J)}{\sqrt{1 + \delta_{\alpha_3, \beta_3, \gamma_3}}} [Q_{\alpha_3}^+ Q_{\beta_3}^+ Q_{\gamma_3}^+]_{JM} + \dots \right\} \Bigg|_{ph}, \quad (238)
 \end{aligned}$$

$$\delta_{\alpha_3, \beta_3, \gamma_3} = \delta_{\alpha_3, \beta_3} + \delta_{\alpha_3, \gamma_3} + \delta_{\beta_3, \gamma_3} + 2\delta_{\alpha_3, \beta_3} \delta_{\alpha_3, \gamma_3}. \quad (239)$$

By greek characters we mean the phonon's identity, i.e. its multipolarity and order number, $\alpha \equiv \lambda^{\pi} i$, the index v ($= 1, 2, 3, \dots$) labels whether a state J is the first, second, etc., state in the total energy spectrum of the system. It is assumed that any combination α, β, γ of phonons appears only once. The second and the third terms in Eq. (238) include phonons of different multiplicities and parities, they only must couple to the same total angular momentum J as the one-phonon term.

Let us limit the wave function of excited states by three-phonon terms and diagonalize the model Hamiltonian of Eqs. (234) and (236) in the space of these states. We use for that a minimization procedure

$$\delta\{\langle\Psi^v(JM)|H|\Psi^v(JM)\rangle - E_x^J\langle\Psi^v(JM)|\Psi^v(JM)\rangle\} = 0, \quad (240)$$

which yields a set of linear equations over unknown wave function coefficients $S_{\alpha_1}^v(J)$, $D_{\alpha_2\beta_2}^v(J)$ and $T_{\alpha_3\beta_3\gamma_3}^v(J)$:

$$\begin{aligned} (\omega_{\alpha_1} - E_x^J)S_{\alpha_1}^v(J) + \sum_{\alpha_2,\beta_2} D_{\alpha_2\beta_2}^v(J)\tilde{U}_{\alpha_2\beta_2}^{\alpha_1} &= 0, \\ \sum_{\alpha_1} S_{\alpha_1}^v(J)\tilde{U}_{\alpha_2\beta_2}^{\alpha_1} + (\omega_{\alpha_2} + \omega_{\beta_2} - E_x^J)D_{\alpha_2\beta_2}^v(J) + \sum_{\alpha_3\beta_3\gamma_3} T_{\alpha_3\beta_3\gamma_3}^v(J)\tilde{U}_{\alpha_3\beta_3\gamma_3}^{\alpha_2\beta_2} &= 0, \\ \sum_{\alpha_2\beta_2} D_{\alpha_2\beta_2}^v(J)\tilde{U}_{\alpha_3\beta_3\gamma_3}^{\alpha_2\beta_2} + (\omega_{\alpha_3} + \omega_{\beta_3} + \omega_{\gamma_3} - E_x^J)T_{\alpha_3\beta_3\gamma_3}^v(J) &= 0. \end{aligned} \quad (241)$$

Applying boson commutation relations for phonons, the matrix element of interaction between two- and three-phonon configurations,

$$\tilde{U}_{\alpha_3\beta_3\gamma_3}^{\alpha_2\beta_2} = \sqrt{1 + \delta_{\alpha_2,\beta_2}}\sqrt{1 + \delta_{\alpha_3,\beta_3,\gamma_3}}\langle[Q_{\alpha_2}Q_{\beta_2}]_{JM}|H_{\text{int.}}|[Q_{\alpha_3}^+Q_{\beta_3}^+Q_{\gamma_3}^+]_{JM}\rangle, \quad (242)$$

can be expressed as a function of matrix elements of interaction between one- and two-phonon configurations,

$$\tilde{U}_{\alpha_2\beta_2}^{\alpha_1} = \sqrt{1 + \delta_{\alpha_2,\beta_2}}\langle Q_{\alpha_1}|H_{\text{int.}}|[Q_{\alpha_2}^+Q_{\beta_2}^+]_{JM}\rangle = \sqrt{1 + \delta_{\alpha_2,\beta_2}}U_{\alpha_2}^{\beta_2}(\alpha_1), \quad (243)$$

as follows:

$$\begin{aligned} \tilde{U}_{\alpha_3\beta_3\gamma_3}^{\alpha_2\beta_2} &= \sqrt{1 + \delta_{\beta_3,\gamma_3}}[\tilde{U}_{\beta_3\gamma_3}^{\alpha_2}\delta_{\beta_2,\alpha_3} + \tilde{U}_{\beta_3\gamma_3}^{\beta_2}\delta_{\alpha_2,\alpha_3}] \\ &+ \sqrt{1 + \delta_{\alpha_3,\gamma_3}}[\tilde{U}_{\alpha_3\gamma_3}^{\alpha_2}\delta_{\beta_2,\beta_3} + \tilde{U}_{\alpha_3\gamma_3}^{\beta_2}\delta_{\alpha_2,\beta_3}] + \sqrt{1 + \delta_{\alpha_3,\beta_3}}[\tilde{U}_{\alpha_3\beta_3}^{\alpha_2}\delta_{\beta_2,\gamma_3} + \tilde{U}_{\alpha_3\beta_3}^{\beta_2}\delta_{\alpha_2,\gamma_3}] \end{aligned} \quad (244)$$

and the value $\tilde{U}_{\alpha_2}^{\beta_2}(\alpha_1)$ is calculated according to Eq. (237). Since we have used pure boson commutation relations for phonons the two-phonon configuration $[\alpha_2\beta_2]_J$ couples only to those three-phonon configurations $[\alpha_3\beta_3\gamma_3]_J$ where either α_3 , β_3 or γ_3 are equal to α_2 or β_2 . This is governed by δ -functions in Eq. (244).

The number of linear equations (241) equals to the number of one-, two- and three-phonon configurations included in the wave function (238). Solving these equations we obtain the energy spectrum E_v^J of excited states described by wave function (238) and the coefficients of wave function (241), S , D and T .

It should be pointed out that within this approximation, in which phonons are considered as ideal bosons and nuclear Hamiltonian includes one-phonon exchange term, multi-phonon configurations of course possess no anharmonicity features. The strength of any one- or many-phonon configuration included in the wave function (238) fragments over some energy interval due to the interaction with other configurations. But the centroid of the strength distribution remains at the unperturbed energy. Thus, the energy centroid of two-phonon configuration

$[\alpha_2\beta_2]_J$ equals exactly to the sum of energies of α_2 and β_2 phonons for all values of J . To consider anharmonic properties of multi-phonon states, one needs to go beyond pure boson features of excitations in even–even nuclei and take into account their internal fermion structure.

Another reason to return back to the fermion origin of phonon excitations is two main problems in considering multi-phonon states associated with the boson mapping procedure. The first problem is an admixture of spurious $n\bar{p}n\bar{h}$ configurations which violate Pauli principle in the wave function of n -phonon state. The second is related to the fact that the set of pure n -phonon states is mathematically non-orthonormal if the internal fermion structure of phonons is taken into account (see Refs. [90,91] for more details). To overcome these problems we will keep on using a phonon's imaging of nuclear excitation and use the same expression for the wave function of excited states (238) but in calculation of the norm of this wave function, $\langle\Psi^v(JM)|\Psi^v(JM)\rangle$, and the energy of this state, $\langle\Psi^v(JM)|H|\Psi^v(JM)\rangle$, we will use exact commutation relations between phonon operators:

$$[Q_{\lambda\mu i}, Q_{\lambda'\mu' i'}^+]_- = \delta_{\lambda,\lambda'}\delta_{\mu,\mu'}\delta_{i,i'} - \sum_{\substack{jj'j_2 \\ mm'm_2}} \alpha_{jm}^+\alpha_{j'm'} \\ \times \{\psi_{j'j_2}^{\lambda i} \psi_{jj_2}^{\lambda' i'} C_{j'm'j_2m_2}^{\lambda\mu} C_{jmj_2m_2}^{\lambda'\mu'} - (-)^{\lambda+\lambda'+\mu+\mu'} \varphi_{jj_2}^{\lambda i} \varphi_{j'j_2}^{\lambda' i'} C_{jmj_2m_2}^{\lambda-\mu} C_{j'm'j_2m_2}^{\lambda'-\mu'}\} \quad (245)$$

and exact commutation relations between phonon and quasiparticle operators:

$$[\alpha_{jm}, Q_{\lambda\mu i}^+]_- = \sum_{j'm'} \psi_{jj'}^{\lambda i} C_{jmj'm'}^{\lambda\mu} \alpha_{j'm'}^+, \\ [\alpha_{jm}^+, Q_{\lambda\mu i}^+]_- = (-1)^{\lambda-\mu} \sum_{j'm'} \varphi_{jj'}^{\lambda i} C_{jmj'm'}^{\lambda-\mu} \alpha_{j'm'}^+. \quad (246)$$

Also we will not expand the operator $B_\tau(jj'; \lambda\mu)$ in Eq. (235) into a sum of phonon operators but use its exact fermion structure. The first term of Eq. (245) corresponds to the ideal boson approximation while the second one is a correction due to the fermion structure of phonon operators. The overlap matrix elements between different two-phonon configurations modify as

$$\langle[Q_{\beta'} Q_{\alpha'}]_J|[Q_{\alpha}^+ Q_{\beta}^+]_J\rangle = \langle[b_{\beta'} b_{\alpha'}]_J|[b_{\alpha}^+ b_{\beta}^+]_J\rangle + K^J(\beta'\alpha'|\alpha\beta), \quad (247)$$

where b_{α}^+ is the ideal boson operator and the quantity K ,

$$K^J(\beta'\alpha'|\alpha\beta) = K^J(\lambda_4 i_4 \lambda_3 i_3 |\lambda_1 i_1 \lambda_2 i_2) = \sqrt{(2\lambda_1 + 1)(2\lambda_2 + 1)(2\lambda_3 + 1)(2\lambda_4 + 1)} \\ \times (-1)^{\lambda_2 + \lambda_4} \sum_{\substack{j_1 j_2 \\ j_3 j_4}} (-1)^{j_2 + j_4} \begin{pmatrix} j_1 & j_2 & \lambda_4 \\ j_4 & j_3 & \lambda_3 \\ \lambda_1 & \lambda_2 & J \end{pmatrix} (\psi_{j_3 j_4}^{\lambda_3 i_3} \psi_{j_1 j_4}^{\lambda_1 i_1} \psi_{j_3 j_2}^{\lambda_2 i_2} \psi_{j_1 j_2}^{\lambda_4 i_4} - \varphi_{j_3 j_4}^{\lambda_3 i_3} \varphi_{j_1 j_4}^{\lambda_1 i_1} \varphi_{j_3 j_2}^{\lambda_2 i_2} \varphi_{j_1 j_2}^{\lambda_4 i_4}), \quad (248)$$

is the Pauli principle correction coefficient. The experience of realistic calculations shows that usually $|K^J(\beta\alpha|\alpha\beta)| \gg |K^J(\beta'\alpha'|\alpha\beta)|$ (where $\alpha \neq \alpha'$ and/or $\beta \neq \beta'$) and that the so-called diagonal Pauli principle approximation, $K^J(\beta'\alpha'|\alpha\beta) = K^J(\alpha\beta)\delta_{\alpha,\alpha'}\delta_{\beta,\beta'}$, provides rather good accuracy and sufficiently simplifies the calculation. For these reasons we will use this diagonal Pauli principle approximation in what follows.

A similar expression, as (247), is valid for the overlap matrix elements between different three-phonon configurations. It can be used as a definition of the Pauli principle correction quantity $K_I^J(\gamma' \beta' \alpha' | \alpha \beta \gamma)$ which we will also keep in diagonal approximation only. The relation between $K^J(\alpha \beta)$ and $K_I^J(\alpha \beta \gamma)$ quantities is the following [92]:

$$K_I^J(\alpha \beta \gamma) = K^J(\alpha \beta) \left(3 + \sum_{I'} \overline{U^2}(\alpha \beta J \gamma; I, I') K^{I'}(\beta \gamma) \right), \quad (249)$$

where $\overline{U^2}$ stands for the Jahn coefficients [93].

When internal fermion structure of phonons is taken into account and exact commutation relations (245), (246) are applied the secular equation (241) transforms into

$$\begin{aligned} (\omega_{\alpha_1} - E_x^J) S_{\alpha_1}^v(J) + \sum_{\alpha_2, \beta_2} D_{\alpha_2 \beta_2}^v(J) \tilde{U}_{\alpha_2 \beta_2}^{\alpha_1} &= 0, \\ \sum_{\alpha_1} S_{\alpha_1}^v(J) \tilde{U}_{\alpha_2 \beta_2}^{\alpha_1} + (\omega_{\alpha_2} + \omega_{\beta_2} + \Delta \omega_{\alpha_2 \beta_2}^J - E_x^J) D_{\alpha_2 \beta_2}^v(J) + \sum_{\alpha_3 \beta_3 \gamma_3} T_{\alpha_3 \beta_3 \gamma_3}^v(J) \tilde{U}_{\alpha_3 \beta_3 \gamma_3}^{\alpha_2 \beta_2} &= 0, \\ \sum_{\alpha_2 \beta_2} D_{\alpha_2 \beta_2}^v(J) \tilde{U}_{\alpha_3 \beta_3 \gamma_3}^{\alpha_2 \beta_2} + (\omega_{\alpha_3} + \omega_{\beta_3} + \omega_{\gamma_3} + \Delta \omega_{\alpha_3 \beta_3 \gamma_3}^J - E_x^J) T_{\alpha_3 \beta_3 \gamma_3}^v(J) &= 0. \end{aligned} \quad (250)$$

The values $\Delta \omega_{\alpha_2 \beta_2}^J$ and $\Delta \omega_{\alpha_3 \beta_3 \gamma_3}^J = \Delta \omega_{\alpha_3 \beta_3}^J + \Delta \omega_{\beta_3 \gamma_3}^J + \Delta \omega_{\alpha_3 \gamma_3}^J$ are anharmonicity shifts of two- and three-phonon configurations, respectively, due to the Pauli principle corrections. In diagonal approximation they can be calculated according to

$$\Delta \omega_{\alpha_2 \beta_2}^J = - \frac{K^J(\alpha_2 \beta_2)}{4} \sum_{\tau}^{n,p} \left[\frac{X_{\tau}^{\alpha_2}}{\mathcal{Y}_{\tau}^{\alpha_2}} + \frac{X_{\tau}^{\beta_2}}{\mathcal{Y}_{\tau}^{\beta_2}} \right]. \quad (251)$$

Another role of Pauli principle corrections is a somewhat renormalization of the interaction between n - and $(n+1)$ -phonon configurations. We have used the same notations for these matrix elements $\tilde{U}_{\alpha_2 \beta_2}^{\alpha_1}$ as in the case of the “ideal boson approximation” (see, Eqs. (242) and (243)). But calculating the matrix elements $\langle Q_{\alpha_1} | H_{\text{int.}} | [Q_{\alpha_2}^+ Q_{\beta_2}^+]_{JM} \rangle$ we take into account the fermion structure of phonons and nuclear Hamiltonian and obtain

$$\tilde{U}_{\alpha_2 \beta_2}^{\alpha_1} = \sqrt{1 + \delta_{\alpha_2, \beta_2}} U_{\alpha_2}^{\beta_2}(\alpha_1) \times [1 + \frac{1}{2} K^J(\alpha_2 \beta_2)], \quad (252)$$

where the value $U_{\alpha_2}^{\beta_2}(\alpha_1)$ is calculated again according to Eq. (237). A similar additional factor $[1 + 1/2 \times K_I^J(\alpha_3 \beta_3 \gamma_3)]$ receives the matrix element of interaction between two- and three-phonon configurations.

The minimal value of the quantity $K^J(\alpha \beta)$ equals to -2 . It corresponds to the case of the maximal Pauli principle violation, i.e. to a spurious multi-phonon configuration. It happens only when α_2 and β_2 phonons are purely two-quasiparticle states. In such a case the matrix element of interaction $\tilde{U}_{\alpha_2 \beta_2}^{\alpha_1} \equiv 0$ (see Eq. (252)) and the spurious state is completely separated from other states. While dealing with collective α_2 and β_2 phonons, when a possible admixture of the spurious four-quasiparticle configurations is small, the value of $K^J(\alpha \beta)$ is close to 0. Nevertheless, the value of the anharmonicity shift $\Delta \omega_{\alpha_2 \beta_2}^J$ is not vanishingly small for the later because of the relatively large value of the ratio $X_{\tau}^{\alpha} / \mathcal{Y}_{\tau}^{\alpha}$ in Eq. (251). This shift is the largest one for the collective low-lying

multi-phonon configurations. For non-collective multi-phonon states the shift is small because of the small value of the above-mentioned ratio.

Equations (250) have been obtained under two main assumptions. The first one is the already discussed diagonal Pauli principle approximation. The second assumption is the neglecting of the higher-order terms of the interaction part of the nuclear Hamiltonian as compared to the one in Eq. (236) which couples n - and $(n \pm 1)$ -phonon configurations. For Eqs. (250) it means that a direct coupling between one- and three-phonon configurations of the wave function (238) which is possible due to non-zero matrix element $\langle Q_{\alpha_1} | \alpha_{jm} \alpha_{jml} [Q_{\alpha_3}^+ Q_{\beta_3}^+ Q_{\gamma_3}^+]_{JM} \rangle$, is neglected. In realistic calculation we will also use a selection of three-phonon configurations provided by Eq. (244) although now the matrix element $\tilde{U}_{\alpha_3 \beta_3 \gamma_3}^{\alpha_2 \beta_2} \neq 0$ even if one of α_3 , β_3 or γ_3 is not necessarily equal to α_2 or β_2 . These omitted matrix elements are orders of magnitude smaller as compared to the accounted for ones.

Solving the system of linear equations (250) we obtain the spectrum of excited states, E_v^J , described by the wave function (238) and coefficients $S_{\alpha_1}^v(J)$, $D_{\alpha_2 \beta_2}^v(J)$ and $T_{\alpha_3 \beta_3 \gamma_3}^v(J)$ reflecting the phonon structure of excited states. Usually, in calculation of the properties of single giant resonances the three-phonon terms of the wave function (238) are omitted. Then it is possible to solve the system of linear equations (250) with the rank of the 10^3 – 10^4 order by a direct diagonalization. But while considering the damping properties of two-phonon resonances, three-phonon configurations cannot be omitted. For this case instead of the diagonalization of the linear matrices of very high orders, an alternative solution is possible. We may substitute the first and last equations of (250) into the second equation and obtain the system of non-linear equations

$$\det \left\| \left(\omega_{\alpha_2} + \omega_{\beta_2} + \Delta \omega_{\alpha_2 \beta_2}^J - E_x^J \right) \delta_{\alpha_2 \beta_2, \alpha_2 \beta_2} - \sum_{\alpha_1} \frac{\tilde{U}_{\alpha_2 \beta_2}^{\alpha_1} \tilde{U}_{\alpha_2 \beta_2}^{\alpha_1}}{\omega_{\alpha_1} - E_x^J} - \sum_{\alpha_3 \beta_3 \gamma_3} \frac{\tilde{U}_{\alpha_3 \beta_3 \gamma_3}^{\alpha_2 \beta_2} \tilde{U}_{\alpha_3 \beta_3 \gamma_3}^{\alpha_2 \beta_2}}{\omega_{\alpha_3} + \omega_{\beta_3} + \omega_{\gamma_3} + \Delta \omega_{\alpha_3 \beta_3 \gamma_3}^J - E_x^J} \right\| = 0, \quad (253)$$

the rank of which equals to the number of two-phonon configurations included in the wave function (238). The solution of the system (253) by some iterative method yield again the spectrum of excited states E_v^J and coefficients $D_{\alpha_2 \beta_2}^v(J)$. Other coefficients of the wave function (238) are related to these coefficients as follows:

$$S_{\alpha_1}^v(J) = - \frac{\sum_{\alpha_2 \beta_2} D_{\alpha_2 \beta_2}^v(J) \tilde{U}_{\alpha_2 \beta_2}^{\alpha_1}}{\omega_{\alpha_1} - E_x^v},$$

$$T_{\alpha_3 \beta_3 \gamma_3}^v(J) = - \frac{\sum_{\alpha_2 \beta_2} D_{\alpha_2 \beta_2}^v(J) \tilde{U}_{\alpha_3 \beta_3 \gamma_3}^{\alpha_2 \beta_2}}{\omega_{\alpha_3} + \omega_{\beta_3} + \omega_{\gamma_3} + \Delta \omega_{\alpha_3 \beta_3 \gamma_3}^J - E_v^J}. \quad (254)$$

It may be argued that the boson mapping with keeping the fermion information of the phonons' images at all stages of transformations gives no advantage as compared to n pnh approach since, mathematically, a direct correspondence between two methods can be established only if the full basis of n -phonon states is used. However, many n pnh configurations interact very weakly with other ones and as a result practically do not mix with them. It allows a sufficient truncation of multi-phonon configurations in the wave function (238) based on their physical properties with keeping a good accuracy for the components important for the subject of

research. From the point of view of the Pauli principle violation the most dangerous multi-phonon configurations are the ones made of non-collective RPA states. On the other hand, these configurations interact with the other ones much weaker than the multi-phonon configurations including at least one collective phonon. For these reasons the first are not accounted for in the wave function (238) in realistic calculation. As the criteria “collective/non-collective” we take the contribution of the main two-quasiparticle component to the wave function of the phonon operator. If the contribution exceeds 50–60% we will call the phonon non-collective.

Let us consider now the electromagnetic excitation of pure one- and multi-phonon states from the ground state. The one-body operator of electromagnetic transition has the form

$$\mathcal{M}(E\lambda\mu) = \sum_{\tau}^{n,p} e_{\tau}^{(\lambda)} \sum_{\substack{jj' \\ mm'}} (-1)^{j'+m'} \frac{\langle j||E\lambda||j' \rangle}{\sqrt{2\lambda+1}} C_{jmj'm'}^{\lambda\mu} a_{jm}^{+} a_{j'm'}^{-}, \quad (255)$$

where the single-particle transition matrix element $\langle j||E\lambda||j' \rangle \equiv \langle j||i^{\lambda} Y_{\lambda r^{\lambda}}||j' \rangle$ and $e_{\tau}^{(\lambda)}$ are effective charges for neutrons and protons. In calculations we use the following values of effective charges: $e_n^{(1)} = -Z/A$ and $e_p^{(1)} = N/A$ to separate the center of mass motion and $e_n^{(\lambda \neq 1)} = 0$ and $e_p^{(\lambda \neq 1)} = 1$. Performing the transformation from particle operators to quasiparticle and phonon ones in Eq. (255), this equation transforms into

$$\begin{aligned} \mathcal{M}(E\lambda\mu) = & \sum_{\tau}^{n,p} e_{\tau}^{(\lambda)} \sum_{jj'} \frac{\langle j||E\lambda||j' \rangle}{\sqrt{2\lambda+1}} \left\{ \frac{u_{jj'}^{(+)}}{2} \sum_i (\psi_{jj'}^{\lambda i} + \varphi_{jj'}^{\lambda i}) (Q_{\lambda\mu i}^{+} + (-)^{\lambda-\mu} Q_{\lambda-\mu i}) \right. \\ & \left. + v_{jj'}^{(-)} \sum_{mm'} C_{jmj'm'}^{\lambda\mu} (-)^{j'+m'} \alpha_{j'm'}^{+} \alpha_{j'-m'}^{-} \right\}, \quad (256) \end{aligned}$$

where the first term corresponds to one-phonon exchange between initial and final states and the second one is responsible for “boson-forbidden” electromagnetic transitions (see for details Ref. [94]). Then the reduced matrix element of the electromagnetic excitation of the one-phonon state λi from the ground state $0_{\text{g.s.}}^{+}$ in even–even nuclei may be calculated according to

$$\langle Q_{\lambda i} || \mathcal{M}(E\lambda) || 0_{\text{g.s.}}^{+} \rangle = \sum_{\tau}^{n,p} e_{\tau}^{(\lambda)} \sum_{j_1 j_2} \frac{1}{2} \langle j_1 || E\lambda || j_2 \rangle u_{j_1 j_2}^{(+)} (\psi_{j_1 j_2}^{\lambda i} + \varphi_{j_1 j_2}^{\lambda i}). \quad (257)$$

Due to the ground-state correlations the direct excitation of pure two-phonon states $[Q_{\lambda_1 i_1}^{+} \times Q_{\lambda_2 i_2}^{+}]_{\lambda}$ from the ground state is also possible when we are dealing with the RPA phonons. The physical reason for that becomes clear if we remember that the ground state wave function includes a small admixture of four-, eight-, etc. quasiparticle configurations (see, Eq. (232)). The second term of Eq. (256) is responsible for these transitions and the reduced matrix element can be obtained by applying the commutation relations (246). It has the form

$$\begin{aligned} \langle [Q_{\lambda_2 i_2} \times Q_{\lambda_1 i_1}]_{\lambda} || \mathcal{M}(E\lambda) || 0_{\text{g.s.}}^{+} \rangle = & \sqrt{(2\lambda_1+1)(2\lambda_2+1)} \sum_{\tau}^{n,p} e_{\tau}^{(\lambda)} \sum_{j_1 j_2 j_3} v_{j_1 j_2}^{(-)} \\ & \times \langle j_1 || E\lambda || j_2 \rangle \begin{Bmatrix} \lambda_2 & \lambda_1 & \lambda \\ j_1 & j_2 & j_3 \end{Bmatrix} \left\{ \psi_{j_2 j_3}^{\lambda_2 i_2} \varphi_{j_3 j_1}^{\lambda_1 i_1} + \psi_{j_3 j_1}^{\lambda_1 i_1} \varphi_{j_2 j_3}^{\lambda_2 i_2} \right\}. \quad (258) \end{aligned}$$

Another type of boson-forbidden γ -transitions which take place due to the internal fermion structure of phonons are the ones between one-phonon initial, $Q_{\lambda_1 i_1}^+ | \rangle_{ph}$, and final, $Q_{\lambda_2 i_2}^+ | \rangle_{ph}$, states. The reduced matrix element of such transitions can be calculated according to

$$\begin{aligned} \langle Q_{\lambda_2 i_2} | \mathcal{M}(E\lambda) | Q_{\lambda_1 i_1}^+ \rangle &= \sqrt{2\lambda_2 + 1} \sum_{\tau}^{n,p} e_i^{(\lambda)} \sum_{j_1 j_2 j_3} v_{j_1 j_2}^{(-)} \langle j_1 | E\lambda | j_2 \rangle \\ &\times \begin{Bmatrix} \lambda_1 & \lambda_2 & \lambda \\ j_1 & j_2 & j_3 \end{Bmatrix} (\psi_{j_2 j_3}^{\lambda_1 i_1} \psi_{j_3 j_1}^{\lambda_2 i_2} + \varphi_{j_2 j_3}^{\lambda_1 i_1} \varphi_{j_3 j_1}^{\lambda_2 i_2}). \end{aligned} \quad (259)$$

The matrix element for transitions between the two-phonon states $[Q_{\lambda_1 i_1}^+ \times Q_{\lambda_2 i_2}^+]_{\lambda'}$ and $[Q_{\lambda_3 i_3}^+ \times Q_{\lambda_4 i_4}^+]_{\lambda''}$ is very complex and not presented here. Its first-order term is very similar to the one for transitions between the one-phonon states $Q_{\lambda_1 i_1}^+ | \rangle_{ph}$ and $Q_{\lambda_4 i_4}^+ | \rangle_{ph}$ and may be obtained by assuming that the fermion structure of one phonon is “frozen”, i.e., assuming that $\lambda_2 i_2 \equiv \lambda_3 i_3$.

When the coupling between one- and multi-phonon configurations is accounted for in the wave function of excited states, the reduced matrix element of the electromagnetic excitation of the states of Eq. (238) may be written as

$$\begin{aligned} \langle \Psi^v(J) | \mathcal{M}(E\lambda) | 0_{g.s.}^+ \rangle &= \left\{ \sum_{\alpha_1} S_{\alpha_1}^v(J) \langle Q_{\lambda i} | \mathcal{M}(E\lambda) | 0_{g.s.}^+ \rangle \right. \\ &\quad \left. + \sum_{\alpha_2 \beta_2} \frac{D_{\alpha_2 \beta_2}^v(J)}{\sqrt{1 + \delta_{\alpha_2, \beta_2}}} \langle [Q_{\lambda_2 i_2} \times Q_{\lambda_1 i_1}]_{\lambda} | \mathcal{M}(E\lambda) | 0_{g.s.}^+ \rangle \right\}, \end{aligned} \quad (260)$$

where we have neglected the direct excitation of three-phonon configurations from the ground state. Since an admixture of multi-quasiparticle configurations in the ground-state wave function is very small, the reduced matrix element, Eq. (258), is typically about two orders of magnitude smaller as compared to the reduced matrix element, Eq. (257). For this reason, in most of the cases keeping only the first term in Eq. (260) and neglecting the second one together with interference effects provides very good accuracy in calculation. Nevertheless, there are a few exceptional cases.

The first one is the excitation of the lowest 1^- state in spherical nuclei. It is well known that no collective one-phonon 1^- configurations appear in the low-energy region and the wave function of the 1_1^- state has the dominant two-phonon component $[2_1^+ \times 3_1^-]_{1^-}$. There are three main mechanisms to explain the $E1$ -excitation of this state observed in the experiment [95]. The first is an influence of the GDR. In microscopic theories it appears in a natural way due to the coupling of one- and two-phonon configurations. Since the GDR is located about 10 MeV higher, this coupling yields only a very small portion of the observed strength. The second mechanism is the excitation of non- and weakly collective one-phonon 1^- configurations which have relatively small $B(E1)$ values but are located in low-energy region. The last mechanism is the direct excitation of two-phonon configurations from the ground state. Although the direct excitation of two-phonon configurations from the ground state is a second-order effect, excitation of collective two-phonon configurations $[2_1^+ \times 3_1^-]_{1^-}$ play an essential role since the other two mechanisms yield much weaker $E1$ strengths. In this case, interference effects between the first and the third mechanisms are also important [94].

The second term of Eq. (260), although very weak as compared to the first one, may also play some role at the excitation energies above 20 MeV where the density two-phonon configurations is

a few orders of magnitude higher as compared to the density of one-phonon configurations. It will be discussed below.

Considering the two-step mechanism of the DGDR excitation in second-order perturbation theory we also need the reduced matrix element of the electromagnetic excitation of the two-phonon DGDR state $[1_i^- \times 1_{i'}^-]_J$ from the one-phonon GDR state 1_i^- . In ideal boson approximation this matrix element

$$\langle [1_i^- \times 1_{i'}^-]_J || \mathcal{M}(E1) || 1_i^- \rangle = \sqrt{(1 + \delta_{i,i'})(2J + 1)/3} \langle 1_{i'}^- || \mathcal{M}(E1) || \text{g.s.} \rangle . \quad (261)$$

4.3. Comparison with other approaches

The properties of the double-giant resonances have been also microscopically studied with the Skyrme forces [74,96] and within the second-RPA approach [97,98].

The most close to the QPM approach is the one of the first group of papers. The main difference between these two approaches is that in calculations with the Skyrme forces the properties of the ground and $1p1h$ excited states are calculated self-consistently. As within the QPM, in calculations with the Skyrme forces the $1p1h$ basis is mapped into the phonon space. Multi-phonon states are obtained by folding of one-phonon states. The phonon basis in Refs. [74,96] is restricted by only a few, the most collective, phonons for each multipolarity. Calculations are performed with the wave function including one- and two-phonon terms. The main attention is paid to the effects of anharmonicity and non-linearity. The latter is an influence of taking into account the boson-forbidden transition matrix elements, Eqs. (258), (259), on the absolute value of the DGDR excitation in heavy ion collisions.

In the second-RPA approach [99] the wave function of excited states is written as a mixture of $1p-1h$ and $2p-2h$ configurations:

$$Q_v^+ | \rangle_{\text{g.s.}} = \sum_{ph} (X_{ph}^v a_p^+ a_h - Y_{ph}^v a_h^+ a_p) + \sum_{pp'hh'} (X_{pp'hh'}^v a_p^+ a_{p'}^+ a_h a_h - Y_{pp'hh'}^v a_h^+ a_{h'}^+ a_{p'} a_p) | \rangle_{\text{g.s.}} . \quad (262)$$

The operators Q_v^+ are assumed as bosons and the energy spectrum and coefficients X and Y are obtained by diagonalization of the model Hamiltonian in the space of states described by the wave functions of Eq. (262).

5. Physical properties of the double-giant resonances

In the present section we will consider the properties of the DGDR as predicted by the QPM mainly in ^{136}Xe and ^{208}Pb for which experimental data in relativistic heavy ion collision (RHIC) are available. Before proceeding with that let us briefly check an accuracy of the description of the properties of low-lying states and single-giant resonances within this approach. It provides an estimate how good the phonon basis, to be used in the forthcoming calculation of the DGDR properties, is since no extra free parameters are used after this basis is fixed. The results of our calculations of the position and exhaust of the energy weighted sum rule (EWSR) of low-lying states and giant resonances as well as the width of resonances in ^{136}Xe and ^{208}Pb are presented in Table 10 in comparison with the experimental findings. The comparison indicate a rather good

Table 10

Integral characteristics (position, E_x , exhaust of the energy weighted sum rule (EWSR) and width of resonances, Γ) of low-lying excited states and one-phonon giant resonances in ^{136}Xe and ^{208}Pb

| Nucl. | λ^π | Calculation | | | Experiment | | |
|-------------------|-------------------|----------------|-------------------|-------------|-------------------|-------------------|-----------------|
| | | E_x (MeV) | Γ (MeV) | EWSR (%) | E_x (MeV) | Γ (MeV) | EWSR (%) |
| ^{136}Xe | 2_1^+ | 1.4 | | 2.6 | 1.31 | | 2.4 |
| | 3_1^- | 3.3 | | 5.6 | 3.28 | | 5.2 |
| | GDR _{iv} | 15.1 | 4.0 | 107 | 15.2 ^a | 4.8 ^a | 80–120 |
| | GQR _{is} | 12.5 | 3.2 | 75 | 12.3 ^b | 4.0 ^b | 70 ^b |
| | GQR _{iv} | 23.1 | 3.6 | 80 | 22.1 ± 0.7 | ≤ 5.4 | 93 ± 45 |
| ^{208}Pb | 2_1^+ | 4.2 | | 16.4 | 4.09 | | 16.9 |
| | 3_1^- | 2.4 | | 21.3 | 2.61 | | 20 |
| | GDR _{iv} | 13.35 | 3.5 | 94 | 13.4 | 4.0 | 89–122 |
| | GQR _{is} | 10.6 | 3.1 | 67 | 10.5–10.9 | 2.4–3.0 | 60–80 |
| | GQR _{iv} | 21.9 | 5.0 | 81 | 22.6 ± 0.4 | 6 ± 2 | ≈ 50 |

^aInterpolation of experimental data [56].

^bInterpolation of experimental data [5].

correspondence between calculated characteristics and experimental data. The calculation somewhat underestimate the width of resonances, especially of the isovector GQR. The main reason is related to the necessity of truncating of complex configurations included in the wave function of excited states in actual calculation. The density of multi-phonon configurations is rapidly increasing with the excitation energy. That is why the effect of the basis truncation the most strongly influences on the width of the GQR_{iv} located at higher energies.

5.1. One-step excitation of two-phonon states in the energy region of giant resonances

Let us consider a direct photoexcitation of the two-phonon states in the energy region of giant resonances from the ground state of even–even nuclei (see, Refs. [57,100] for more details). Since in RHIC experiments the Coulomb mechanism of excitation plays the most essential role, the cross sections of photoexcitation can be easily recalculated into RHIC cross sections for different energies and Z -values of target and projectile nuclei. In calculation of the $B(E\lambda)$ values we use only the terms proportional to $\psi\varphi$ (see Eq. (258)). The complete set of diagrams corresponding to a direct transition to two-phonon states from the ground state is presented in Ref. [101]. As one can see from the analytical expressions the main part of the contributions from different terms disappears due to the cancellation between particles and holes.

The cross sections of the direct photoexcitation of the groups of two-phonon states made of phonons of definite multiplicities in ^{136}Xe and ^{208}Pb are presented in Fig. 28. $E2$ -excitation of $[1^- \otimes 1^-]_{2^+}$ states is plotted in the top part of the figure. $E1$ -excitation of the two-phonon states $[1^- \otimes 2^+]_{1^-}$ and $[2^+ \otimes 3^-]_{1^-}$ is shown in the middle and the bottom parts, respectively. The

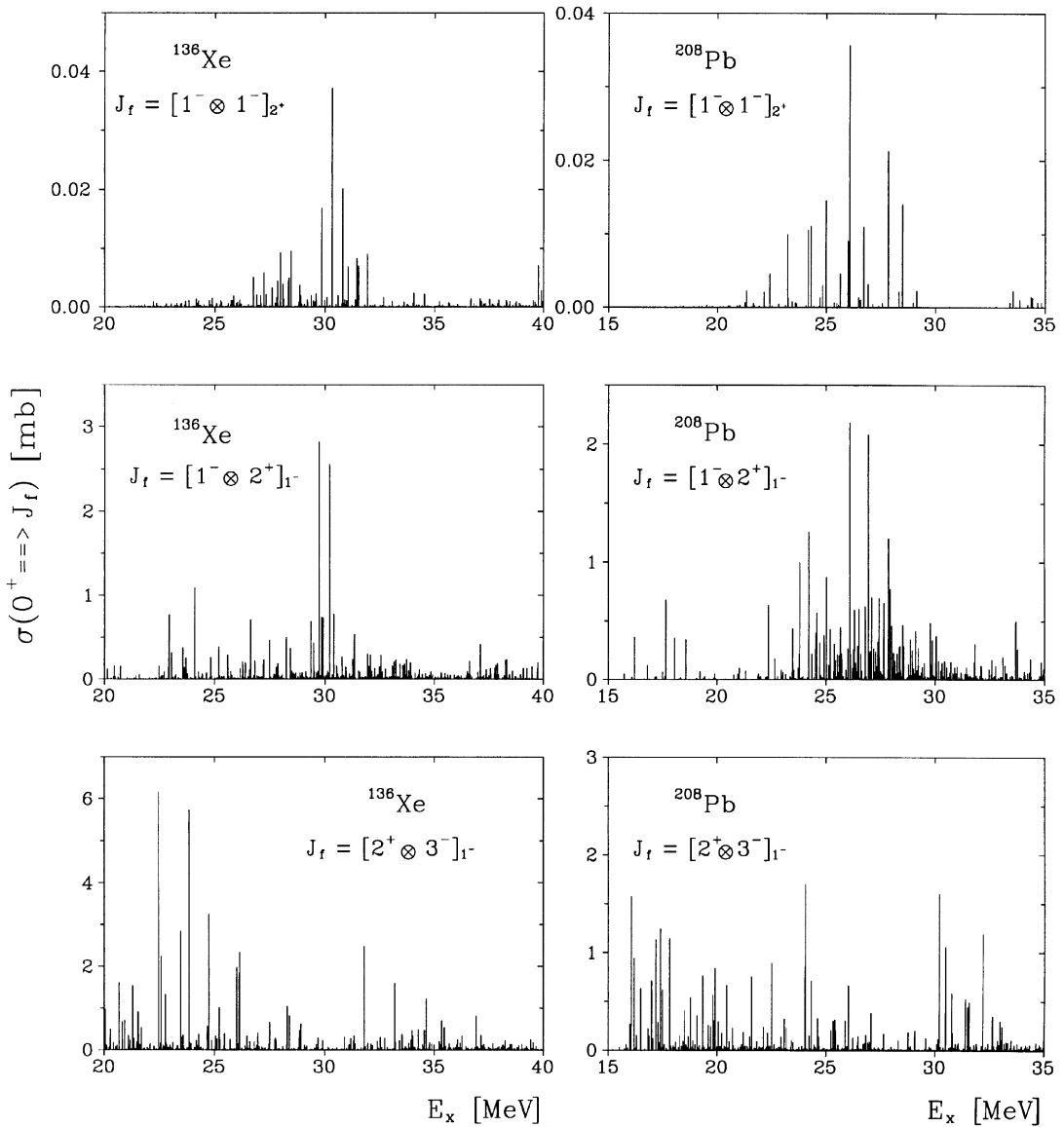


Fig. 28. Cross sections of the direct photoexcitation of two-phonon configurations $[1^- \otimes 1^-]_{2^+}$, $[1^- \otimes 2^+]_{1^-}$ and $[2^+ \otimes 3^-]_{1^-}$ from the ground state in ^{136}Xe and ^{208}Pb .

integral characteristics of two-phonon states which are a single giant resonances built on top of either a low-lying state or another single resonance in the same nuclei are given in Table 11.

The main feature of the top part of Fig. 28 is that just all two-phonon states which form this double-phonon resonance are constructed of the one-phonon 1_i^- states belonging to the GDR in the one-phonon approximation. The structure of the $[1^- \otimes 2^+]_{1^-}$ and $[2^+ \otimes 3^-]_{1^-}$ states is more

Table 11

Integral characteristics (energy centroid, width and cross section of direct photoexcitation from the ground state) of some groups of two-phonon states which are a giant resonance built on top of either a low-lying state or another single-giant resonance in ^{136}Xe and ^{208}Pb

| Nucl. | Configuration | Centroid (MeV) | Width (MeV) | σ_γ (mb) |
|-------------------|---|----------------|-------------|----------------------|
| ^{136}Xe | $[1_{\text{GDR}_i}^- \otimes 2_{\text{GQR}_{is}}^+]_{1^-}$ | 24.0 | 2.9 | 4.3 |
| | $[1_{\text{GDR}_i}^- \otimes 1_{\text{GDR}_{iv}}^+]_{2^+}$ | 30.2 | 4.0 | 0.33 |
| | $[2_{\text{GQR}_{is}}^+ \otimes 2_{\text{GQR}_{iv}}^+]_{2^+}$ | 21.3 | 0.5 | 0.1 |
| ^{208}Pb | $[1_{\text{GDR}_i}^- \otimes 2_1^+]_{1^-}$ | 17.4 | 2.2 | 1.7 |
| | $[1_{\text{GDR}_i}^- \otimes 2_1^+]_{2^-}$ | 17.2 | 2.1 | 8.7×10^{-4} |
| | $[1_{\text{GDR}_i}^- \otimes 2_1^+]_{3^-}$ | 17.7 | 3.4 | 4.9×10^{-5} |
| | $[1_{\text{GDR}_i}^- \otimes 3_1^-]_{2^+}$ | 15.3 | 3.9 | 5.2×10^{-2} |
| | $[1_{\text{GDR}_i}^- \otimes 2_{\text{GQR}_{is}}^+]_{1^-}$ | 25.1 | 3.8 | 9.6 |
| | $[1_{\text{GDR}_i}^- \otimes 1_{\text{GDR}_{iv}}^+]_{2^+}$ | 25.5 | 4.4 | 0.22 |

complex. For example, among $[1^- \otimes 2^+]_{1^-}$ states the substructure in the energy range from 15 to 20 MeV in ^{208}Pb (right middle part of Fig. 28) is formed mainly by 1_i^- phonons from the GDR region coupled to the 2_1^+ state. The small substructure above 32 MeV is due to the GDR 1_i^- phonons coupled to the 2_i^+ phonons of the isovector GQR. As for the broad structure between 20 and 30 MeV not only $[\text{GDR} \otimes \text{GQR}_{is}]_{1^-}$ states but many other two-phonon states built of less collective 1_i^- and 2_i^+ phonons, the role of which is marginal for properties of single resonances, play an essential role. The same conclusions are valid for the direct photoexcitation of $[1^- \otimes 2^+]_{1^-}$ states in ^{136}Xe . The cross section of the direct photoexcitation of the two-phonon 1^- states built of phonons of the higher multiplicities yield non-resonance feature. It is already seen for the case of $[2^+ \otimes 3^-]_{1^-}$ states (bottom part of Fig. 28), especially in ^{208}Pb .

While dealing with electromagnetic, or with Coulomb excitation from a 0^+ ground state, the priority attention has to be paid to the final states with the total angular momentum and parity $J^\pi = 1^-$. For that we have calculated the cross section for the photoexcitation of two-phonon states $[\lambda_1^{\pi_1} \otimes \lambda_2^{\pi_2}]_{1^-}$, where $\lambda_1^{\pi_1}$ and $\lambda_2^{\pi_2}$ are both natural λ^{π^n} ($\pi^n = (-1)^\lambda$) and unnatural λ^{π^n} ($\pi^n = (-1)^{\lambda+1}$) parity phonons with multipolarity λ from 0 to 9.

The results of the calculation for ^{136}Xe and ^{208}Pb integrated over the energy interval from 20 to 35 MeV are presented in Table 12. Each configuration $[\lambda_1^{\pi_1} \otimes \lambda_2^{\pi_2}]$ in the table means a sum over a plenty of two-phonon states made of phonons with a given spin and parity $\lambda_1^{\pi_1}$, $\lambda_2^{\pi_2}$, but different RPA root numbers i_1 , i_2 of its constituents

$$\sigma([\lambda_1^{\pi_1} \otimes \lambda_2^{\pi_2}]) = \sum_{i_1, i_2} \sigma([\lambda_1^{\pi_1}(i_1) \otimes \lambda_2^{\pi_2}(i_2)]) . \quad (263)$$

The total number of two-phonon 1^- states included in this calculation for each nucleus is about 10^5 and they exhaust 25% and 15% of the EWSR in ^{136}Xe and ^{208}Pb , respectively. The absolute

Table 12

Cross sections for the direct photoexcitation of different two-phonon configurations from the ground state integrated over the energy interval from 20 to 35 MeV in ^{136}Xe and ^{208}Pb . The GDR cross section integrated over the energy of its location is presented in the last line for a comparison

| Configuration | σ_γ (mb) | |
|---|----------------------|-------------------|
| | ^{136}Xe | ^{208}Pb |
| $[0^+ \otimes 1^-]_{1^-}$ | 4.4 | 3.9 |
| $[1^- \otimes 2^+]_{1^-}$ | 36.6 | 44.8 |
| $[2^+ \otimes 3^-]_{1^-}$ | 82.8 | 33.1 |
| $[3^- \otimes 4^+]_{1^-}$ | 101.0 | 56.7 |
| $[4^+ \otimes 5^-]_{1^-}$ | 68.9 | 37.3 |
| $[5^- \otimes 6^+]_{1^-}$ | 49.2 | 46.2 |
| $[6^+ \otimes 7^-]_{1^-}$ | 31.9 | 49.8 |
| $[7^- \otimes 8^+]_{1^-}$ | 13.6 | 12.5 |
| $[8^+ \otimes 9^-]_{1^-}$ | 4.9 | 9.0 |
| $\sum_{\lambda_1, \lambda_2=1}^9 [\lambda_1^{\pi_1} \otimes \lambda_2^{\pi_2}]_{1^-}$ | 71.4 | 58.5 |
| $\sum_{\lambda_1, \lambda_2=1}^9 [\lambda_1^{\pi_1} \otimes \lambda_2^{\pi_2}]_{1^-}$ | 46.7 | 71.1 |
| $\sum_{\lambda_1, \lambda_2=0}^9 [\lambda_1^{\pi_1''} \otimes \lambda_2^{\pi_2''}]_{1^-}$ | 511.4 | 422.9 |
| $[\text{GDR} \otimes \text{GDR}]_{2^+}$ | 0.33 | 0.22 |
| $\sum_{\lambda_1, \lambda_2=1}^9 [\lambda_1^{\pi_1} \otimes \lambda_2^{\pi_2}]_{2^+}$ | 38.1 | 21.7 |
| GDR | 2006 | 2790 |

value of the photoexcitation of any two-phonon state under consideration is negligibly small but altogether they produce a sizable cross section. Table 12 demonstrates that different two-phonon configurations give comparable contributions to the total cross section which decreases only for very high spins because of the lower densities of such states. As a rule, unnatural parity phonons play a less important role than natural parity ones. For these reasons we presented in the table only the sums for [natural \otimes unnatural] and [unnatural \otimes unnatural] two-phonon configurations.

The cross section for the photoexcitation of all two-phonon 1^- states in the energy region 20–35 MeV from the ground state equals in our calculation to 511 and 423 mb for ^{136}Xe and ^{208}Pb , respectively. It is not surprising that we got a larger value for ^{136}Xe than for ^{208}Pb . This is because the phonon states in Xe are composed of a larger number of two-quasiparticle configurations due to the pairing. The same values for two-phonon states with angular momentum and parity $J^\pi = 2^+$ are an order of magnitude smaller. We point out that the direct excitation of $[1^- \otimes 1^-]_{2^+}$ or $[\text{GDR} \otimes \text{GDR}]_{2^+}$ configurations is negligibly weak (compare results in Tables 11 and 12). The calculated values should be compared to the cross section for the photoexcitation of the single-phonon GDR which in our calculation equals to 2006 and 2790 mb, respectively.

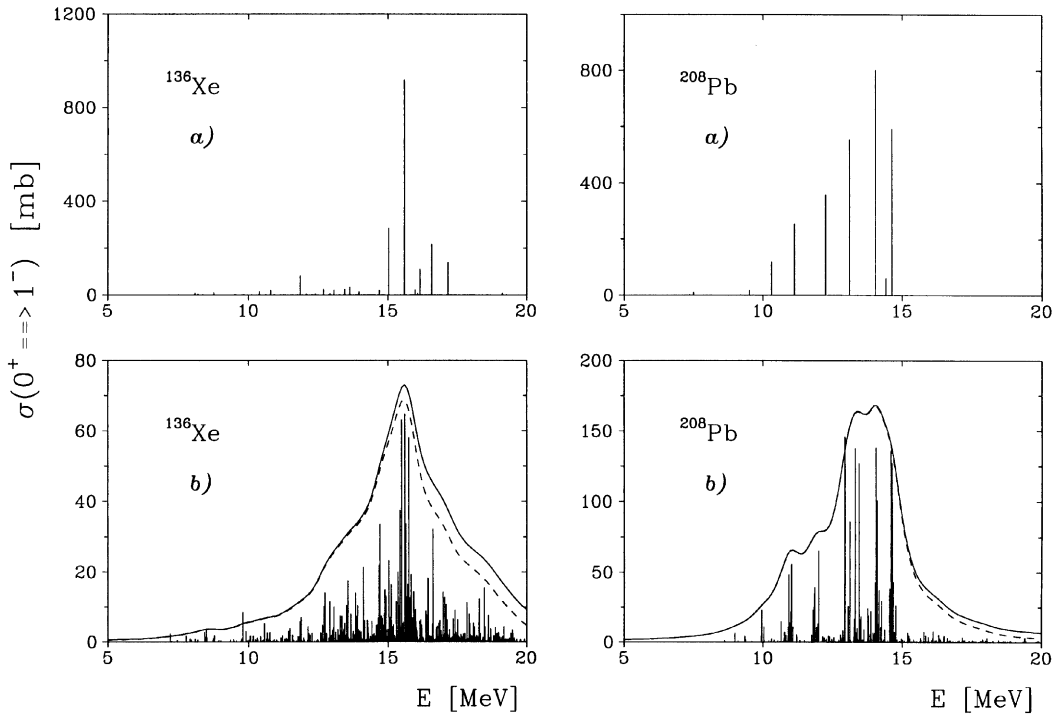


Fig. 29. Photoexcitation cross section of the GDR in ^{136}Xe and ^{208}Pb . Calculations are performed: (a) within one-phonon approximation and (b) with taking into account of the coupling between one- and two-phonon configurations. Continuous curves in the bottom part are the strength functions calculated with a smearing parameter $\Delta = 1$ MeV; dashed curve corresponds to electromagnetic transitions to one-phonon 1^- states, solid curve – to one- and two-phonon 1^- states.

A contribution of two-phonon 1^- states to the total cross section at GDR energies is weaker than at higher energies because of the lower density of two-phonon states and the lower excitation energy and can be neglected considering the GDR itself. It is clearly demonstrated in Fig. 29b. In this figure the cross sections of the photoexcitation of 1^- states in ^{136}Xe and ^{208}Pb are presented. The top part of the figure corresponds to a calculation performed in one-phonon approximation. The results of calculations with the wave function which includes a coupling between one- and two-phonon 1^- configurations are plotted in the bottom part of the figure. For a visuality the last calculations are also presented as strength functions

$$b(\sigma, E) = \frac{1}{2\pi} \sum_{\nu} \sigma_{\nu}^J \frac{\Delta}{(E - E_{\nu}^J)^2 + \Delta^2/4} \quad (264)$$

with a smearing parameter $\Delta = 1$ MeV, where σ_{ν}^J is a partial cross section for the state with the excitation energy E_{ν}^J plotted also by a vertical line. The $E1$ -transitions to one-phonon components of the wave function of excited 1^- states are plotted by dashed curve. It should be compared with

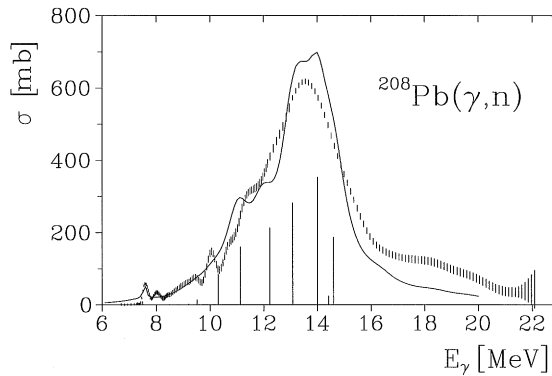


Fig. 30. Photon-neutron cross sections in ^{208}Pb . Solid curve is the result of calculation with the wave function including one- and two-phonon terms presented with a smearing parameter $\Delta = 1$ MeV; vertical lines (in arbitrary units) – within one-phonon approximation. Experimental data are plotted by experimental error bars.

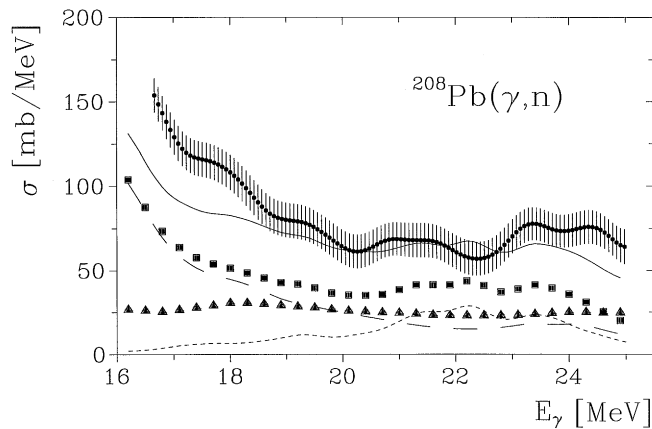


Fig. 31. Photo-neutron cross section for ^{208}Pb . Experimental data (dots with experimental errors) are from Ref. [103]. The long-dashed curve is the high energy tail of the GDR, the short-dashed curve is the GQR_{iv} and the curve with squares is their sum. The contribution of two-phonon states is plotted by a curve with triangles. The solid curve is the total calculated cross section.

the solid curve which is the sum of transitions to one- and two-phonon 1^- configurations in the GDR energy region.

For ^{208}Pb photoexcitation cross sections are known from experimental studies in (γ, n) reactions up to the excitation energy about 25 MeV [102,103]. It was shown that QPM provides a very good description of the experimental data in the GDR region [102] (see, Fig. 30), while theoretical calculations at higher excitation energies which account for contributions from the single-phonon GDR and GQR_{iv} essentially underestimated the experimental cross section [103]. The experimental cross sections above 17 MeV are shown in Fig. 31 together with theoretical predictions. The results of the calculations are presented as strength functions obtained with averaging parameter

equal to 1 MeV. The contribution to the total cross section of the GQR_{iv} (short-dashed curve), the high-energy tail of GDR (long-dashed curve), and their sum (squared curve), are taken from Ref. [103]. The curve with triangles represents the contribution of the direct excitation of the two-phonon states from our present studies. The two-phonon states form practically a flat background in the whole energy region under consideration. Summing together the photoexcitation cross sections of all one- and two-phonon states, we get a solid curve which is in a very good agreement with the experimental data.

Thus, from our investigation of photoexcitation cross sections we conclude that in this reaction very many different two-phonon states above the GDR contribute on a comparable level, forming altogether a flat physical background which should be taken into account in the description of experimental data. On the other hand, Coulomb excitation in relativistic heavy ion collisions provides a unique opportunity to excite a very selected number of two-phonon states by the absorption of two virtual γ 's in a single process of projectile–target interaction [6]. Theoretically, this process is described using the second-order perturbation theory of the semi-classical approach of Winther and Alder [6,18] and discussed in Section 3.2.3. Since excitation cross sections to second order are much weaker than to first order of the theory, two-phonon states connected to the ground states by two $E1$ -transitions are predominantly excited. These two-phonon states have the structure $[1^-(i) \otimes 1^-(i')]_{J^+}$ and form the DGDR.

5.2. 1^+ component of the DGDR

According to the rules of angular momentum coupling two one-phonon states with the spin and parity equal to 1^- may couple to the total angular momentum $J^\pi = 0^+, 1^+$ and 2^+ . Thus, in principle, three components of the DGDR with these quantum numbers should exist. In phenomenological approaches describing the single GDR as one collective state, the $[1^- \otimes 1^-]_{1^+}$ component the DGDR is forbidden by symmetry properties. Taking into account the Landau damping this collective state splits into a set of different 1_i^- states distributed over an energy interval. In microscopic studies the Landau damping is taken into account by solving the RPA equations. Again, the diagonal components $[1_i^- \otimes 1_i^-]_{1^+}$ are forbidden by the same symmetry properties but nondiagonal ones $[1_i^- \otimes 1_{i'}^-]_{1^+}$ exist and should be taken into consideration. Consequently, the role of these nondiagonal components depends on how strong is the Landau damping.

We produce here two-phonon DGDR states with quantum numbers $J^\pi = 0^+, 1^+$ and 2^+ by coupling one-phonon RPA states with the wave function $|1_i^- \rangle_m$ to each other. The index m stands for different magnetic substates. The wave function of the two-phonon states has the form

$$|[1_i^- \otimes 1_i^-]_{J^\pi=0^+,2^+} \rangle_M = \frac{1}{\sqrt{2}} \sum_{m,m'} (1m1m'|JM) |1_i^- \rangle_m |1_i^- \rangle_{m'} , \quad (265)$$

for two-phonon states made of two identical phonons while for other DGDR states it is

$$|[1_i^- \otimes 1_{i'}^-]_{J^\pi=0^+,1^+,2^+} \rangle_M = \sum_{m,m'} (1m1m'|JM) |1_i^- \rangle_m |1_{i'}^- \rangle_{m'} . \quad (266)$$

In the present calculation we do not include the interaction between DGDR states, of Eqs. (265) and (266), and we do not couple them to states with different than two number of phonons (it will

be considered below). Thus, our two-phonon states $[[1_i^- \otimes 1_{i'}^-]_{J^\pi}]_M$ have excitation energy equal to the sum of one-phonon energies $\omega_i + \omega_{i'}$ and are degenerated for different values of the total spin J^π and its projection M .

Since the main mechanism of excitation in projectile ions at relativistic energies is the Coulomb part of interaction with a target, the nuclear part of interaction has been neglected in the present analysis. In a semi-classical approach [6], the two-phonon DGDR states can be excited in second-order perturbation theory via the two-step process g.s. \rightarrow GDR \rightarrow DGDR. The second-order amplitude can be written as

$$a_{[1_i^- \otimes 1_{i'}^-], M}^{(2)} = \frac{1}{2} \sum_m a_{1_i^-, m \rightarrow [1_i^- \otimes 1_{i'}^-], M}^{(1)} a_{\text{g.s.} \rightarrow 1_i^-, m}^{(1)}, \tag{267}$$

where assuming the Coulomb mechanism of excitation the first-order amplitude $a_{J_i^- \rightarrow J_j}$ is proportional to the reduced matrix element of $\langle J_j || E1 || J_i \rangle$. The reduced matrix element $\langle [1_i^- \otimes 1_{i'}^-]_{J^\pi} || E1 || 1_i^- \rangle$ of electromagnetic excitation of two-phonon states, Eqs. (265) and (266), from the one-phonon state $|1_i^- \rangle_m$ is related, in the boson picture of nuclear excitation, to the excitation of $|1_i^- \rangle_m$ from the ground state according to (261). It should be noted that although for the two-phonon states, Eq. (265), we have an extra factor $\sqrt{2}$, the states of Eq. (266) play a more important role in two-step excitations since they can be reached by two different possibilities: g.s. $\rightarrow 1_i^- \rightarrow [1_i^- \otimes 1_{i'}^-]$ and g.s. $\rightarrow 1_{i'}^- \rightarrow [1_i^- \otimes 1_{i'}^-]$. First of all, we point out that in second-order perturbation theory the amplitude for this process is identically zero in a semi-classical approach. This can be understood by looking at Fig. 32. The time-dependent field V_{E1} carries angular momentum with projections $m = 0, \pm 1$. Thus, to reach the 1^+ DGDR magnetic substates, many routes are possible. The lines represent transitions caused by the different projections of V_{E1} : (a) dashed lines are for $m = 0$, (b) dashed-dotted lines are for $m = -1$, and (c) solid lines are for $m = +1$. The relation $V_{E1, m=0} \neq V_{E1, m=\pm 1}$ holds, so that not all routes yield the same excitation amplitude. Since the phases of the wave functions of each set of magnetic substates are equal, the difference between the transition amplitudes to a final M , can also arise from different values of the Clebsch–Gordan coefficients $(1m1m'|1M)$. It is easy to see that, for any route to a final M , the second-order amplitude will be proportional to $(001m|1m)(1m1m'|1M) V_{E1, m'} V_{E1, m} + (m \leftrightarrow m')$.

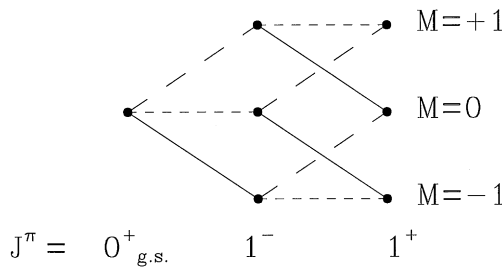


Fig. 32. The possible paths to the excitation of a given magnetic substate of the 1^+ component of the DGDR are displayed. The transitions caused by the different projections of the operator V_{E1} are shown by: (a) dashed lines for $m = 0$, (b) dashed-dotted lines for $m = -1$, and (c) solid lines are $m = +1$.

The two amplitudes carry opposite signs from the value of the Clebsch–Gordan coefficients. Since $\langle 001m|1m \rangle \equiv 1$, the identically zero result for the excitation amplitude of the 1^+ DGDR state is therefore a consequence of

$$\sum_{mm'} (1m1m'|1M) = 0. \quad (268)$$

We have also performed a coupled-channels calculation [104] following the theory described in Ref. [19]. As shown in Ref. [19], the coupling of the electric quadrupole (isovector and isoscalar) and the electric dipole states is very weak and can be neglected. We therefore include in our space only one-phonon 1^- and two-phonon $[1_i^- \otimes 1_{i'}^-]_{J^\pi}$ ($J^\pi = 0^+, 1^+$ and 2^+) states. In coupled-channels calculation we take into account interference effects in the excitation of different GDR and DGDR states and obtain the occupation amplitudes by solving the coupled-channels equations. By solving these equations we thus account for unitarity and for multi-step excitations, beyond the two-step processes of Eq. (267). The time-dependent electric dipole field is that of a straight-line moving particle with charge Ze , and impact parameter b (we use Eqs. (25) and (26) of Ref. [19]).

Due to the large number of degenerate magnetic substates, to make our coupled-channels calculation feasible, we have chosen a limited set of GDR and DGDR states. We have taken six 1^- states which have the largest value of the reduced matrix element $\langle 1_i^- || E1 || g.s. \rangle$. These six states exhaust 90.6% of the classical EWSR, while all 1^- states up to 25 MeV in our RPA calculation exhaust 94.3% of it. This value is somewhat smaller than the 122% reported in Ref. [32]. It is because the continuum in our RPA calculation was approximated by narrow quasibound states. From these six one-phonon 1^- states we construct two-phonon $[1_i^- \otimes 1_{i'}^-]_{J^\pi}$ states, Eqs. (265) and (266), which also have the largest matrix element of excitation $\langle [1_i^- \otimes 1_{i'}^-]_{J^\pi} || E1 || 1_i^- \rangle$ for excitations starting from one-phonon states.² The number of two-phonon states equals to 21 for $J^\pi = 0^+$ and 2^+ , and to 15 for $J^\pi = 1^+$. The cross section for the DGDR excitation was obtained by summing over the final magnetic substates of the square of the occupation amplitudes and, finally, by an integration over impact parameter. We have chosen the minimum impact parameter, $b = 15.54$ fm, corresponding to the parameterization of Ref. [43], appropriate for lead–lead collisions.

The electromagnetic excitation cross sections for the reaction ^{208}Pb (640A MeV) + ^{208}Pb with excitation of all our basic 63 states is shown in Fig. 33. The total cross sections for each multipolarity are presented in Table 13, together with the results of first-order (for one-phonon excitations) and second-order (for two-phonon excitations) perturbation theory. The coupled-channels calculation yields a non-zero cross section for the 1^+ DGDR state due to other possible

² As demonstrated in the previous subsection the direct excitation of two-phonon configurations from the ground state is very weak. It allows us to exclude in our calculation matrix elements of the form $\langle [1_i^- \otimes 1_{i'}^-]_{2^+(1^+)} || E2(M1) || g.s. \rangle$ which correspond to direct transitions and produce higher-order effects in comparison with accounted ones. These matrix elements give rise to DGDR excitation in first-order perturbation theory. Thus, to prove our approximation, we have calculated such cross sections and got total values equal to 0.11 and < 0.01 mb for the 21 2^+ and the 15 1^+ basic two-phonon states, respectively. These values have to be compared to 244.9 mb for the total DGDR cross section in the second-order perturbation theory.

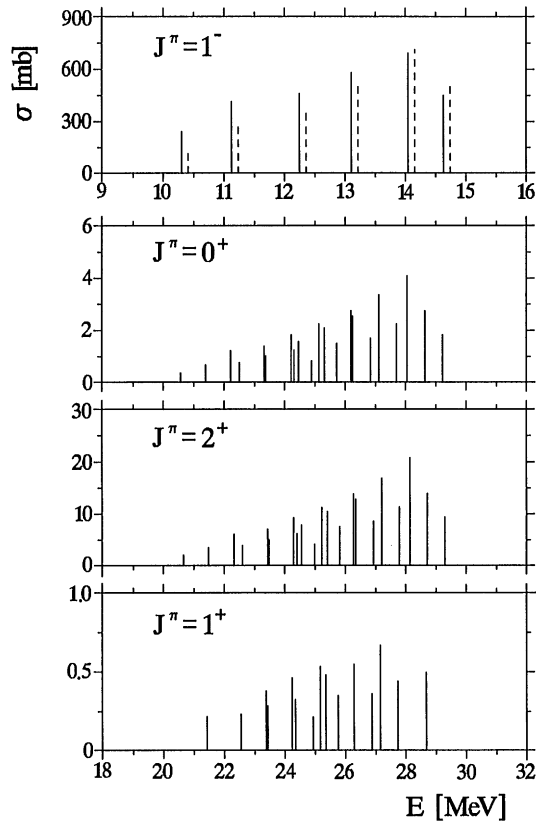


Fig. 33. The electromagnetic excitation cross sections for the reaction ^{208}Pb (640A MeV) + ^{208}Pb calculated in coupled channels. It is shown the excitation of the GDR (top) and the three components $J^\pi = 0^+$, 2^+ and 1^+ of the DGDR. The $B(E1)$ strength distribution (in arbitrary units) over 1^- states is shown by dashed lines. For a visuality it is shifted up by 100 keV.

Table 13

Cross section (in mb) for the excitation of the GDR and the three components with $J^\pi = 0^+$, 2^+ , 1^+ of the DGDR in ^{208}Pb (640A MeV) + ^{208}Pb collisions. Calculations are performed within coupled-channels (CC) and within first (PT-1) and second (PT-2) order perturbation theory, respectively

| | CC | PT-1 | PT-2 |
|---------------|-------|--------|-------|
| GDR | 2830. | 3275. | 0. |
| DGDR $_{0^+}$ | 33.0 | 0.0 | 43.1 |
| DGDR $_{2^+}$ | 163.0 | 0.11 | 201.8 |
| DGDR $_{1^+}$ | 6.3 | < 0.01 | 0.0 |
| DGDR/GDR | 0.071 | 0.075 | |

routes (higher-order), not included in second-order perturbation theory. One observes a considerable reduction of the DGDR cross sections, as compared to the predictions of the second-order perturbation theory. The GDR cross sections are also reduced in magnitude. However, the population of the 1^+ DGDR states are not appreciable and cannot be the source of the missing excitation cross section needed to explain the experiments. In general, the coupled-channels calculation practically does not change the relative contribution of different one-phonon 1_i^- and two-phonon states $[1_i^- \otimes 1_{i'}^-]_{J^\pi}$ to the total cross section with given $J^\pi = 1^-, 0^+$ and 2^+ . But since the 1^+ component of the DGDR, with its zero value of excitation cross section in second-order perturbation theory, has a special place among the two other components, the main effect of coupled-channels is to redistribute the total cross section between the $J^\pi = 0^+, 2^+$ and $J^\pi = 1^+$ components.

The calculated cross section in coupled channels for both GDR and DGDR are somewhat lower than that reported in experimental findings [54,105]. This is not surprising since as mentioned above our chosen six 1^- states exhaust only 90.6% of EWSR while the photo-neutron data [32] indicate that this value equals to 122%. Due to this underestimate of exhaust of the EWSR the cross section for the DGDR excitation reduces more strongly than the one for the single GDR. This is because the GDR cross section is roughly proportional to the total $B(E1)$ value while for the DGDR it is proportional to the square of it. We will return back in more detail to the problem of absolute cross sections of the DGDR excitation in RHIC in the forthcoming subsection.

5.3. Position, width and cross section of excitation in RHIC of the DGDR in ^{136}Xe and ^{208}Pb

To describe the width of two-phonon resonances it is necessary to take into account a coupling of two-phonon configurations, which form these resonances, with more complex ones. For this two types of calculations have been performed. In the first of them [106] the fine structure of the GDR calculated with the wave function which includes one- and two-phonon configurations and presented in Fig. 29b has been used. The DGDR states have been constructed as a product of the GDR to itself. In other words, following the Axel–Brink hypotheses on top of each 1^- state in Fig. 29b we have built the full set of the same 1^- states.

The calculation has been performed for the nucleus ^{136}Xe . In the dipole case, $\lambda^\pi = 1^-$, the one-phonon states exhaust 107% of the classical oscillator strength and are displayed in the left part of Fig. 29a. Of these, 20 states have an oscillator strength which is at least 1% of the strongest strength and together exhaust 104% of the classical EWSR. We have used these states in the coupling to two-phonon states. We have included all the natural parity phonons $\lambda^\pi = 1^- - 8^+$ with energy lower or equal to 21 MeV, obtaining 2632 two-phonon configurations. One obtains 1614 states described by the wave function which includes one- and two-phonon configurations, in the energy interval from 7 MeV to 19.5 MeV. Their photoexcitation cross sections are shown in Fig. 29b. The $B(E1)$ value associated with each mixed state is calculated through its admixture with one-phonon states, as $|\langle \nu || \mathcal{M}(E1) || 0 \rangle|^2 = |\sum_i S_i^\nu(1^-) \langle 0 || Q_{1^- i} \mathcal{M}(E1) || 0 \rangle|^2$. Also shown by dashed curve in the left part of Fig. 29b is the result obtained adding an averaging parameter of 1.0 MeV. This parameter represents in some average way the coupling to increasingly more complicated states and eventually to the compound nuclear states. From the resulting smooth response it is easy to directly extract the centroid and the full width at half maximum of the GDR. The corresponding

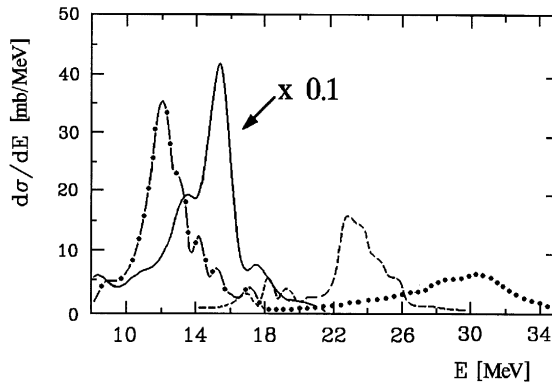


Fig. 34. The cross section for Coulomb excitation of the one-phonon GDR (continuous curve), of the isoscalar GQR (dash-dotted), of the isovector GQR (long dashed) as well as for the double-phonon GDR (short dashed) are shown. They have been calculated at $E_{\text{lab}} = 681A$ MeV, taking into account the energy reduction of the beam in the target [40]. The one-phonon GDR cross section has been reduced in the figure by a factor 10.

Table 14

Calculated (for two values of r_o) and experimental cross section (in mb) for the excitation of giant resonances in ^{136}Xe in ^{136}Xe (690A MeV) + ^{208}Pb reaction. In the last row, the experimental cross sections for Coulomb excitation of one- and two-phonon states from Ref. [40] are shown. The value of the integrated cross section reported in Ref. [40] is 1.85 ± 0.1 b. The nuclear contribution has been estimated in Ref. [40] to be about 100 mb, while about 3% (50 mb) of the cross section is found at higher energy. Subtracting these two contributions and the two-phonon cross section, leads to the value 1485 ± 100 mb shown in the table

| | GDR | GQR _{is} | GQR _{iv} | GDR + GQR | DGDR |
|----------------|----------------|-------------------|-------------------|----------------|--------------|
| $r_o = 1,2$ fm | 2180 | 170 | 120 | 2470 | 130 |
| $r_o = 1,5$ fm | 1480 | 110 | 60 | 1650 | 50 |
| Experiment | 1024 ± 100 | – | – | 1485 ± 100 | 215 ± 50 |

values are $E_{\text{GDR}} = 15.1$ MeV and $\Gamma_{\text{GDR}} = 4$ MeV. They can be compared with the values extracted from experiment, $E_{\text{GDR}} = 15.2$ MeV and $\Gamma_{\text{GDR}} = 4.8$ MeV.

The isoscalar and the isovector giant quadrupole resonances (GQR) have also been calculated. The centroid, width and percentage of the EWSR associated with the isoscalar mode are 12.5 MeV, 3.2 MeV and 75%, respectively. The corresponding quantities associated with the isovector GQR are 23.1 MeV, 3.6 MeV and 80%.

The differential Coulomb-excitation cross sections as a function of the energy associated with the one-phonon GDR and GQR resonances and the two-phonon DGDR in ^{136}Xe (690A MeV) + ^{208}Pb reaction are displayed in Fig. 34. It is seen that the centroid of the two-phonon dipole excitation falls at 30.6 MeV, about twice that of the one-phonon states, while the width is $\Gamma \approx 6$ MeV, the ratio to that of the one-phonon excitation being 1.5.

The associated integrated values are displayed in Table 14, in comparison with the experimental findings. The cross sections depend strongly on the choice of the value of $b_{\text{min}} = r_o(A_p^{1/3} + A_t^{1/3})$.

In keeping with the standard “safe distance”, that is, the distance beyond which nuclear excitation can be safely neglected, we have used $r_o = 1.5$ fm. Because their values essentially do not depend on the width of the GDR, we view the calculated cross section of 1650 mb as a rather accurate value and if anything an upper limit for the one-phonon Coulomb excitation cross section. It is satisfactory that the measured cross section is rather close to this value. Also shown in Table 14 are the predictions associated with the sequential excitation of the DGDR. This result is essentially not modified evaluating the direct Coulomb excitation of the double GDR. In fact, the cross section associated with this process is a factor 10^{-3} smaller than that associated with the two-step process. The calculated value of 50 mb is a factor of 0.25 smaller than that observed experimentally.

Two other processes are possible within the sequential excitation of the giant modes which can lead to an excitation energy similar to that of the two-phonon GDR. They are the excitation of the isoscalar GQR mode followed by a GDR mode and vice versa. The resulting cross section is estimated to be an order of magnitude smaller, cf. Table 14, and does not change qualitatively this result. In order to make clearer the seriousness of this discrepancy, we have recalculated all the cross sections using $r_o = 1.2$ fm, namely with a much smaller radius than that prescribed in order to respect the safe Coulomb excitation distance of closest approach. The calculated value of 130 mb is still a factor of 0.6 smaller than the reported experimental cross section. At the same time the cross section of the one-phonon states has become a factor 1.7 larger than the empirical value. This factor becomes 1.5 when the coupling to higher multiphonon states is included according to the standard Poisson distribution for the excitation probabilities [17].

The main shortcoming of the above discussed theoretical scheme to treat the DGDR, when the DGDR states are obtained by folding of the fine structure of two GDRs, is the fact that the DGDR states obtained this way are not eigenstates of the used microscopic Hamiltonian. To overcome this shortcoming other calculations have been performed in which two-phonon [$1^- \otimes 1^-$] DGDR states are coupled directly to more complex ones [107–109]. From rather general arguments [60], the most important couplings leading to real transitions of the double-giant resonances and thus to a damping width of these modes are to configurations built out by promoting three nucleon across the Fermi surface. That is, configurations containing three holes in the Fermi sea and three particles above the Fermi surface ($3p3h$ configurations). We use the wave function (238) to describe the DGDR states and their coupling to $1p1h$ and to $3p3h$ doorway configurations.

The spectrum of excited states which form the DGDR is obtained by solving the secular equation (253) and the wave function coefficient S, D and T are calculated from Eq. (254). Pauli principle corrections, the coefficients $\tilde{K}_J(\beta_2\alpha_2|\alpha'_2\beta'_2)$ and anharmonicity shifts $\Delta\omega_{\alpha_2\beta_2}^J$, were omitted in calculations presented in Ref. [107] and accounted for in Ref. [108]. While they are small, they produce shifts in the energy centroid of the double-giant resonance. Similar coefficients appear also in connection with the term arising from the “doorway states” containing three phonons in Eq. (238). We have neglected them because they again are small and furthermore act only in higher order as compared to the previous term, in defining the properties of the double-giant dipole resonance. Finally, the corresponding \tilde{K} -coefficient associated with the first term in Eq. (238) is proportional to the number of quasiparticles present in the ground state of the system, a quantity which is assumed to be zero within linear response theory.

In keeping with the fact that the Q -value dependence of the Coulomb excitation amplitude is rather weak at relativistic energies [14], the cross section associated with the two-step excitation of the double-giant dipole resonance is proportional to

$$\begin{aligned}
 [B(E1) \times B(E1)] &= \left| \sum_{\nu_1} \langle \Psi_{0^+(2^+)}^{\nu_1} | \mathcal{M}(E1) | \Psi_1^{\nu_1} \rangle \cdot \langle \Psi_1^{\nu_1} | \mathcal{M}(E1) | \Psi_{g.s.} \rangle \right|^2 \\
 &= \left| 2 \sum_{\alpha_2 \beta_2} D_{\alpha_2 \beta_2}^{\nu} (J) \cdot \left[\frac{M_{\alpha_2} M_{\beta_2}}{\sqrt{1 + \delta_{\alpha_2, \beta_2}}} + \sum_{\alpha'_2 \beta'_2} M_{\alpha'_2} M_{\beta'_2} \sqrt{1 + \delta_{\alpha'_2, \beta'_2}} \tilde{K}_J(\beta_2 \alpha_2 | \alpha'_2 \beta'_2) \right] \right|^2,
 \end{aligned} \tag{269}$$

where $M_\alpha = \langle Q_\alpha | \mathcal{M}(E1) | 0_{g.s.}^+ \rangle$ is the reduced matrix element of the $E1$ -operator which acting on the ground state $| \rangle_{ph}$ excites the one-phonon state with quantum numbers $\alpha = (1^-, i)$.

Making use of the elements discussed above we calculated the distribution of the quantity Eq. (269) over the states Eq. (238) in ^{136}Xe . We considered only $J^\pi = 0^+$ and 2^+ components of the two-phonon giant dipole resonance. As already discussed above its $J^\pi = 1^+$ component cannot be excited in the second-order perturbation theory and is sufficiently quenched in coupled-channels calculation. The 15 configurations $\{1^-, 1^-i\} = \{\alpha_2, \beta_2\}$ displaying the largest $[B(E1) \times B(E1)]$ values were used in the calculation. They are built up out of the five most collective RPA roots associated with the one-phonon giant dipole resonance carrying the largest $B(E1)$ values and exhausting 77% of energy weighted sum rule (EWSR). Two-phonon states of collective character and with quantum numbers different from 1^- lie, as a rule, at energies few MeV away from the double-giant dipole states and were not included in the calculations. The three-phonon states $\{\alpha_3 \beta_3 \gamma_3\}$ were built out of phonons with angular momentum and parity $1^-, 2^+, 3^-$ and 4^+ . Only those configurations where either α_3, β_3 or γ_3 were equal to α_2 or β_2 were chosen. This is because other configurations lead to matrix elements $U_{\alpha_3 \beta_3 \gamma_3}^{\alpha_2 \beta_2} (J)$ of the interaction, which are orders of magnitude smaller than those associated with the above-mentioned three-phonon configurations, and which contain in the present calculation 5742 states up to an excitation energy 38 MeV. The single-particle continuum has been approximated in the present calculation by quasibound states. This approximation provides rather good description of the single GDR properties in ^{136}Xe . This means that our $(2p2h)_{[1^- \times 1^-]}$ spectrum is also rather complete for the description of the DGDR properties although it is located at higher energies.

If one assumes a pure boson picture to describe the phonons, without taking into account their fermion structure, the three-phonon configurations omitted in the present calculation do not couple to two-phonon states under consideration. Furthermore, although the density of $3p3h$ configurations is quite high in the energy region corresponding to the DGDR, a selection of the important doorway configurations in terms of the efficiency with which configurations couple to the DGDR, can be done rather easily. The above considerations testify to the advantage of employing a microscopic phonon picture in describing the nuclear excitation spectrum, instead of a particle-hole representation. One can more readily identify the regularities typical of the collective picture of the vibrational spectrum, and still deal with the fermion structure of these excitations. As far as the one-phonon term appearing in Eq. (238) is concerned, essentially all phonons with angular momentum and parity 0^+ and 2^+ were taken into account within the energy interval 20–40 MeV.

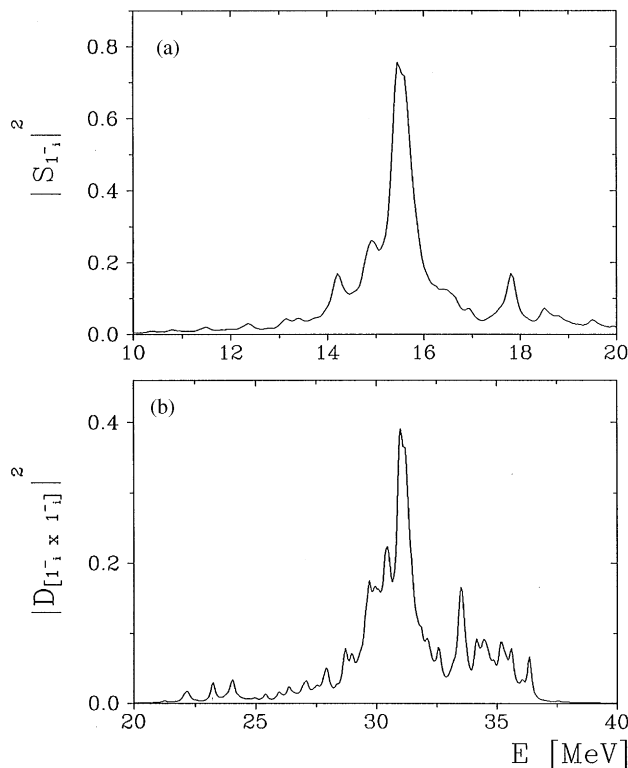


Fig. 35. Fragmentation of the most collective (a) one-phonon 1^- and (b) two-phonon $[1^- \otimes 1^-]$ configurations in ^{136}Xe due to the coupling to more complex configurations. The results are presented with a smearing parameter $\Delta = 0.2$ MeV.

A rather general feature displayed by the results of the present calculation is that all two-phonon configurations of the type $\{1^-i, 1^-i'\}$ building the DGDR in the “harmonic” picture are fragmented over a few MeV due to the coupling to $3p3h$ “doorway states”. Fragmentation of the most collective one is presented in the bottom part of Fig. 35. For a comparison the fragmentation of the most collective one-phonon 1^- configuration due to the coupling to $2p2h$ “doorway states” is plotted in the top part of the same figure. The results have been averaged with the aid of a Breit–Wigner distribution of width 0.2 MeV. The maximum amplitude with which each two-phonon configuration enters in the wave function (238) does not exceed a few percent. Two-phonon configurations made out of two different 1^- phonons are fragmented stronger than two-phonon configurations made out of two identical 1^- phonons. This is keeping with the fact that, as a rule, states of the type $\{1^-i, 1^-i'\}$ with $i \neq i'$ are less harmonic than states with $i = i'$ and consequently are coupled to a larger number of three-phonon configurations.

In Figs. 36b and c, the $[B(E1) \times B(E1)]$ quantity of Eq. (269) associated with Coulomb excitation of the almost degenerate $J^\pi = 0^+$ and $J^\pi = 2^+$ components of double-giant dipole resonance are shown. For comparison, the $B(E1)$ quantity associated with the Coulomb excitation of the one-phonon giant dipole resonance is also shown in Fig. 36a. The reason why the two angular momentum components of the DGDR are almost degenerate can be traced back to the fact that

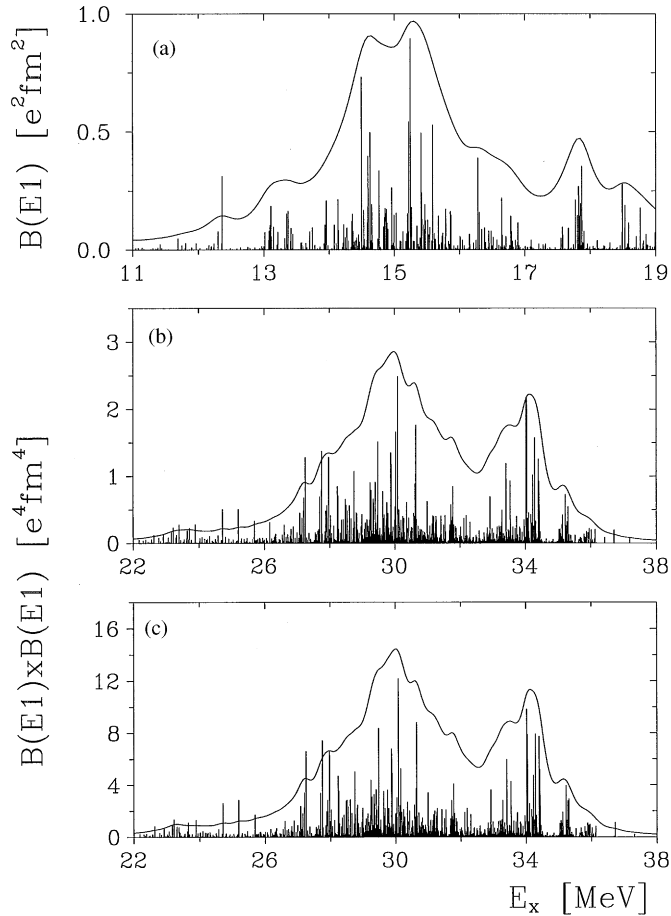


Fig. 36. (a) $B(E1)$ values for the GDR and (b, c) $[B(E1) \times B(E1)]$ values Eq. (269) for the DGDR associated with Coulomb excitation in ^{136}Xe in relativistic heavy ion collision. (b) and (c) correspond to $J = 0^+$ and $J = 2^+$ components of the DGDR, respectively. A smooth curve is a result of averaging over all states with a smearing parameter $\Delta = 0.5$ MeV. See text for details.

the density of one-phonon configurations to which the DGDR couple and which are different for $J^\pi = 0^+$ and $J^\pi = 2^+$ type states is much lower than the density of states associated with $3p3h$ “doorway states”, density of states which is the same in the present calculation for the two different angular momentum and parity. Effects associated with the J -dependence of the \tilde{K}_J and Δ_J coefficients are not able to remove the mentioned degeneracy, because of the small size of these coefficients. These coefficients can also affect the excitation probability with which the $J^\pi = 0^+$ and $J^\pi = 2^+$ states are excited (cf. Eq. (269)). The effect however is rather small, leading to a decrease of the order of 2–3% in both cases. The J -degeneracy would be probably somehow broken if one goes beyond a one-boson exchange picture in the present approach of interaction between different nuclear modes. The next order term of interaction would couple the DGDR states to many other $3p3h$ configurations, not included in the present studies, some of these $3p3h$ configurations would

Table 15

Position, width and the ratio values R , Eq. (270), for of $J = 0^+$ and $J = 2^+$ components of the DGDR with respect to the ones of the single GDR in ^{136}Xe . The third row corresponds to pure harmonic picture

| J | $\langle E_{\text{DGDR}} \rangle - 2 \cdot \langle E_{\text{GDR}} \rangle$ (keV) | $\Gamma_{\text{DGDR}}/\Gamma_{\text{GDR}}$ | R |
|-------|--|--|------|
| 0^+ | - 120 | 1.44 | 1.94 |
| 2^+ | - 90 | 1.45 | 1.96 |
| | 0 | $\sqrt{2}$ | 2 |

be different for different J^π values. Unfortunately, such calculation is not possible at the present moment.

The calculated excitation functions displayed in Figs. 36b and c yield the following values for the centroid and width of the DGDR in ^{136}Xe : $\langle E_{0^+} \rangle = 30.68$ MeV and $\Gamma_{0^+} = 6.82$ MeV for the 0^+ component of the DGDR and $\langle E_{2^+} \rangle = 30.71$ MeV and $\Gamma_{2^+} = 6.84$ MeV for the 2^+ component. These values have to be compared to $\langle E_{1^-} \rangle = 15.40$ MeV and $\Gamma_{1^-} = 4.72$ MeV for the single GDR in this nucleus from our calculation. The correspondence between these values is presented in Table 15 in comparison with the prediction of the harmonic model. Also shown is the ratio

$$R = \frac{\sum_v \sum_{v_1} \langle \Psi_{0^+(2^+)}^v | \mathcal{M}(E1) | \Psi_{1^+}^{v_1} \rangle \cdot \langle \Psi_{1^+}^{v_1} | \mathcal{M}(E1) | \Psi_{\text{g.s.}} \rangle|^2}{|\sum_{v_1} \langle \Psi_{1^+}^{v_1} | \mathcal{M}(E1) | \Psi_{\text{g.s.}} \rangle|^4} \quad (270)$$

between the two-step excitation probability of the DGDR normalized to the summed excitation probability of the one-phonon GDR. The numerical results lie quite close to the predictions of the harmonical model (see also a discussion of this problem in Ref. [110]). While the on-the-energy-shell transitions are easier to identify and calculate properly, off-the-energy shell corrections are considerably more elusive. In fact, it may be argued that the calculated shift of the energy centroid of the DGDR with respect to that expected in the harmonic picture is somewhat underestimated, because of the limitations used in selecting two-phonon basis states used in the calculation. Our calculated value $\Delta E = 2\langle E_{\text{GDR}} \rangle - \langle E_{\text{DGDR}} \rangle$ shown in Table 15 can be compared to the ones in ^{40}Ca [111] and ^{208}Pb [74] in calculations with Skyrme forces. One of the purposes of the last calculations was to consider the anharmonic properties of the DGDR with the wave function which includes collective $1p1h$ and $2p2h$ states. Thus, an interaction not only between the two-phonon DGDR states, [$1^- \times 1^-$] among themselves, but with other two-phonon states made up of collective 2^+ and 3^- phonons was taken into account. The reported value of ΔE in these studies is of the order of -200 keV in consistency with our results. It should be pointed out that the calculation with Skyrme forces also yield somewhat larger anharmonicity shifts for low-lying two-phonon states as compared to the QPM calculations [112]. The most complete basis of the $2p2h$ configurations has been used in the second-RPA calculations of the DGDR properties in ^{40}Ca [97] and ^{208}Pb [98] which includes not only “collective phonons” but non-collective as well. The authors of Refs. [97,98] obtained the values of ΔE equal to -670 (-40) and -960 (-470) keV for 0^+ and 2^+ components of the DGDR, respectively, in ^{40}Ca (^{208}Pb). Recently, the problem of anharmonicity for the DGDR has been also studied within macroscopic approaches in

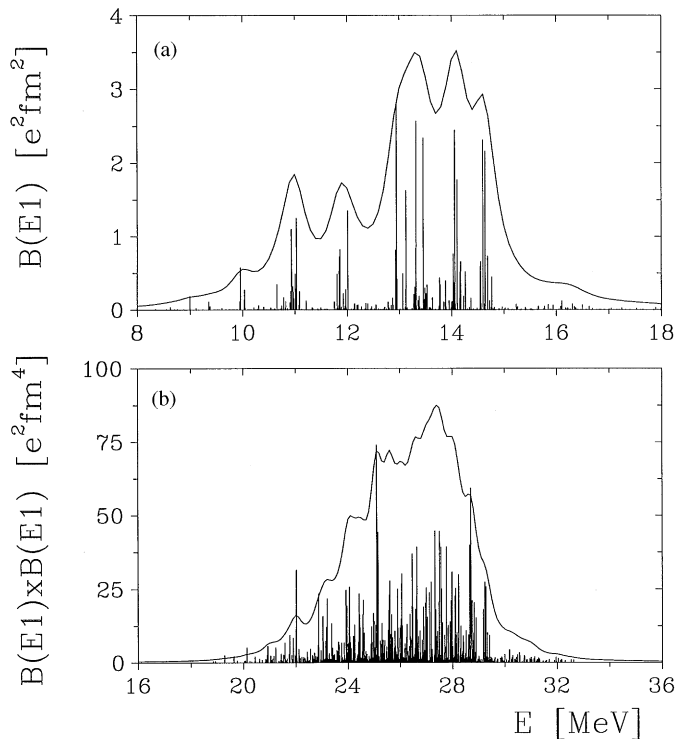


Fig. 37. (a) $B(E1)$ values for the GDR and (b) $[B(E1) \times B(E1)]$ values, Eq. (269), for the DGDR ($J = 0^+ + 2^+$) associated with Coulomb excitation in ^{208}Pb in relativistic heavy ion collision. A smooth curve is a result of averaging over all states with a smearing parameter $\Delta = 0.5$ MeV.

Refs. [76,113]. In Ref. [76] it has been concluded that the A -dependence of it should be as $A^{-4/3}$ while in Ref. [113] it is $A^{-2/3}$ in consistency with Ref. [55].

The fragmentation of the DGDR due to the coupling to three-phonon configurations has been also calculated in ^{208}Pb [109]. The fine structure of the GDR as a result of interaction with two-phonon 1^- configurations in this nucleus is presented in Fig. 37a. The $[B(E1) \times B(E1)]$ values for the DGDR states described by the wave function which includes two- and three-phonon configurations are plotted in Fig. 37b. In this calculation we have used the same basis of six the most collective one-phonon 1^- states for the GDR and 21 the most collective two-phonon [$1^- \times 1^-$] states for 0^+ and 2^+ components of the DGDR as in the coupled-channels calculation in the previous subsection (see Fig. 33). For a description of the GDR width a coupling to 1161 two-phonon 1^- configurations was taken into account. In calculation of the DGDR strength distribution we have neglected the interaction with one-phonon configurations and Pauli principle corrections since these effects are weaker in double-magic nucleus ^{208}Pb as compared to the ones in ^{136}Xe . As a result, the 0^+ and 2^+ components of the DGDR are completely degenerated in this calculation. The DGDR width is determined by the coupling of the selected 21 two-phonon configurations with 6972 three-phonon ones and is very close to $\sqrt{2}$ times the width of the GDR. This is a natural result for a folding of two independent phonons in microscopic treatment of the

problem. As already discussed in Section 3.3, when damping width of giant resonances is described phenomenologically by Breit–Wigner strength distribution one obtains the value 2 for the quantity $r = \Gamma_{\text{DGDR}}/\Gamma_{\text{GDR}}$. On the other hand, when the Gaussian strength distribution is used, it yields the value $r = \sqrt{2}$. This is due to the different behavior of the wings of the above-mentioned strength functions at infinity. In a microscopic picture, collective resonance state(s) couples to some finite number of doorway configurations and the strength distribution, as a result of this coupling, is always concentrated in a definite energy region. It results in $r = \sqrt{2}$.

The square of the amplitude $a_{J_f, M_f; J_i, M_i}^{(1)}(E)$ of the Coulomb excitation of one-phonon resonances in RHIC in the first-order perturbation theory has a smooth exponential energy dependence. This rather simplifies a calculation of the excitation cross section in RHIC of the states of Eq. (238) which form single-giant resonances. Although a large number of the states of Eq. (238), the giant resonance excitation cross section in this reaction can be easily calculated as a product of the $B(E1)$ values of each state, presented in Figs. 36a and 37a, and an interpolated value of the tabulated function $|a_{J_f, M_f; J_i, M_i}^{(1)}(E)|^2$ at $E = E_{v_f}^{J_f}$. The cross sections of the GDR and GQR excitation in ^{136}Xe (see Fig. 34) have been calculated this way. A similar procedure may be applied for calculation of the cross section of the DGDR($v_{0^+, 2^+}$) states excitation via the GDR(v_{1^-}) states. In the second-order perturbation theory it equals to

$$\sigma_{v_{0^+, 2^+}} = \left| \sum_{v_{1^-}} A(E_{v_{1^-}}, E_{v_{0^+, 2^+}}) \langle 1^-(v_{1^-}) || E1 || 0_{\text{g.s.}}^+ \rangle \langle [1^- \otimes 1^-](v_{0^+, 2^+}) || E1 || 1^-(v_{1^-}) \rangle \right|^2, \quad (271)$$

where $A(E_1, E_2)$ is the reaction amplitude which has a very smooth dependence on both arguments. This function was tabulated and used in the final calculation of the DGDR Coulomb excitation cross section in relativistic heavy ion collisions.

Let us consider the excitation of the DGDR in the projectile for a ^{208}Pb (640A MeV) + ^{208}Pb collision, according to the experiment in Ref. [54], and use the minimum value of the impact parameter, $b = 15.54$ fm, corresponding to the parameterization of Ref. [43]. The cross section for

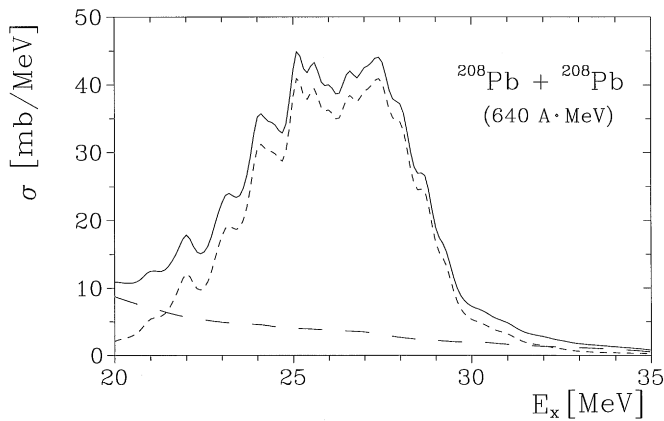


Fig. 38. The contribution for the excitation of two-phonon 1^- states (long-dashed curve) in first-order perturbation theory, and for two-phonon 0^+ and 2^+ DGDR states in second order (short-dashed curve). The total cross section (for ^{208}Pb (640A MeV) + ^{208}Pb) is shown by the solid curve.

Coulomb excitation of the DGDR is presented in Fig. 38 by the short-dashed curve as a strength function calculated with an averaging parameter equal to 1 MeV. The contribution of the background of the two-phonon 1^- states to the total cross section is shown by a long-dashed curve in the same figure. It was calculated in first-order perturbation theory. The role of the background in this reaction is much less important than in photoexcitation studies. First, it is because in heavy ion collisions we have a special mechanism to excite selected two-phonon states in the two-step process. Second, the Coulomb excitation amplitude is exponentially decreasing with the excitation energy, while the $E1$ -photoexcitation amplitude is linearly increasing. Nonetheless, Fig. 38 shows that the direct excitation of two-phonon 1^- states cannot be completely excluded from consideration of this reaction. Integrated over the energy interval from 20 to 35 MeV these states give a cross section of 50.3 mb which should be compared with the experimental cross section in the DGDR region for the ^{208}Pb (640A MeV) + ^{208}Pb reaction which is equal to 380 mb [54].

The solid line in Fig. 38 is the sum of DGDR and two-phonon background excitations in relativistic heavy ion collisions. The first and second moments of excitation functions, displayed by the short-dashed and solid curves in Fig. 38, indicate that the centroid of the total strength is 200 keV lower and the width is 16% larger than the same quantities for the pure DGDR. We point out that this 200 keV shift is even somewhat larger than the one due to the anharmonicities studied in ^{208}Pb [74].

Direct excitation of the two-phonon 1^- states in ^{208}Pb (640A MeV) + ^{208}Pb reaction was also investigated in Ref. [74] in calculation with Skyrme forces. The reported effect (a difference between 5.07 and 3.55 mb for $22 < E_x < 28$ MeV) is much weaker than in our calculation because of a rather limited two-phonon space. Another source of the DGDR enhancement in [74] is due to anharmonicity effects. We also checked the last by coupling one-phonon GDR states to (the most important) 1200 two-phonon 1^- states in the DGDR region. Due to the constructive interference between one- and two-phonon states at DGDR energies we got an additional enhancement of 24 mb, which is again larger than the difference between 6.42 and 3.55 mb obtained in Ref. [74] for the same reason.

The absolute value of the total cross section of the DGDR excitation in RHIC in ^{208}Pb is somewhat small in our calculation (cf. Table 13) as compared with the experimental findings. For example, the experimental value of the total DGDR excitation in the reaction ^{208}Pb (640A MeV) + ^{208}Pb , for which the calculations have been performed, equals to 0,38(4) b. As mentioned above, our chosen six 1^- states exhaust only 90.6% of EWSR while the photo-neutron data [32] indicate that this value equals to 122%. Due to this underestimate of exhaust of the EWSR the cross section for the DGDR excitation reduces more strongly than the one for the single GDR. This is because the GDR cross section is roughly proportional to the total $B(E1)$ value while for the DGDR it is proportional to the square of it.

If we apply a primitive scaling to obtain the experimental value 122% of EWSR the ratio $R = \sigma_{(\text{DGDR})}/\sigma_{(\text{GDR})}$, the last line of Table 13, changes into 0.096 and 0.101 for the coupled-channels calculation and for the perturbation theory, respectively. The experimental findings [54] yield the value $R_{\text{exp}} = 0.116 \pm 0.014$. The reported [54] disagreement $R_{\text{exp}}/R_{\text{calc}} = 1.33 \pm 0.16$ is the result of a comparison with R_{calc} obtained within a folding model, assuming 122% of the EWSR. We get a somewhat larger value of R_{calc} (taking into account our scaling procedure) because the $B(E1)$ strength distribution over our six 1^- states is not symmetrical with respect to the centroid energy, E_{GDR} : the lower part is enhanced. A weak energy dependence in the excitation amplitude, which is

also squared for the DGDR, enhances the DGDR cross section for a non-symmetrical distribution with respect to the symmetrical one, or when the GDR is treated as a single state. The effect of the energy dependence is demonstrated for a single GDR in the top part of Fig. 33 where the excitation cross sections are compared to the $B(E1)$ strength distribution. It produces a shift to lower energies of the centroid of the GDR and the DGDR cross sections with respect to the centroid of the $B(E1)$ and the $[B(E1) \times B(E1)]$ strength distribution, respectively. In our calculation this shift equals to 0.26 MeV for the GDR and to 0.33, 0.28 MeV for the DGDR within coupled channels and perturbation theory, respectively. Of course, this scaling procedure has no deep physical meaning but we have included this discussion to indicate that the disagreement between experiment and theory for the DGDR excitation cross sections in ^{208}Pb reached the stage when theoretical calculations have to provide a very precise description of both the GDR and the DGDR to draw up final conclusions.

The situation with the absolute values of cross sections of the DGDR excitation in ^{136}Xe in RHIC is much less clear than in ^{208}Pb . The experimental value for the reaction ^{136}Xe (700A MeV) + ^{208}Pb is reported to be equal to 215 ± 50 mb [40]. This value is sufficiently larger as compared to any theoretical predictions available (cf. Table 14). But it should be pointed out that a comparison between experimental data for xenon [40] and lead [54] reveal some essential contradiction. While for ^{208}Pb the above discussed quantity of the ratio between the total cross sections of the DGDR and GDR excitation $R_{\text{exp}}(^{208}\text{Pb}) = 0.116 \pm 0.014$, its value for ^{136}Xe : $R_{\text{exp}}(^{136}\text{Xe}) = 0.21 \pm 0.05$ [40]. Taking into account that experiments for both nuclei have been performed at close projectile energies (per nucleon) and the cross section of the GDR excitation in ^{136}Xe is about three times less as compared to the one in ^{208}Pb , the ratio $R_{\text{exp}}(^{136}\text{Xe})$ should be sufficiently smaller than $R_{\text{exp}}(^{208}\text{Pb})$ and not vice versa. Probably, the problem with the absolute value of the DGDR excitation in ^{136}Xe is related to uncertainties in separating of the contribution of single resonances, the characteristics of which are unknown experimentally for this nucleus and the results of interpolation have been used in evaluating the experimental data. Recently, the experiment for ^{136}Xe has been repeated by LAND collaboration [114]. The analysis of the new data in the nearest future should clear up the situation.

5.4. The role of transitions between complex configurations of the GDR and the DGDR

In the previous subsection considering the excitation properties of the DGDR, $[B(E1) \times B(E1)]$ values or excitation cross sections in RHIC in second-order perturbation theory, we have taken into account only the transition matrix elements between simple one-phonon 1^- GDR and two-phonon 0^+ or 2^+ DGDR configurations for the second step of the excitation process g.s. \rightarrow GDR \rightarrow DGDR. In fact, as already discussed above these configurations couple to more complex ones to produce the widths of single and double resonances and, in principle, additional transitions between complex configurations of the GDR and the DGDR, together with interference effects, may alter the predicted values of excitation probabilities. This problem will be considered in the present subsection (see, also Ref. [115]). It will be concluded that their role is marginal in the process under consideration although a huge amount of the $E1$ -strength is hidden in the GDR \rightarrow DGDR transition. This negative result ensures that calculations, in which only transitions between simple components of the GDR and DGDR are taken into account and which are much easier to carry out, require no further corrections.

In microscopic approaches the strength of the GDR is split among several one-phonon 1_{α}^{-} states (due to the Landau damping). The wave function $|1_{\alpha}^{-}\rangle$ couples to complex configurations $|1_{\beta}^{-}\rangle$ yielding the GDR width. We use the index α for simple configurations and the index β for complex ones, respectively. Thus, the wave function of the i th 1^{-} state in the GDR energy region can be schematically written as

$$|1_i^{-}\rangle = \sum_{\alpha} S_i^{\text{GDR}}(\alpha)|1_{\alpha}^{-}\rangle + \sum_{\beta} C_i^{\text{GDR}}(\beta)|1_{\beta}^{-}\rangle, \quad (272)$$

where the coefficients $S_i^{\text{GDR}}(\alpha)$ and $C_i^{\text{GDR}}(\beta)$ may be obtained by diagonalizing the nuclear model Hamiltonian on the set of wave functions (272).

The total $E1$ -strength of the GDR excitation from the ground state,

$$B_{\text{GDR}}(E1) = \sum_i |\langle 1_i^{-} || E1 || 0_{\text{g.s.}}^{+} \rangle|^2,$$

remains practically the same as in the one-phonon RPA calculation because the direct excitation of complex configurations from the ground state is a few orders of magnitude weaker as compared to excitation of one-phonon states. However these complex configurations play a fundamental role for the width of the GDR.

The wave function of the 2^{+} component of the DGDR states can be written in the similar fashion:

$$|2_f^{+}\rangle = \sum_{\tilde{\alpha}=\{\alpha_1 \times \alpha_2\}} S_f^{\text{DGDR}}(\tilde{\alpha})|[1_{\alpha_1}^{-} \times 1_{\alpha_2}^{-}]_{2^{+}}\rangle + \sum_{\alpha''} \tilde{S}_f^{\text{DGDR}}(\alpha'')|2_{\alpha''}^{+}\rangle + \sum_{\beta'} C_f^{\text{DGDR}}(\beta')|2_{\beta'}^{+}\rangle. \quad (273)$$

In this equation, we have separated in the first term the $[1^{-} \times 1^{-}]$ DGDR configurations from other two-phonon configurations (second term) and complex configurations (the last term). The same equation as (273) is valid for the 0^{+} DGDR states.

The total $E1$ -transition strength between the GDR and DGDR,

$$\sum_f \sum_i |\langle 2^{+}(0^{+})_f || E1 || 1_i^{-} \rangle|^2,$$

is much larger as compared to that for the GDR excitation, $\sum_i |\langle 1_i^{-} || E1 || 0_{\text{g.s.}}^{+} \rangle|^2$, from the ground state. This is because the former includes transitions not only between simple GDR and DGDR states but also between complex configurations as well. The enhancement factor should be the ratio between the density of simple and complex configuration in the GDR energy region. But in the two-step excitation process the sum over intermediate GDR states in Eq. (274) reduces the total transition strength for g.s. \rightarrow GDR \rightarrow DGDR to $\sim 2 \cdot |B_{\text{GDR}}(E1)|^2$ (the factor 2 appears due to the bosonic character of the two phonons which also holds if Landau damping is taken into account). To prove this let us consider the excitation probability of the DGDR

$$P_{\text{DGDR}}(E_f, b) = \frac{1}{4} \sum_{M_f} \left| \sum_{i, M_i} a_{0(0) \rightarrow 1_i^{-}(M_i)}^{E1(\mu)}(E_i, b) \times a_{1_i^{-}(M_i) \rightarrow [1^{-} \times 1^{-}]_f(M_f)}^{E1(\mu')}(E_f - E_i, b) \right|^2, \quad (274)$$

where the index i labels intermediate states belonging to the GDR, and $a_{J_1(M_1) \rightarrow J_2(M_2)}^{E1(\mu)}$ is the first-order $E1$ excitation amplitude for the transition $J_1(M_1) \rightarrow J_2(M_2)$ in a collision with impact

parameter b . For each state, J and M denote the total angular momentum and the magnetic projection, respectively.

The amplitude $a_{J_1(M_1) \rightarrow J_2(M_2)}^{E1(\mu)}$ is given by

$$a_{J_1(M_1) \rightarrow J_2(M_2)}^{E1(\mu)}(E, b) = (J_1 M_1 1 \mu | J_2 M_2) \times \langle J_2 || E1 || J_1 \rangle f_{E1(\mu)}(E, b). \quad (275)$$

It is a product of the reduced matrix element $\langle J_2 || E1 || J_1 \rangle$ for the $E1$ -transition between the states $J_1(M_1)$ and $J_2(M_2)$ which carries nuclear structure information and the reaction function $f_{E1(\mu)}(E, b)$. The latter depends on the excitation energy, charge of the target, beam energy, and is calculated according to Ref. [18]. Except for the dependence on the excitation energy, it does not carry any nuclear structure information. The cross section for the DGDR is obtained from Eq. (274) by integration over impact parameters, starting from a minimal value b_{\min} to infinity. This minimal value is chosen according to Ref. [19]. Now we substitute the wave functions of the GDR and DGDR states given by Eqs. (272) and (273) in expression (274). We obtain two terms. The first one corresponds to transitions between simple GDR and DGDR states (after the GDR is excited from the ground state through its simple component):

$$A_{\mu\mu'} = \sum_i \sum_{\alpha\alpha'\tilde{\alpha}} S_i^{\text{GDR}}(\alpha) f_{E1(\mu)}(E_i, b) \langle 1_{\alpha}^- || E1 || 0_{\text{g.s.}}^+ \rangle \\ \times S_i^{\text{GDR}}(\alpha') S_f^{\text{DGDR}}(\tilde{\alpha}) f_{E1(\mu')}(E_f - E_i, b) \langle [1_{\alpha_1}^- \times 1_{\alpha_2}^-]_f || E1 || 1_{\alpha'}^- \rangle \delta_{\alpha_2, \alpha'} \quad (276)$$

and the second one accounts transitions between complex configurations in the wave functions of Eqs. (272) and (273):

$$B_{\mu\mu'} = \sum_i \sum_{\alpha\alpha'\beta\beta'} S_i^{\text{GDR}}(\alpha) f_{E1(\mu)}(E_i, b) \langle 1_{\alpha}^- || E1 || 0_{\text{g.s.}}^+ \rangle \\ \times C_i^{\text{GDR}}(\beta) C_f^{\text{DGDR}}(\beta') f_{E1(\mu')}(E_f - E_i, b) \langle [1_{\alpha'}^- \times 1_{\beta}^-]_f || E1 || 1_{\beta'}^- \rangle \delta_{\beta', [\alpha' \times \beta]}. \quad (277)$$

The second reduced matrix element in the above equations is proportional to the reduced matrix element between the ground state and the simple one-phonon configuration (see Eq. (261)).

For a given impact parameter b , the function $f_{E1(\mu)}(E, b)$ can be approximated by a constant value $f_{E1(\mu)}^0$ [6] for the relevant values of the excitation energies. Then the energy dependence can be taken out of summations and orthogonality relations between different components of the GDR wave functions can be applied [107]. The orthogonality relations between the wave functions imply that

$$\sum_i S_i^{\text{GDR}}(\alpha) C_i^{\text{GDR}}(\beta) \equiv 0. \quad (278)$$

This means that the term $B_{\mu\mu'}$ vanishes. The term $A_{\mu\mu'}$ summed over projections and all final states yields a transition probability to the DGDR, $P_{\text{DGDR}}(E_f, b)$, which is proportional to $2 \cdot |B_{\text{GDR}}(E1)|^2$ in second-order perturbation theory. This argument was the reason for neglecting the term $B_{\mu\mu'}$ in previous calculations of DGDR excitation where the coupling of simple GDR and DGDR states to complex configurations was taken into account.

In Fig. 39 we plot the value of $\chi_{E1}(E) = 2\pi \int db b \sum_{\mu} |f_{E1(\mu)}(E, b)|^2$ as a function of energy calculated for the ^{208}Pb (640A MeV) + ^{208}Pb reaction. This value corresponds to σ_{GDR} if $B_{\text{GDR}}(E1) = 1$. The square in this figure indicates the location of the GDR in ^{208}Pb . This figure demonstrates that the

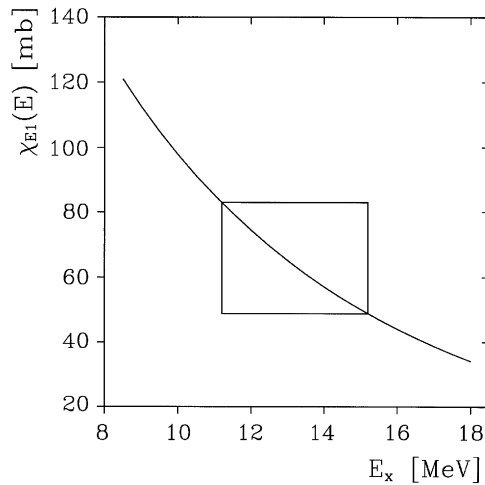


Fig. 39. The energy dependence of the ^{208}Pb (640A MeV) + ^{208}Pb reaction function calculated within first-order perturbation theory. The square indicates the location of the GDR in ^{208}Pb .

function $\chi_{E1}(E)$ changes by 60% in the GDR energy region. The role of this energy dependence for other effects has been considered in Refs. [19,74]. Taking into account that one-phonon 1_{α}^{-} configurations are fragmented over a few MeV [108], when a sufficiently large two-phonon basis is included in the wave function given by Eq. (272), the role of the $B_{\mu\mu'}$ term in the excitation of the DGDR should be studied in more detail.

To accomplish this task we have performed firstly a simplified calculation in which we used the *boson-type* Hamiltonian:

$$H = \sum_{\alpha} \omega_{\alpha} Q_{\alpha}^{\dagger} Q_{\alpha} + \sum_{\beta} \tilde{\omega}_{\beta} \tilde{Q}_{\beta}^{\dagger} \tilde{Q}_{\beta} + \sum_{\alpha, \beta} U_{\beta}^{\alpha} (Q_{\alpha}^{\dagger} \tilde{Q}_{\beta} + \text{h.c.}), \quad (279)$$

where Q_{α}^{\dagger} is the phonon creation operator and ω_{α} is the energy of this one-phonon configuration; $\tilde{Q}_{\beta}^{\dagger}$ is the operator for creation of a complex configuration with energy $\tilde{\omega}_{\beta}$ and U_{β}^{α} is the matrix element for the interaction between these configurations. We have assumed that the energy difference between two neighboring one-phonon configurations is constant and equals to $\Delta\omega$. An equidistant spacing with the energy $\Delta\tilde{\omega}$ was assumed for the complex configurations. We also have used a constant value U for the matrix elements of the interaction. The $B_{\text{GDR}}(E1)$ value was distributed symmetrically over one-phonon configurations. Thus, the free parameters of this model are: $\Delta\omega$, $\Delta\tilde{\omega}$, U , the number of one-phonon and complex configurations, and the distribution of the $B_{\text{GDR}}(E1)$ value over the simple configurations. The only condition we want to be satisfied is that the energy spectrum for the GDR photoexcitation is the same as the one known from experiment.

After all parameters are fixed we diagonalize the model Hamiltonian of Eq. (279) on the set of wave functions of Eq. (272) for the GDR and on the set of Eq. (273) for the DGDR. The diagonalization procedure yields the information on eigenenergies of the 1_{i}^{-} GDR states and on the coefficients $S_{i}^{\text{GDR}}(\alpha)$ and $C_{i}^{\text{GDR}}(\beta)$, respectively. One also obtains information on eigenenergies of the 2_{f}^{\dagger} or 0_{f}^{\dagger} DGDR states and the coefficients $S_{f}^{\text{DGDR}}(\tilde{\alpha})$ and $C_{f}^{\text{DGDR}}(\beta')$, respectively. With this

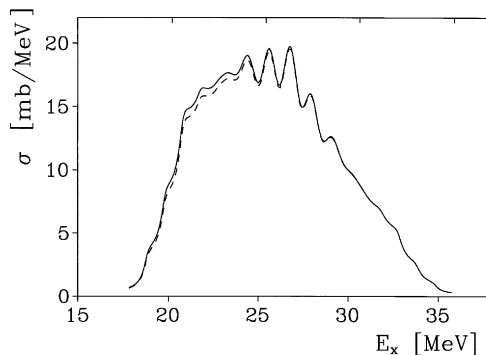


Fig. 40. The cross section for the excitation of the 2^+ component of the DGDR in the reaction ^{208}Pb (640A MeV) + ^{208}Pb , calculated within second-order perturbation theory. The dashed curve shows the contribution of the $E1$ -transition between simple GDR and DGDR configurations only. The solid curve is a sum of the above result and the contribution of the $E1$ -transitions between complex GDR and DGDR configurations. See text for details.

information we are able to study the role of the $B_{\mu\mu'}$ term in the excitation of the DGDR in RHIC.

The big number of free parameters allows an infinite number of suitable choices. In fact, not all of the parameters are really independent. For example, the increase in the number of simple or complex configurations goes together with the decreasing of the value of U . This is necessary for a correct description of the GDR photoabsorption cross section. This makes it possible to investigate the role of the $B_{\mu\mu'}$ term in different conditions of weak and strong Landau damping and for different density of complex configurations. In our calculations we vary the number of collective simple states from one to seven and the number of complex configurations from 50 to 500. The value of U then changes from about 100–500 keV. The results of one of these calculations for the excitation of the 2^+ component of the DGDR in ^{208}Pb (640A MeV) + ^{208}Pb collisions are presented in Fig. 40. For a better visual appearance the results are averaged with a smearing parameter equal to 1 MeV. The dashed curve shows the results of a calculation in which $\sigma_{\text{DGDR}}^A(E) \equiv \sigma_{\text{DGDR}}(E) \sim \int db b |A_{\mu\mu'}|^2$ and the results of another one in which $\sigma_{\text{DGDR}}^{A+B}(E) \equiv \sigma_{\text{DGDR}}(E) \sim \int db b |A_{\mu\mu'} + B_{\mu\mu'}|^2$ are represented by a solid curve.

Our calculation within this simple model indicates that the role of the $B_{\mu\mu'}$ term in second-order perturbation theory is negligibly small, although the total $B(E1)$ strength for transitions between complex GDR and DGDR configurations, considered separately, is more than two orders of magnitude larger than the ones between simple GDR and DGDR configurations. The value $\Delta\sigma = (\sigma_{\text{DGDR}}^{A+B} - \sigma_{\text{DGDR}}^A) / \sigma_{\text{DGDR}}^A$, where $\sigma_{\text{DGDR}}^{A+B} = \int \sigma_{\text{DGDR}}^{A+B}(E) dE$, changes in these calculations from 1% to 2.5%. The results practically do not depend on the number of complex configurations accounted for. The maximum value of $\Delta\sigma$ is achieved in a calculation with a single one-phonon GDR state (no Landau damping). This is because the value of U is larger in this case and the fragmentation of the one-phonon state is stronger. Thus, in such a situation, the energy dependence of the reaction amplitude modifies appreciably the orthogonality relations. But in general the effect is marginal.

We also performed a calculation with more realistic wave functions for the GDR and DGDR states taken from our studies presented in the previous subsection. These wave functions include

6 and 21 simple states for the GDR and DGDR, respectively. The complex configurations are two-phonon states for the GDR and three-phonon states for the DGDR. The value $\Delta\sigma$ equals in this realistic calculation to 0.5%. This result is not surprising because realistic calculations with only two-phonon complex configurations, and a limited number of them, somewhat underestimate the GDR width which is crucial for the modification of the orthogonality relations.

We have proved that the transitions between complex GDR and DGDR configurations within second-order perturbation theory for the DGDR excitation in RHI collisions play a marginal role in the process under consideration and it is sufficient to take into account only transitions between the ground-state and one-phonon GDR and two-phonon DGDR configurations.

5.5. The DGDR in deformed nuclei

The possibility to observe two-phonon giant resonances in deformed nuclei with the present state-of-art experimental techniques is still questionable. This is mainly due to the fact that one has to expect a larger width of these resonances as compared to spherical nuclei. Also, the situation with the low-lying two-phonon states in deformed nuclei is much less clear than in spherical ones.

The first experiment with the aim to observe the double-giant dipole resonance (DGDR) in ^{238}U in relativistic heavy ion collisions (RHIC) was performed recently at the GSI/SIS facility by the LAND collaboration [114]. It will take some time to analyze the experimental data and to present the first experimental evidence of the DGDR in deformed nuclei, if any. Thus, we present here the first theoretical predictions of the properties of the DGDR in deformed nuclei based on microscopic study [116]. The main attention will be paid to the width of the DGDR and its shape.

In a phenomenological approach the GDR is considered as a collective vibration of protons against neutrons. In spherical nuclei this state is degenerate in energy for different values of the spin $J = 1^-$ projection $M = 0, \pm 1$. The same is true for the 2^+ component of the DGDR with projection $M = 0, \pm 1, \pm 2$. In deformed nuclei with an axial symmetry like ^{238}U , the GDR is split into two components $I^\pi(K) = 1^-(0)$ and $I^\pi(K) = 1^-(\pm 1)$ corresponding to vibrations against two different axes. In this approach one expects a three-bump structure for the DGDR with the value $K = 0, K = \pm 1$ and $K = 0, \pm 2$, respectively (see Fig. 41). Actually, the GDR possesses a width and the main mechanism responsible for it in deformed nuclei is the Landau damping. Thus, the conclusion on how three bumps overlap and what is the real shape of the DGDR in these nuclei, i.e., either a three-bump or a flat broad structure, can be drawn out only from some consistent microscopic studies.

We use in our calculations for ^{238}U the parameters of Woods–Saxon potential for the average field and monopole pairing from Ref. [117]. They were adjusted to reproduce the properties of the ground-state and low-lying excited states. The average field has a static deformation with the deformation parameters $\beta_2 = 0.22$ and $\beta_4 = 0.08$. To construct the phonon basis for the $K = 0$ and $K = \pm 1$ components of the GDR we use the dipole-dipole residual interaction (for more details of the QPM application to deformed nuclei, see e.g. Ref. [84]). The strength parameters of this interaction are taken from Ref. [118] where they have been fitted to obtain the centroid of the $B(E1, 0_{g.s.}^+ \rightarrow 1^-(K = 0, \pm 1))$ strength distribution at the value known from experiment [119] and to exclude the center of mass motion. In this approach, the information on the phonon basis (i.e. the excitation energies of phonons and their internal fermion structure) is obtained by solving

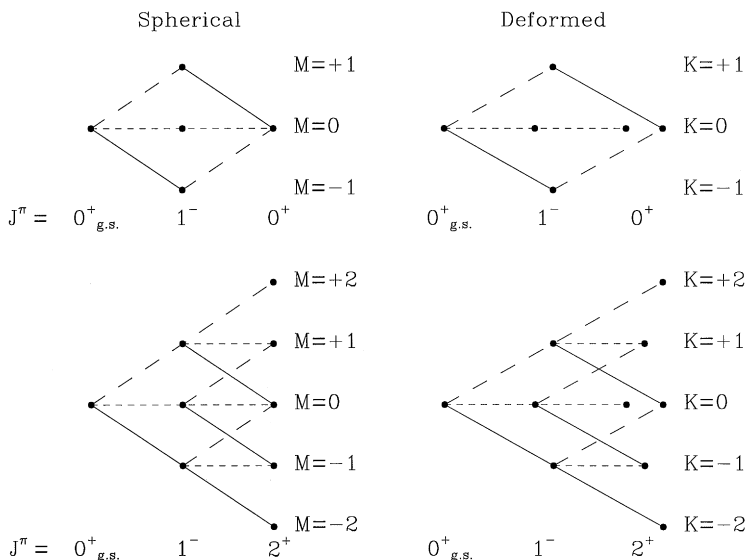


Fig. 41. The possible paths to the excitation of a given magnetic substate of the 0^+ and 2^+ components of the DGDR in spherical and deformed nuclei. The notations are the same as in Fig. 32.

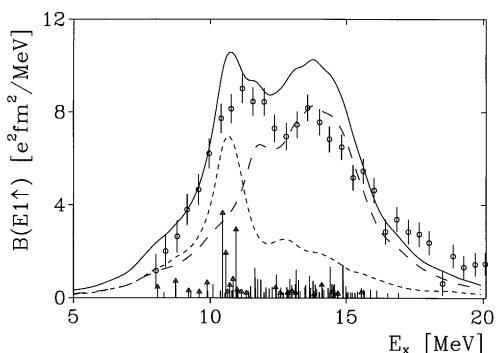


Fig. 42. The $B(E1)$ strength distribution over $K = 0$ (short-dashed curve) and $K = \pm 1$ (long-dashed curve) 1^- states in ^{238}U . The solid curve is their sum. The strongest one-phonon 1^- states are shown by vertical lines, the ones with $K = 0$ are marked by a triangle on top. Experimental data are from Ref. [119].

the RPA equations. For electromagnetic $E1$ -transitions we use the values of the effective charges, $e_{\text{eff}}^{Z(N)} = eN(-Z)/A$ to separate the center of mass motion.

The results of our calculation of the $B(E1)$ strength distribution over $|1_{\bar{K}=0}(i)\rangle$ and $|1_{\bar{K}=\pm 1}(i')\rangle$ GDR states are presented in Fig. 42, together with experimental data. The index i in the wave function stands for the different RPA states. All one-phonon states with the energy lower than 20 MeV and with the $B(E1)$ value larger than $10^{-4} e^2 \text{ fm}^2$ are accounted for. Their total number equals to 447 and 835 for the $K = 0$ and $K = \pm 1$ components, respectively. Only the strongest of them with $B(E1) \geq 0.2 e^2 \text{ fm}^2$ are shown in the figure by vertical lines. Our phonon basis exhausts

32.6% and 76.3% of the energy weighted sum rules, $14.8 \cdot NZ/A e^2 \text{ fm}^2 \text{ MeV}$, by the $K = 0$ and $K = \pm 1$ components, respectively. For a better visual appearance we also present in the same figure the strength functions averaged with a smearing parameter, which we take as 1 MeV. The short (long) dashed-curve represent the $K = 0$ ($K = \pm 1$) components of the GDR. The solid curve is their sum. The calculation reproduces well the two-bump structure of the GDR and the larger width of its $K = \pm 1$ component. The last is consistent with the experiment [119] which is best fitted by two Lorentzians with widths equal to $\Gamma_1 = 2.99 \text{ MeV}$ and $\Gamma_2 = 5.10 \text{ MeV}$, respectively. The amplitudes of both maxima in the calculation are somewhat overestimated as compared to the experimental data. This happens because the coupling of one-phonon states to complex configurations is not taken into account which can be more relevant for the $K = \pm 1$ peak at higher energies. But in general the coupling matrix elements are much weaker in deformed nuclei as compared to spherical ones and the Landau damping describes the GDR width on a reasonable level.

The wave functions of the 0^+ and 2^+ states belonging to the DGDR are constructed by the folding of two 1^- phonons from the previous calculation. When a two-phonon state is constructed as the product of two identical phonons its wave function gets an additional factor $1/\sqrt{2}$. The 1^+ component of the DGDR is not considered here for the same reasons as in spherical nuclei. The anharmonicity effects which arise from interactions between different two-phonon states are also not included in the present study.

The folding procedure yields three groups of the DGDR states:

$$|[1_{\bar{K}=0}(i_1) \otimes 1_{\bar{K}=0}(i_2)]_{0_{\bar{K}=0}, 2_{\bar{K}=0}} \rangle, \quad (280a)$$

$$|[1_{\bar{K}=0}(i) \otimes 1_{\bar{K}=\pm 1}(i')]_{2_{\bar{K}=\pm 1}} \rangle, \quad (280b)$$

$$|[1_{\bar{K}=\pm 1}(i'_1) \otimes 1_{\bar{K}=\pm 1}(i'_2)]_{0_{\bar{K}=0}, 2_{\bar{K}=0, \pm 2}} \rangle. \quad (280c)$$

The total number of non-degenerate two-phonon states equals to about 1.5×10^6 . The energy centroid of the first group is the lowest and of the last group is the highest among them. So, we also obtain the three-bump structure of the DGDR. But the total strength of each bump is fragmented over a wide energy region and they strongly overlap.

Making use of the nuclear structure elements discussed above, we have calculated the excitation of the DGDR in ^{238}U projectiles ($0.5 \text{ GeV} \cdot \text{A}$) incident on ^{120}Sn and ^{208}Pb targets, following the conditions of the experiment in Ref. [114]. These calculations have been performed in second-order perturbation theory [6], in which the DGDR states of Eqs. (280a), (280b) and (280c) are excited within a two-step process: g.s. \rightarrow GDR \rightarrow DGDR. As intermediate states, the full set of one-phonon $|1_{\bar{K}=0}(i)\rangle$ and $|1_{\bar{K}=\pm 1}(i')\rangle$ states was used. We have also calculated the GDR excitation to first order for the same systems. The minimal value of the impact parameter, which is very essential for the absolute values of excitation cross section has been taken according to $b_{\min} = 1.28 \cdot (A_t^{1/3} + A_p^{1/3})$.

The results of our calculations are summarized in Fig. 43 and Table 16. In Fig. 43 we present the cross sections of the GDR (part a) and the DGDR (part b) excitation in the $^{238}\text{U} (0.5 \text{ GeV} \cdot \text{A}) + ^{208}\text{Pb}$ reaction. We plot only the smeared strength functions of the energy distributions because the number of two-phonon states involved is numerous. The results for $^{238}\text{U} (0.5 \text{ GeV} \cdot \text{A}) + ^{120}\text{Sn}$ reaction look very similar and differ only by the absolute value of cross

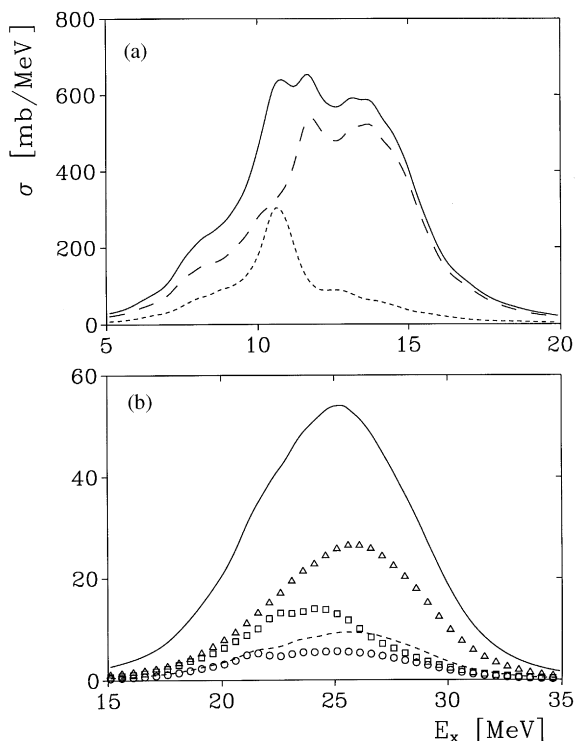


Fig. 43. The strength functions for the excitation: (a) of the GDR, and (b) of the DGDR in ^{238}U in the ^{238}U (0.5A GeV) + ^{208}Pb reaction. In (a), the short-dashed curve corresponds to the GDR ($K = 0$) and the long-dashed curve to the GDR ($K = \pm 1$). In (b) the dashed curve corresponds to the DGDR $_{0^+}$ ($K = 0$), the curve with circles to the DGDR $_{2^+}$ ($K = 0$), the curve with squares to the DGDR $_{2^+}$ ($K = \pm 1$), and the curve with triangles to the DGDR $_{2^+}$ ($K = \pm 2$). The solid curve is the sum of all components. The strength functions are calculated with the smearing parameter equal to 1 MeV.

Table 16

The properties of the different components of the GDR and the DGDR in ^{238}U . The energy centroid E_c , the second moment of the strength distribution m_2 in RHIC, and the cross sections σ for the excitation of the projectile are presented for: (a) ^{238}U (0.5A GeV) + ^{120}Sn , and (b) ^{238}U (0.5A GeV) + ^{208}Pb

| | E_c | m_2 | σ (mb) | |
|-------------------------------|-------|-------|---------------|--------|
| | (MeV) | (MeV) | (a) | (b) |
| GDR($K = 0$) | 11.0 | 2.1 | 431.2 | 1035.4 |
| GDR($K = \pm 1$) | 12.3 | 2.6 | 1560.2 | 3579.1 |
| GDR(total) | 12.0 | 2.6 | 1991.4 | 4614.5 |
| DGDR $_{0^+}$ ($K = 0$) | 25.0 | 3.4 | 18.3 | 88.9 |
| DGDR $_{2^+}$ ($K = 0$) | 24.4 | 3.5 | 11.8 | 58.7 |
| DGDR $_{2^+}$ ($K = \pm 1$) | 23.9 | 3.2 | 22.7 | 115.4 |
| DGDR $_{2^+}$ ($K = \pm 2$) | 25.3 | 3.4 | 49.7 | 238.3 |
| DGDR(total) | 24.8 | 3.4 | 102.5 | 501.3 |

sections. In Table 16 the properties of the GDR and the DGDR, and their different K components are given. The energy centroid E_c and the second moment, $m_2 = \sqrt{\sum_k \sigma_k (E_k - E_c)^2 / \sum_k \sigma_k}$, of the distributions are averaged values for the two reactions under consideration.

The two-bump structure can still be seen in the curve representing the cross section of the GDR excitation in ^{238}U in RHIC as a function of the excitation energy. But its shape differs appreciably from the $B(E1)$ strength distribution (see Fig. 43a in comparison with Fig. 42). The reason for this is the role of the virtual photon spectra. First, for the given value of the excitation energy and impact parameter it is larger for the $K = \pm 1$ component than that for the $K = 0$ one (see also the first two lines in Table 16). Second, for both components it has a decreasing tendency with an increase of the excitation energy [6]. As a result, the energy centroid of the GDR excitation in RHIC shifts by the value 0.7 MeV to lower energies as compared to the same value for the $B(E1)$ strength distribution. The second moment m_2 increases by 0.2 MeV.

The curves representing the cross sections of the excitation of the $K = \pm 1$ and $K = \pm 2$ components of the DGDR in ^{238}U in RHIC have typically a one-bump structure (see the curves with squares and triangles in Fig. 43b, respectively). It is because they are made of two-phonon 2^+ states of one type: the states of Eqs. (280b) and (280c), respectively. Their centroids should be separated by an energy approximately equal to the difference between the energy centroids of the $K = 0$ and $K = \pm 1$ components of the GDR. They correspond to the second and the third bumps in a phenomenological treatment of the DGDR. The $K = 0$ components of the DGDR include two group of states: the states represented by Eq. (280a) and those of Eq. (280c). Its strength distribution has two bumps (see the curve with circles for the $2^+(K = 0)$ and the dashed curve for the $0^+(K = 0)$ components of the DGDR, respectively). The excitation of the states given by Eq. (280a) in RHIC is enhanced due to their lower energies, while the enhancement of the excitation of the states given by Eq. (280c) is related to the strongest response of the $K = \pm 1$ components to the external $E1$ Coulomb field in both stages of the two-step process.

Summing together all components of the DGDR yields a broad one-bump distribution for the cross section for the excitation of the DGDR in ^{238}U , as a function of excitation energy. It is presented by the solid curve in Fig. 43b. Another interesting result of our calculations is related to the position of the DGDR energy centroid and to the second moment of the DGDR cross section. The centroid of the DGDR in RHIC is shifted to the higher energies by about 0.8 MeV from the expected value of two times the energy of the GDR centroid. The origin for this shift is in the energy dependence of the virtual photon spectra and it has nothing to do with anharmonicities of the two-phonon DGDR states. In fact, the energy centroid of the $B(E1, g.s. \rightarrow 1_i^-) \times B(E1, 1_i^- \rightarrow \text{DGDR}_f)$ strength function appears exactly at twice the energy of the centroid of the $B(E1, g.s. \rightarrow \text{GDR})$ strength distribution because the coupling between different two-phonon DGDR states are not accounted for in the present calculation. The same shift of the DGDR from twice the energy position of the GDR in RHIC also takes place in spherical nuclei. But the value of the shift is smaller there because in spherical nuclei the GDR and the DGDR strength is less fragmented over their simple configurations due to the Landau damping. But the larger value of the shift under consideration in deformed nuclei should somehow simplify the separation of the DGDR from the total cross section in RHIC.

Another effect which also works in favor of the extraction of the DGDR from RHIC excitation studies with deformed nuclei is its smaller width than $\sqrt{2}$ times the width of the GDR, as observed with spherical nuclei. Our calculation yields the value 1.33 for the ratio $\Gamma_{\text{DGDR}}/\Gamma_{\text{GDR}}$ in this

reaction. The origin for this effect is in the different contributions of the GDR $K = 0$ and $K = \pm 1$ components to the total cross section, due to the reaction mechanism. It should be remembered that only the Landau damping is accounted for the width of both the GDR and the DGDR. But since the effect of narrowing of the DGDR width is due to the selectivity of the reaction mechanism it will still hold if the coupling to complex configurations is included in the calculation.

It may be argued that the procedure of independent excitations of two RPA phonons applied here is not sufficient for a consistent description of the properties of the two-phonon giant resonances. This is true for the case of spherical nuclei where only the coupling of two GDR phonons to more complex, $3p3h$, configurations allows one to describe the DGDR width as discussed above. But the typical matrix element of this coupling in deformed nuclei does not exceed the value of 200 keV [120] while in spherical nuclei it is an order of magnitude larger. It means that due to the coupling, the strength of each GDR RPA-phonon will fragment within the energy interval of 100–200 keV in deformed nuclei. The last value should be compared to the second moment, m_2 , presented in Table 16 which is the result of the Landau damping accounted for in our calculation. Taking into account that the reaction amplitude has very weak energy dependence and that mixing of different RPA phonons in the GDR wave function does not change the total strength [115], the total cross sections of the GDR and DGDR excitation in RHIC will be also conserved.

Acknowledgements

We thank our colleagues G. Baur, P.F. Bortignon, R.A. Broglia, L.F. Canto, M. Hussein, A.F.N. de Toledo Piza, A.V. Sushkov, V.V. Voronov for fruitful collaboration. We also thank H. Emling for many fruitful and stimulative discussions. This work was supported in part by the Brazilian agencies CNPq, FINEP/PRONEX, FAPERJ and FUJB, the Russian Fund for Basic Research (grant no. 96-15-96729) and the Research Council of the University of Gent.

References

- [1] W. Bothe, W. Gentner, *Z. Phys.* 106 (1937) 236.
- [2] M. Goldhaber, E. Teller, *Phys. Rev.* 74 (1948) 1046.
- [3] H. Steinwedel, J.H.D. Jensen, *Z. Naturforsch.* 5a (1950) 413.
- [4] J. Speth, J. Wambach, in: J. Speth (Ed.), *Int. Review of Nuclear and Particle Physics*, World Scientific, Singapore, Vol. 7, 1991.
- [5] F. Bertrand, *Annu. Rev. Nucl. Sci.* 26 (1976) 457.
- [6] C.A. Bertulani, G. Baur, *Phys. Rep.* 163 (1988) 299.
- [7] H. Emling, *Prog. Part. Nucl. Phys.* 33 (1994) 729.
- [8] P. Chomaz, N. Frascaria, *Phys. Rep.* 252 (1995) 275.
- [9] T. Aumann, P.F. Bortignon, H. Emling, *Ann. Rev. Nucl. Part. Sci.* 48 (1998) 351.
- [10] P.G. Hansen, *Nucl. Phys. A* 553 (1993) 89c.
- [11] C.A. Bertulani, L.F. Canto, M.S. Hussein, *Phys. Rep.* 226 (1993) 282.
- [12] J. Barrette et al., *Phys. Lett. B* 209 (1988) 182.
- [13] J. Beene et al., *Phys. Rev. C* 41 (1990) 920.

- [14] J. Beene et al., International Nuclear Physics Conference on Giant Resonances, Gull Lake (1993), Nucl. Phys. A 569 (1994) 163c.
- [15] G. Baur, C.A. Bertulani, Phys. Lett. B 174 (1986) 23; Nucl. Phys. A 482 (1988) 313; Phys. Rev. C 34 (1986) 1654; Proceedings of International School of Heavy Ion Physics, Erice, Italy, October 1986, Plenum Press, New York, R.A. Broglia, G.F. Bertsch (Eds.), p. 331.
- [16] K. Alder, A. Winther, Coulomb Excitation, Academic Press, New York, 1966.
- [17] K. Alder, A. Winther, Electromagnetic Excitation, North-Holland, Amsterdam, 1975.
- [18] A. Winther, K. Alder, Nucl. Phys. A 319 (1979) 518.
- [19] C.A. Bertulani, L.F. Canto, M.S. Hussein, A.F.R. de Toledo Piza, Phys. Rev. C 53 (1996) 334.
- [20] J.D. Jackson, Classical Electrodynamics, Wiley, New York, 1975.
- [21] J.M. Eisenberg, W. Greiner, Excitation Mechanisms of the Nuclei, 3rd Edition, North-Holland, Amsterdam, 1987, p. 227.
- [22] C.A. Bertulani, G. Baur, Nucl. Phys. A 442 (1985) 73.
- [23] A.N.F. Aleixo, C.A. Bertulani, Nucl. Phys. A 505 (1989) 448.
- [24] L.D. Landau, E.M. Lifshitz, The Classical Theory of Fields, 4th English Edition, Pergamon, Oxford, 1979, p. 93.
- [25] C.E. Aguiar, A.N.F. Aleixo, C.A. Bertulani, Phys. Rev. C 42 (1990) 2180.
- [26] M. Abramowitz, I.A. Stegun, Handbook of Mathematical Functions, National Bureau of Standards, Washington, DC, 1964.
- [27] C.A. Bertulani, A. Nathan, Nucl. Phys. A 554 (1993) 158.
- [28] M.S. Hussein, R. Rego, C.A. Bertulani, Phys. Rep. 201 (1991) 279.
- [29] L. Ray, Phys. Rev. C 20 (1979) 1857.
- [30] I.S. Gradshteyn, I.M. Ryzhik, Table of Integrals, Series, and Products, Academic Press, New York, 1980.
- [31] F.E. Bertrand, J.R. Beene, Nucl. Phys. A 520 (1990) 627c.
- [32] A. Veyssi re, H. Beil, R. Berg re, P. Carlos, A. Lepr tre, Nucl. Phys. A 159 (1970) 561.
- [33] J. Raynal, Phys. Rev. C 23 (1981) 2571.
- [34] A.M. Nathan, Phys. Rev. C 43 (1991) 2479.
- [35] G.R. Satchler, Nucl. Phys. A 472 (1987) 215.
- [36] W.D. Myers, W.J. Swiatecki, Ann. of Phys. 55 (1969) 395; 84 (1974) 186.
- [37] Shen Wen-Qing et al., Nucl. Phys. A 491 (1989) 130.
- [38] T. Aumann, C.A. Bertulani, K. Suemmerer, Phys. Rev. C 51 (1995) 416.
- [39] J. Ritman et al., Phys. Rev. Lett. 70 (1993) 533.
- [40] R. Schmidt et al., Phys. Rev. Lett. 70 (1993) 1767.
- [41] T. Aumann et al., Phys. Rev. C 47 (1993) 1728.
- [42] C.A. Bertulani, V. Zelevinsky, Phys. Rev. Lett. 71 (1993) 967; Nucl. Phys. A 568 (1994) 931.
- [43] C.J. Benesh, B.C. Cook, J.P. Vary, Phys. Rev. C 40 (1989) 1198.
- [44] S. Kox et al., Phys. Rev. C 35 (1987) 1678.
- [45] B.L. Berman, R.E. Pywell, S.S. Dietrich, M.N. Thompson, K.G. McNeill, J.W. Jury, Phys. Rev. C 36 (1987) 1286.
- [46] GSI version of the code ALICE (M. Blann, F. Plasil, Phys. Rev. Lett. 29 (1972) 303); W. Reisdorf, M. Sch del, Z. Phys. A 343 (1992) 47.
- [47] W. Llope, P. Braun-Munzinger, Phys. Rev. C 45 (1992) 799; W. Llope, Ph. D. Dissertation, SUNY at Stony Brook, 1992, and private communication.
- [48] J.C. Hill, F.K. Wohn, D.D. Schwellenbach, A.R. Smith, Phys. Lett. B 273 (1991) 371, and references therein.
- [49] M.L. Justice et al., Phys. Rev. C (1994) R5.
- [50] J. Norbury, G. Baur, Phys. Rev. C 48 (1993) 1915.
- [51] C.A. Bertulani, Phys. Lett. B 319 (1993) 421.
- [52] A.C. Vasconcellos-Gomes, C.A. Bertulani, Nucl. Phys. A 517 (1990) 639.
- [53] S. Mordechai et al., Phys. Rev. Lett. 61 (1988) 531.
- [54] K. Boretzky et al., Phys. Lett. B 384 (1996) 30.
- [55] A. Bohr, B. Mottelson, Nuclear Structure, Vol. 1, Benjamin, New York, 1969; Vol. II, Benjamin, Reading, MA, 1975.
- [56] B.L. Berman, Atomic Data Nucl. Data Tables 15 (1975) 319.

- [57] V.Yu. Ponomarev, V.V. Voronov, *Phys. Lett. B* 279 (1992) 1.
- [58] W.R. Abel, A.C. Anderson, J.C. Wheatley, *Phys. Rev. Lett.* 17 (1966) 74.
- [59] B. Lauritzen, R.A. Broglia, T. Dossing, *Nucl. Phys. A* 457 (1986) 61.
- [60] G.F. Bertsch, P.F. Bortignon, R.A. Broglia, *Rev. Mod. Phys.* 55 (1983) 287.
- [61] B.W. Bush, G.F. Bertsch, B.A. Brown, *Phys. Rev. C* 45 (1992) 1709.
- [62] S. Mordechai et al., *Phys. Rev. C* 41 (1990) 202.
- [63] V.G. Zelevinsky, unpublished.
- [64] V.G. Zelevinsky, *Nucl. Phys. A* 555 (1993) 109.
- [65] A. Bracco et al., *Phys. Rev. Lett.* 62 (1989) 2080.
- [66] J. Reiter, H.L. Harney, *Z. Phys. A* 337 (1990) 121.
- [67] V.G. Zelevinsky, P. von Brentano, *Nucl. Phys. A* 529 (1991) 141.
- [68] V.V. Sokolov, V.G. Zelevinsky, *Ann. Phys. (NY)* 216 (1992) 323.
- [69] R.-D. Herzberg, P. von Brentano, I. Rotter, preprint, 1991.
- [70] G. Lauritsch, P.-G. Reinhard, *Nucl. Phys. A* 509 (1990) 287.
- [71] L.F. Canto, A. Romanelli, M.S. Hussein, A.F.R. de Toledo Piza, *Phys. Rev. Lett.* 72 (1994) 2147.
- [72] M.S. Hussein, M.P. Pato, A.F.R. de Toledo Piza, *Phys. Rev. C* 51 (1995) 846.
- [73] C. Volpe et al., *Nucl. Phys. A* 589 (1995) 521.
- [74] E.G. Lanza, M.V. Andrés, F. Catara, Ph. Chomaz, C. Volpe, *Nucl. Phys. A* 613 (1997) 445.
- [75] P.F. Bortignon, Ch. Dasso, *Phys. Rev. C* 56 (1997) 574.
- [76] G.F. Bertsch, H. Feldmeier, *Phys. Rev. C* 56 (1997) 839.
- [77] B.V. Carlson, L.F. Canto, S. Cruz-Barrios, M.S. Hussein, A.F.R. de Toledo Piza, *Phys. Rev. C* 59 (1999) 2689.
- [78] B.V. Carlson, M.S. Hussein, A.F.R. de Toledo Piza, L.F. Canto, *Phys. Rev. C* 60 (1999) 014604.
- [79] C.M. Ko, *Z. Phys. A* 286 (1978) 405.
- [80] B.V. Carlson, M.S. Hussein, A.F.R. de Toledo Piza, *Phys. Lett. B* 431 (1998) 249.
- [81] M.S. Hussein, A.F.R. de Toledo Piza, O.K. Vorov, *Phys. Rev. C* 59 (1999) R1242–R1246.
- [82] B.V. Carlson, M.S. Hussein, *Phys. Rev. C* 59 (1999) R2343.
- [83] A.F.R. de Toledo Piza, M.S. Hussein, B.V. Carlson, C.A. Bertulani, L.F. Canto, S. Cruz-Barrios, *Phys. Rev. C* 59 (1999) 3093.
- [84] V.G. Soloviev, *Theory of Atomic Nuclei: Quasiparticles and Phonons*, Inst. of Phys. Publ., Bristol, 1992.
- [85] A.I. Vdovin, V.G. Soloviev, *Phys. Part. Nucl.* 14 (1983) 99.
- [86] V.V. Voronov, V.G. Soloviev, *Phys. Part. Nucl.* 14 (1983) 583.
- [87] V.Yu. Ponomarev, V.G. Soloviev, Ch. Stoyanov, A.I. Vdovin, *Nucl. Phys. A* 323 (1979) 446.
- [88] V.V. Voronov, D.T. Khoa, *Izv. Akad. Nauk SSSR, Ser. Fiz.* 48 (1984) 2008.
- [89] T. Marumori, *Prog. Theory Phys.* 31 (1964) 1009.
- [90] R. Piepenbring, K.V. Protasov, B. Silvestre-Brac, *Nucl. Phys. A* 586 (1995) 396, 413.
- [91] M. Grinberg, R. Piepenbring, K.V. Protasov, B. Silvestre-Brac, *Nucl. Phys. A* 597 (1996) 355.
- [92] T.K. Dinh, M. Grinberg, Ch. Stoyanov, *J. Phys. G* 18 (1992) 329.
- [93] D.A. Varshalovich, A.N. Noskolev, V.K. Khersonskii, *Quantum Theory of Angular Momentum*, World Scientific, Singapore, 1988.
- [94] V.Yu. Ponomarev, Ch. Stoyanov, N. Tsoneva, M. Grinberg, *Nucl. Phys. A* 635 (1998) 470.
- [95] M. Kneissl, H.H. Pitz, A. Zilges, *Prog. Part. Nucl. Phys.* 37 (1996) 439.
- [96] E.G. Lanza, M.V. Andrés, F. Catara, Ph. Chomaz, C. Volpe, *Nucl. Phys. A* 636 (1998) 452.
- [97] S. Nishizaki, J. Wambach, *Phys. Lett. B* 349 (1995) 7.
- [98] S. Nishizaki, J. Wambach, *Phys. Rev. C* 57 (1998) 1515.
- [99] S. Drożdż, S. Nishizaki, J. Speth, J. Wambach, *Phys. Rep.* 197 (1990) 1.
- [100] F. Catara, Ph. Chomaz, N. Van Giai, *Phys. Lett. B* 277 (1992) 1.
- [101] D.R. Bes et al., *Nucl. Phys. A* 452 (1986) 531.
- [102] S.N. Belyaev et al., *Sov. J. Nucl. Phys.* 55 (1992) 157.
- [103] S.N. Belyaev et al., *Phys. At. Nucl.* 58 (1995) 1833.
- [104] C.A. Bertulani, V.Yu. Ponomarev, V.V. Voronov, *Phys. Lett. B* 388 (1996) 457.
- [105] J. Stroth et al., *Nucl. Phys. A* 599 (1996) 307c.

- [106] V.Yu. Ponomarev et al., *Phys. Rev. Lett.* 72 (1994) 1168.
- [107] V.Yu. Ponomarev, P.F. Bortignon, R.A. Broglia, E. Vigezzi, V.V. Voronov, *Nucl. Phys. A* 599 (1996) 341c.
- [108] V.Yu. Ponomarev, P.F. Bortignon, R.A. Broglia, V.V. Voronov, *Z. Phys. A* 356 (1996) 251.
- [109] V.Yu. Ponomarev, C.A. Bertulani, *Phys. Rev. Lett.* 79 (1997) 3853.
- [110] C. Yannouleas, S. Jang, Ph. Chomaz, *Phys. Lett. B* 163 (1985) 55.
- [111] F. Catara, Ph. Chomaz, N. Van Giai, *Phys. Lett. B* 233 (1989) 6.
- [112] V.Yu. Ponomarev, P. von Neumann-Cosel, *Phys. Rev. Lett.* 82 (1998) 501.
- [113] V.Yu. Denisov, *Phys. Rev. C* 57 (1998) 666.
- [114] H. Emling, private communication.
- [115] V.Yu. Ponomarev, C.A. Bertulani, *Phys. Rev. C* 57 (1998) 3476.
- [116] V.Yu. Ponomarev, C.A. Bertulani, A.V. Sushkov, *Phys. Rev. C* 58 (1998) 2750.
- [117] S.P. Ivanova, A.L. Komov, L.A. Malov, V.G. Soloviev, *Phys. Part. Nucl.* 7 (1976) 175; V.G. Soloviev, A.V. Sushkov, N.Yu. Shirikova, *Z. Phys. A* 358 (1997) 287.
- [118] S.V. Akulinichev, L.A. Malov, *J. Phys. G: Nucl. Phys.* 3 (1977) 625.
- [119] G.M. Gurevich, L.E. Lazareva, V.M. Mazur, G.V. Solodukhov, B.A. Tulupov, *Nucl. Phys. A* 273 (1976) 326.
- [120] V.G. Soloviev, A.V. Sushkov, N.Yu. Shirikova, *Phys. Part. Nucl.* 25 (1994) 157.
- [121] C.A. Bertulani, *Comput. Phys. Commun.* 116 (1999) 345.